The Astronomical Journal, 151:74 (43pp), 2016 March doi:10.3847/0004-6256/151/3/74

INVISIBLE ACTIVE GALACTIC NUCLEI. II. RADIO MORPHOLOGIES AND FIVE NEW H I 21 cm ABSORPTION LINE DETECTORS

Ting Yan[1,2], John T. Stocke[1,2], Jeremy Darling[1,2], Emmanuel Momjian[3], Soniya Sharma[4], and Nissim Kanekar[5]
[1] Center for Astrophysics and Space Astronomy, UCB 389, University of Colorado, Boulder, CO 80309-0389, USA
[2] Department of Astrophysical and Planetary Sciences, UCB 391, University of Colorado, Boulder, CO 80309-0391, USA
[3] National Radio Astronomy Observatory, P.O. Box O, Socorro, NM 87801, USA
[4] Research School of Astronomy & Astrophysics, The Australian National University, Mt Stromlo Observatory, ACT 2611, Australia
[5] National Centre for Radio Astrophysics, TIFR, Post Bag 3, Ganeshkhind, Pune 411 007, India
Received 2014 August 22; accepted 2015 December 23; published 2016 February 24

ABSTRACT

This is the second paper directed toward finding new highly redshifted atomic and molecular absorption lines at radio frequencies. To this end, we selected a sample of 80 candidates for obscured radio-loud active galactic nuclei (AGNs) and presented their basic optical/near-infrared (NIR) properties in Paper I. In this paper, we present both high-resolution radio continuum images for all of these sources and H I 21 cm absorption spectroscopy for a few selected sources in this sample. A-configuration 4.9 and 8.5 GHz Very Large Array continuum observations find that 52 sources are compact or have substantial compact components with size $<0\farcs5$ and flux densities >0.1 Jy at 4.9 GHz. The 36 most compact sources were then observed with the Very Long Baseline Array at 1.4 GHz. One definite and 10 candidate Compact Symmetric Objects (CSOs) are newly identified, which is a detection rate of CSOs ~three times higher than the detection rate previously found in purely flux-limited samples. Based on possessing compact components with high flux densities, 60 of these sources are good candidates for absorption-line searches. Twenty-seven sources were observed for H I 21 cm absorption at their photometric or spectroscopic redshifts with only six detections (five definite and one tentative). However, five of these were from a small subset of six CSOs with pure galaxy optical/NIR spectra (i.e., any AGN emission is obscured) and for which accurate spectroscopic redshifts place the redshifted 21 cm line in a radio frequency intereference (RFI)-free spectral "window" (i.e., the percentage of H I 21 cm absorption-line detections could be as high as ~90% in this sample). It is likely that the presence of ubiquitous RFI and the absence of accurate spectroscopic redshifts preclude H I detections in similar sources (only 1 detection out of the remaining 22 sources observed, 13 of which have only photometric redshifts); that is, H I absorption may well be present but is masked by the RFI. Future searches for highly redshifted H I and molecular absorption can easily find more distant CSOs among bright, "blank field" radio sources, but will be severely hampered by an inability to determine accurate spectroscopic redshifts due to their lack of rest-frame UV continuum.

Key words: quasars: absorption lines – radio continuum: galaxies

1. INTRODUCTION

Finding highly redshifted absorption lines at radio frequencies is important yet challenging work. Up to now there have been ~80 H I absorption systems detected at cosmological distances ($z > 0.1$), among which about half are associated absorption systems (i.e., $z_{\rm abs} = z_{\rm em}$). The detection rate is 30% in compact radio sources (Vermeulen et al. 2003) and can be as high as 50% in $z < 1$ CSO/GPS sources (e.g., Pihlström et al. 2003; Gupta et al. 2006). Except for two H I absorbers found at $z > 1.5$, various surveys have failed to find more associated ($z_{\rm abs} = z_{\rm em}$) absorption systems at high-z (e.g., Curran et al. 2008, 2011a). Recently, a few intervening absorption systems have been found at high redshift by targeting damped Lyα (DLA) absorbers (DLA; Kanekar et al. 2007, 2013, 2014; York et al. 2007), but none include molecular absorbers (Curran et al. 2004, 2006). Meanwhile, there are only five known molecular absorption systems at $z > 0.1$ (one detected only in OH), all at $z < 1$ (Wiklind & Combes 1994, 1995, 1996a, 1996b; Kanekar et al. 2005). More detections are, in general, important for understanding the cosmic evolution in the local physical properties of the cold dense gas out of which stars form.

Another potentially important application is to use atomic and molecular radio absorption lines to determine whether there are spacial or temporal variations in fundamental physical parameters, such as the fine-structure constant (α) and the proton-to-electron mass ratio. In this latter application, radio frequency absorption-line measurements provide distinct advantages over optical techniques due to the precision with which frequencies can be calibrated, the narrowness of the absorption features that arise in cold gas (e.g., OH, CO and formaldehyde), and the physics of the OH molecule's "satellite lines" (Chengalur & Kanekar 2003; Darling 2003, 2004). In contrast to claims based on optical spectroscopy that changes in the value of α have been detected at $z > 2$ (Webb et al. 1999, 2011; Murphy et al. 2001, 2008), radio spectroscopy has not found any evidence for a change in α, but only out to $z \approx 0.75$ (Kanekar et al. 2012). However, the absence of known molecular absorbers at $z > 1$ means that the current set of radio observations cannot rule out the claims made from optical spectroscopy at higher redshifts. The discovery of $z > 1$ molecular absorption systems must be made to confirm or challenge these optical claims. However, the more distant active galactic nuclei (AGNs) are typically much more luminous in the optical/UV, which may preclude the detection of neutral and molecular gas (Curran & Whiting 2010, 2012).

To this end we have embarked on a systematic search for obscured radio-loud AGNs. In Paper I of this work, we described the selection techniques for the sample and presented

our near-infrared (NIR) photometry for the sample. The selection method used the overlap region between the Faint Images of the Radio Sky at 20 cm (FIRST) survey and the Sloan Digital Sky Survey (SDSS) to identify strong radio galaxies ($f_{20\,\mathrm{cm}} > 0.3$ Jy) whose optical morphologies are diffuse, likely late-type or interacting galaxies. The purpose of the NIR imaging was to verify the optical classifications and provide a broader baseline in wavelength for better spectral energy distribution (SED) characterization and more accurate photometric redshift determination. After confirming that most of the sample objects are best fit by pure galaxy SEDs requiring any AGN emission to be absent or heavily obscured (i.e., a typical non-thermal AGN continuum is not present), in this paper we identify sources that are compact enough at radio frequencies for absorption to be detectable. By this we mean that a source dominated by a compact component will not have its absorption diluted by extended flux that comes to us along unabsorbed sightlines. We also present a preliminary search for redshifted H I 21 cm and OH molecular absorption lines in which six new H I detections and no molecular detections were made.

Most radio-loud AGN are not good candidates for discovering highly redshifted absorption because numerous studies of radio-loud AGN host galaxies find that they are almost exclusively ellipticals (e.g., Urry & Padovani 1995; Best et al. 2005) with little cold gas. But recent large surveys make it possible to find rare cases that do not obey this rule. In Paper 1 we selected a sample of 82 objects that make up only ∼5% of the ∼1500 sources with flux densities >300 mJy in the 2003 April version of the FIRST survey (Becker et al. 1995). Among the ∼50% of these that have coincident optical galaxies detected by the SDSS Data Release 5 (DR5; Adelman-McCarthy et al. 2007), the majority have typical elliptical morphology (i.e., a De Vaucouleurs radial profile and a large concentration index (Strateva et al. 2001) or are classified by SDSS as point sources). Only 82 optical counterparts have late-type, low central-concentration morphologies, suggesting they could be late-type galaxies, interacting galaxies, or occasionally intervening systems for which the detected optical object is a foreground spiral galaxy not related physically to the radio source. In any of these cases, the nuclear source could be obscured by dust in the gas-rich optical counterpart, becoming "invisible" AGN in the optical.

In Paper I, we presented near-infrared (NIR) J, H, and K_{short} observations for this sample obtained using the Astrophysical Research Consortium 3.5-m telescope at the Apache Point Observatory (APO), which is also the site of the SDSS 2.5-m telescope. Our NIR observing conditions typically were better than the SDSS optical observing conditions, allowing a good test of the SDSS optical morphology classifications for these faint sources. The morphology is largely consistent between the NIR images and optical images; with very few exceptions the diffuse morphology of the hosts for these luminous radio sources is confirmed, suggesting that these can be gas-rich systems containing a radio-loud AGN. Analysis of the optical-NIR SEDs in Paper I indicates that only a small number of sources have pure elliptical or un-reddened quasar-like SEDs. Many sources show late-type galaxy SEDs or significantly reddened quasar-like SEDs. Most of these optical-NIR SEDs are consistent with pure galaxy SEDs with heavily obscured nuclei; in several cases NIR turnups are present confirming this hypothesis. Mid-IR photometry from the *Spitzer Space Telescope* "warm mission" and from the *Wide-field Infrared Survey Explorer* (*WISE*) mission is available to determine which sources in this sample are the most heavily obscured.

From the radio source perspective, this sample may catch a unique evolutionary phase or subclass of radio galaxies. The study of the host galaxies and multi-wavelength properties of the central AGN can shed light on the formation and evolution of radio galaxies. The radio structure, particularly the size of the most compact components, can also provide unique insights into the earliest evolutionary phases of radio galaxy evolution, and can test the "breakout" paradigm central to prevailing pictures of AGN feedback.

In this paper we continue the investigation of this uniquely selected sample of obscured radio-loud AGN by presenting Very Large Array (VLA) and Very Long Baseline Array (VLBA) images of a large sub-sample of these sources. These maps are used both to identify the most compact sources in this sample and to find unusual individual cases that are the best candidates for possessing cold gas absorption. Additionally, we present the results for redshifted H I 21 cm absorption-line spectroscopy for 27 sources in the sample out of which 5 definite and 1 tentative H I detections were made. No molecular detections were made for any of the H I detections.

The sample selection from Paper 1 is briefly reviewed in Section 2. In Section 3 we describe our radio continuum observing strategy, data reduction process, and basic observational results. The radio maps and source fluxes are presented in an Appendix. Statistical relations between radio morphologies, radio spectral types, and optical+NIR SEDs in this sample are studied and individual sources of interest (e.g., intervening systems, possible gravitational lens systems) are described in this same section. In Section 4 we describe the limited radio spectroscopy that has been attempted for this sample and present five H I 21 cm detections. The overall results from this work are discussed and summarized in Section 5. Future progress in the search for high-z atomic and molecular absorbers will require precise spectroscopic redshifts for the associated galaxies in this sample so that optimal search strategies (e.g., telescope and radio frequency intereference (RFI) environment) can be employed.

Throughout this paper, we assume a ΛCDM cosmology with $H_0 = 71$ km s^{-1} Mpc^{-1}, $\Omega_\Lambda = 0.73$, and $\Omega_M = 0.27$.

2. THE SAMPLE

The specific selection criteria for the sample presented in Paper I include the presence of an SDSS r-band optical counterpart within 1.″5 of a bright (⩾0.5 Jy) FIRST radio source position and characteristics of the optical counterpart that favor it being a late-type galaxy (i.e., low central compactness index and a surface brightness profile more similar to an exponential disk (Strateva et al. 2001) than an $r^{1/4}$-law). Of the 82 objects originally selected (Paper I), 2 are nearby galaxies at $z < 0.05$ (J1352+3126 and J1413−0312) and are excluded from our discussion in this paper. Among the remainder of the 80 objects, only 3 have angular sizes larger than 5″ in their SDSS images, which corresponds to 16 kpc at $z = 0.2$; these are J1347+1217 at $z = 0.122$, J0920+2714 at $z = 0.206$, and J0901+0304 at $z = 0.287$. We expect most other objects to have redshifts between approximately 0.2 and 1.0 due to the detection limits of the SDSS photometric survey (except for a few high-z quasars, which may be mistakenly

Table 1
Observing Summary

Object	Radio Name	VLA 4.9 GHz		VLA 8.5 GHz		VLBI		Notes[a]
		Date	References	Date	References	Date	References	
J0000−1054	PKS 2358-111	2007 Aug 12	[1]	2007 Aug 12	(1)	⋯	⋯	⋯
J0003−1053	PKS 0001-111	2007 Aug 12	(1)	2007 Aug 12	(1)	⋯	⋯	⋯
J0134+0003	4C −00.11	2007 Aug 11	(1)	⋯	⋯	⋯	⋯	N1
J0249−0759	PKS 0247-08	2007 Aug 11	(1)	2007 Aug 11	(1)	⋯	⋯	N1, N2
J0736+2954	TXS 0733+300	2007 Jul 08	(1)	⋯	⋯	⋯	⋯	N3
J0747+4618	4C +46.16	⋯	(13)	⋯	(13)	⋯	⋯	⋯
J0749+2129	TXS 0746+216	2007 Jun 16	(1)	2007 Jun 16	(1)	⋯	⋯	⋯
J0751+2716	B2 0748+27	⋯	(15)	⋯	(15)	⋯	⋯	⋯
J0759+5312	TXS 0755+533	2007 Jun 16	(1)	2007 Jun 16	(1)	2009 Dec 10	(1)	⋯
J0805+1614	PKS 0802+16	1987 Sep 13	(3)	2007 Jul 08	(1)	2009 Dec 08	(1)	⋯
J0807+5327	TXS 0803+536	2007 Jun 16	(1)	2007 Jun 16	(1)	2009 Dec 10	(1)	⋯
J0824+5413	TXS 0820+543	2007 Jun 16	(1)	2007 Jun 16	(1)	2009 Dec 10	(1)	N4
J0834+1700	4C +17.45	⋯	⋯	2007 Jul 08	(1)	2009 Dec 08	(1)	⋯
J0839+2403	4C +24.18	2007 Jul 08	(1)	⋯	⋯	⋯	⋯	⋯
J0843+4215	B3 0840+424A	⋯	⋯	⋯	(16)	⋯	(14)	⋯
J0901+0304	PKS 0859+032	2007 Jul 06	(1)	⋯	⋯	2010 Jan 03	(1)	⋯
J0903+5012	4C +50.28	2007 Jun 16	(1)	2007 Jun 16	(1)	⋯	⋯	⋯
J0905+4128	B3 0902+416	⋯	(13)	⋯	(13)	⋯	(12)	⋯
J0907+0413	4C +04.30	1984 Dec 17	(8)	⋯	⋯	⋯	⋯	⋯
J0910+2419	4C +24.19	2007 Jul 08	(1)	⋯	⋯	⋯	⋯	⋯
J0915+1018	TXS 0912+105	1985 Feb 07	(8)	⋯	⋯	⋯	⋯	⋯
J0917+4725	B3 0914+476	2007 Jun 16	(1)	2007 Jun 16	(1)	2009 Dec 10	(1)	⋯
J0920+1753	4C +18.29	2007 Jul 08	(1)	⋯	⋯	2009 Dec 08	(1)	N4
J0920+2714	B2 0917+27B	2007 Jun 17	(1)	2007 Jun 17	(1)	2009 Dec 08	(1)	⋯
J0939+0304	PKS 0937+033	1984 Dec 17	(8)	⋯	⋯	2010 Jan 03	(1)	⋯
J0945+2640	B2 0942+26	2001 Jan 26	(9)	⋯	⋯	2009 Dec 08	(1)	⋯
J0951+1154	TXS 0948+121	1985 Feb 08	(8)	2007 Jul 06	(1)	⋯	⋯	⋯
J1008+2401	B2 1005+24	2007 Jul 08	(1)	⋯	⋯	2009 Dec 08	(1)	N4
J1010+4159	B3 1007+422	⋯	(13)	⋯	(13)	⋯	(12)	⋯
J1019+4408	B3 1016+443	⋯	(13)	⋯	(13)	⋯	(12)	⋯
J1023+0424	TXS 1021+046	1986 Apr 22	(4)	2007 Jul 06	(1)	2010 Jan 03	(1)	⋯
J1033+3935	B2 1030+39	⋯	⋯	⋯	(16)	⋯	(14)	⋯
J1034+1112	TXS 1031+114	2007 Jun 17	(1)	2007 Jun 17	(1)	⋯	⋯	⋯
J1043+0537	4C +05.45	2007 Jul 06	(1)	⋯	⋯	2010 Jan 03	(1)	N4
J1045+0455	TXS 1043+051	2007 Jun 17	(1)	2007 Jun 17	(1)	⋯	⋯	⋯
J1048+3457	4C +35.23	1986 Mar 08	(2)	⋯	⋯	2009 Dec 08	(1)	⋯
J1120+2327	4C +23.27	⋯	⋯	⋯	⋯	⋯	⋯	⋯
J1125+1953	PKS 1123+201	2007 Jul 06	(1)	⋯	⋯	2009 Dec 08	(1)	⋯
J1127+5743	TXS 1124+579	2007 Jun 16	(1)	2007 Jun 16	(1)	2009 Dec 10	(1)	⋯
J1129+5638	TXS 1126+569	2007 Jun 16	(1)	2007 Jun 16	(1)	2009 Dec 10	(1)	⋯
J1142+0235	TXS 1139+028	1985 Feb 08	(8)	2007 Jul 08	(1)	2010 Jan 03	(1)	N4
J1147+4818	4C +48.33	2007 Jun 17	(1)	2007 Jun 17	(1)	2009 Dec 10	(1)	⋯
J1148+1404	TXS 1145+143	1986 Apr 08	(4)	2007 Jul 06	(1)	2010 Jan 03	(1)	⋯
J1202+1207	TXS 1200+124	2007 Jun 17	(1)	2007 Jun 17	(1)	2010 Jan 03	(1)	⋯
J1203+4632	B3 1200+468	2007 Jul 08	(1)	⋯	⋯	⋯	⋯	⋯
J1207+5407	4C +54.26	2007 Jun 16	(1)	2007 Jun 16	(1)	⋯	⋯	⋯
J1215+1730	4C +17.54	⋯	⋯	⋯	(16)	⋯	(14)	⋯
J1228+5348	4C +54.28	2007 Jun 16	(1)	2007 Jun 16	(1)	⋯	⋯	⋯
J1238+0845	TXS 1235+090	2007 Jun 17	(1)	2007 Jun 17	(1)	2010 Jan 03	(1)	⋯
J1300+5029	TXS 1258+507	⋯	⋯	⋯	(17)	⋯	(14)	⋯
J1312+1710	TXS 1310+174	1986 Apr 08	(4)	2007 Jul 08	(1)	2009 Dec 08	(1)	⋯
J1315+0222	TXS 1312+026	1984 Dec 17	(8)	2007 Jul 08	(1)	⋯	⋯	⋯
J1341+1032	4C +10.36	2007 Jun 17	(1)	2007 Jun 17	(1)	⋯	⋯	⋯
J1345+5846	4C +59.20	2007 Jun 17	(1)	2007 Jun 17	(1)	2009 Dec 10	(1)	⋯
J1347+1217	4C +12.50	⋯	⋯	⋯	⋯	⋯	⋯	⋯
J1348+2415	4C +24.28	⋯	(11)	⋯	⋯	⋯	(10)	⋯
J1354+5650	4C +57.23	2007 Jun 17	(1)	2007 Jun 17	(1)	⋯	⋯	⋯
J1357+0046	PKS 1355+01	2007 Jun 17	(1)	2007 Jun 17	(1)	2010 Jan 03	(1)	⋯
J1410+4850	TXS 1408+490	2007 Jul 15	(1)	2007 Jul 15	(1)	2009 Dec 10	(1)	⋯
J1413−0312	TXS 1410-029	⋯	⋯	⋯	⋯	⋯	⋯	⋯
J1413+1509	TXS 1411+154	2007 Jul 15	(1)	⋯	⋯	⋯	⋯	⋯
J1414+4554	B3 1412+461	⋯	⋯	⋯	(17)	⋯	(18)	⋯
J1415+1320	PKS 1413+135	⋯	⋯	⋯	⋯	⋯	(19)	⋯

Table 1
(Continued)

Object	Radio Name	VLA 4.9 GHz		VLA 8.5 GHz		VLBI		Notes[a]
		Date	References	Date	References	Date	References	
J1421−0246	4C −02.60	2007 Jul 10	(1)	2007 Jul 10	(1)	⋯	⋯	⋯
J1424+1852	4C +19.47	2007 Jul 10	(1)	2007 Jul 10	(1)	⋯	⋯	⋯
J1502+3753	B2 1500+38	2007 Jul 15	(1)	2007 Jul 15	(1)	⋯	⋯	⋯
J1504+5438	TXS 1503+548	⋯	⋯	⋯	(16)	⋯	(14)	⋯
J1504+6000	TXS 1502+602	2007 Jun 17	(1)	2007 Jun 17	(1)	2010 Jan 11	(1)	⋯
J1523+1332	4C +13.54	2007 Jul 10	(1)	2007 Jul 10	(1)	2010 Jan 11	(1)	⋯
J1527+3312	B2 1525+33	2007 Jul 15	(1)	1991 Jul 26	(6)	2010 Jan 11	(1)	N5
J1528−0213	PKS 1525-020	2007 Jul 10	(1)	2007 Jul 10	(1)	⋯	⋯	⋯
J1548+0808	TXS 1545+082	2007 Jul 15	(1)	2007 Jul 15	(1)	2010 Jan 11	(1)	⋯
J1551+6405	TXS 1550+642	⋯	⋯	⋯	(16)	⋯	(14)	⋯
J1559+4349	4C +43.36	1999 Jun 23	(7)	⋯	⋯	2010 Jan 11	(1)	⋯
J1604+6050	TXS 1603+609	2007 Jun 17	(1)	2007 Jun 17	(1)	2010 Jan 11	(1)	⋯
J1616+2647	PKS 1614+26	2007 Jul 15	(1)	1990 May 04	(5)	2010 Jan 11	(1)	N2
J1625+4134	4C +41.32	⋯	⋯	⋯	(16)	⋯	(14)	⋯
J1629+1342	4C +13.60	2007 Jul 15	(1)	2007 Jul 15	(1)	⋯	⋯	⋯
J1633+4700	4C +47.43	2007 Jul 15	(1)	2007 Jul 15	(1)	2010 Jan 11	(1)	⋯
J1724+3852	B2 1722+38	2007 Jul 15	(1)	2007 Jul 15	(1)	2010 Jan 11	(1)	⋯
J2203−0021	4C −00.79	2007 Aug 11	(1)	⋯	⋯	⋯	⋯	N1

Note.
[a] N1–N5 in this column means: N1, no flux calibration on the VLA-A 4.9 GHz image; N2, no flux calibration on the VLA-A 8.5 GHz image; N3, not detected on the VLA-A 4.9 GHz image; N4, not detected on the VLBA 1.4 GHz image; N5, all data are flagged on the VLA-A 4.9 GHz image.
References. (1) This work (VLA project AY0052 and VLBA project BY 0020), (2) VLA project AA052, (3) VLA project AA073, (4) VLA project AB375, (5) VLA project AB568, (6) VLA project AB611, (7) VLA project AB922, (8) VLA project AH167, (9) VLA project AS704, (10) Cai et al. (2002), (11) Chambers et al. (1996), (12) Dallacasa et al. (2002a), (13) Fanti et al. (2001), (14) Helmboldt et al. (2007), (15) Lehar et al. (1997), (16) Myers et al. (2003), (17) Patnaik et al. (1992), (18) Peck & Taylor (2000), (19) Perlman et al. (2002).

present in the sample). The photometric and spectroscopic redshifts for individual optical counterparts in the sample support this conclusion. A listing of the full sample of sources and their basic parameters can be found in Paper I and Yan (2013).

A non-elliptical optical morphology could indicate a late-type galaxy, an interacting system, or a gravitational lens system. We find examples that are already identified in our sample for each of the three possibilities: J1415+1320 (a.k.a. PKS 1413+135) is an edge-on spiral galaxy at $z = 0.247$ and the first object with molecular absorption lines detected at cosmological distances (Wiklind & Combes 1994). J0751+2716 is a gravitationally lensed system with a background quasar at $z = 3.2$ and a foreground galaxy at $z = 0.349$; strong CO emission lines are found in the high-z quasar because of the high magnification factor due to a strong lensing effect (Barvainis & Ivison 2002). J1347+1217 is an interacting system at $z = 0.122$ with H I absorption lines detected (Mirabel 1989). There are also two sources, J1120+2327 and J1348+2415, that are known alignment-effect radio galaxies in which the optical morphology is dominated by extended emission-line atomic gas (Miley & De Breuck 2008).

In Paper I, we re-evaluated all 80 objects using SDSS Data Release 8 and found 5 objects that were likely to be misclassified early-type galaxies. Because the possibility of being late-type cannot be ruled out completely, and to retain a complete sample selected from SDSS DR5 and the 2003 April version of FIRST, we still include those five objects in this paper. The optical counterpart of J0834+1700 is coincident with one lobe of a double-lobe radio galaxy. We excluded it in Paper I, but it actually could be an intervening system with potential absorption and remains in the sample for this paper.

3. RADIO CONTINUUM IMAGING

3.1. Observations and Data Reduction

Except when archive data were available, we observed all the sources at 4.9 and 8.5 GHz using the VLA of NRAO in its most extended A-configuration (VLA-A; project # AY0052).[6] Overall, we obtained data for 35 sources at both frequencies, 14 at 4.9 GHz only, and 8 at 8.5 GHz only. Our data were taken during 2007 June to August in the transitional period from VLA to Expanded VLA (EVLA; currently the Karl G. Jansky VLA). The observations were made with an effective bandwidth of 100 MHz in full polarization centered at 4.860 and 8.460 GHz. The typical on-source observing time was 4–5 minutes for each object at one frequency. We bracketed each target or a group of close-by targets with a single phase calibrator.

We initially reduced all VLA data using the Common Astronomy Software Applications (CASA) Version 2.3.1; then we found that the centers of many images were shifted from the pointing center to the brightest point, probably due to problems in the self-calibration process. Reduction was rectified using the Astronomical Imaging Processing System (AIPS) for 4.9 GHz data, but was not possible for the 8.5 GHz data. This problem does not affect our conclusions in this paper because the relative structure of the 8.5 GHz images remains correct. However, caution must be exercised in identifying individual component correlations between frequencies. For this reason, we display the 8.5 GHz images only in relative coordinates.

[6] The National Radio Astronomy Observatory (NRAO) is a facility of the National Science Foundation (NSF) operated under cooperative agreement by Associated Universities, Inc.

Table 2
Summary of Radio Galaxy Properties

Object	z	SED Type	G Type	S_{365} (Jy)	$S_{1.4}$ (Jy)	$S_{4.9}$ (Jy)	$\alpha_{\rm l}$	$\alpha_{\rm h}$	Spec. Type	LAS ($''$)	LLS (kpc)	Freq.(GHz)/ Telescope	Morph.	EVAL
(1)	(2)	(3)	(4)	(5)	(6)	(7)	(8)	(9)	(10)	(11)	(12)	(13)	(14)	(15)
J0000−1054	⋯	Q+abs	⋯	2.20	0.40	0.07	−1.28	−1.41	USS	1.5	<12.9	4.9/VLA-A	MSO	Y
J0003−1053	1.474[a]	Q+abs	⋯	1.47	0.40	0.14	−0.97	−0.84	SS	2.3	20.0	4.9/VLA-A	CPLX	Y, I:
J0134+0003	0.879	G	Sa	1.11	0.89	0.46	−0.17	−0.53	GPS	0.018	0.140	2.3/VLBI	CSO:	Y
J0249−0759	⋯	G+Q	⋯	2.34	0.62	0.19	−0.99	−0.95	SS	1.9	<16.3	4.9/VLA-A	LSO	N
J0736+2954	⋯	G+Q	⋯	0.35	0.49	0.52	0.26	0.05	FS	0.014	<0.118	5/VLBI	CJ	Y
J0747+4618	2.926	Q+abs	⋯	2.00	0.52	0.13	−1.00	−1.09	USS	1.3	10.6	4.9/VLA-A	MSO	N
J0749+2129	0.52*	G	S0	1.13	0.42	0.12	−0.73	−1.05	SS	2.6	∼16.1	4.9/VLA-A	CPLX	Y
J0751+2716	3.200[b]	G	Sc	1.47	0.60	0.21	−0.66	−0.83	SS	0.80	6.14	8.5/VLA-A	GA	Y, I
J0759+5312	⋯	G+Q	⋯	1.12	0.33	0.15	−0.91	−0.63	SS	1.4	<11.9	4.9/VLA-A	MSO	Y
J0805+1614	0.632 :	G	Sc	1.78	0.63	0.20	−0.77	−0.94	SS	0.45	: 3.10	8.5/VLA-A	MSO	Y
J0807+5327	⋯	Q+abs	⋯	0.83	0.33	0.11	−0.69	−0.92	SS	1.1	<9.15	4.9/VLA-A	MSO	Y, I:
J0824+5413	0.639	G+Q	⋯	1.12	0.39	0.15	−0.79	−0.77	SS	1.8	12.4	4.9/VLA-A	MSO	Y
J0834+1700	⋯	Q+abs	⋯	5.64	1.64	0.58	−0.92	−0.84	SS	0.11	<0.966	1.4/VLBI	SL	Y, I
J0839+2403	⋯	G+Q	⋯	1.77	0.66	0.23	−0.73	−0.84	SS	4.1	<35.3	4.9/VLA-A	LSO	N
J0843+4215	0.60*	G	Sb	2.50	1.46	0.58	−0.40	−0.74	SS ✓	0.021	∼0.143	5/VLBI	CJ	Y
J0901+0304	0.287	G	Sc	0.56	0.38	0.26	−0.28	−0.31	GPS ✓	0.011	0.047	1.4/VLBI	PS	Y
J0903+5012	⋯	G+Q	⋯	2.78	0.95	0.31	−0.80	−0.90	SS	3.4	<29.0	4.9/VLA-A	LSO	N
J0905+4128	⋯	G+Q	⋯	1.10	0.48	0.16	−0.61	−0.90	SS	0.33	<2.82	1.66/VLBI	MSO	Y
J0907+0413	1.10*	G	Sc	1.85	0.70	0.19	−0.72	−1.04	SS	2.6	∼21.4	4.9/VLA-A	LSO	N
J0910+2419	⋯	G+Q	⋯	2.72	0.83	0.21	−0.89	−1.12	SS	4.2	<36.0	4.9/VLA-A	LSO	N
J0915+1018	⋯	G+Q	⋯	0.97	0.35	0.18	−0.76	−0.56	SS	1.9	<16.5	4.9/VLA-A	LSO	Y
J0917+4725	⋯	G+Q	⋯	1.21	0.35	0.13	−0.91	−0.81	SS	0.58	<4.96	4.9/VLA-A	SL	N, I
J0920+1753	0.68*	G	Sc	3.45	1.08	0.27	−0.86	−1.11	SS	0.42	∼2.97	4.9/VLA-A	MSO	Y
J0920+2714	⋯ [c]	G	S0	1.60	0.46	0.13	−0.93	−1.04	SS	2.9	<24.7	4.9/VLA-A	LSO	Y, I
J0939+0304	0.34*	G	S0	0.75	0.47	0.23	−0.35	−0.56	FS:	0.23	∼1.11	1.4/VLBI	CJ	Y
J0945+2640	⋯	Q	⋯	1.56	0.57	0.20	−0.74	−0.86	SS	5.3	<45.7	4.9/VLA-A	LSO	N
J0951+1154	0.65*	G	Sc	1.25	0.37	0.11	−0.90	−0.99	SS	2.9	∼20.1	4.9/VLA-A	LSO	N
J1008+2401	0.62*	G	Sc	1.36	0.43	0.12	−0.85	−1.05	SS	2.0	∼13.6	4.9/VLA-A	MSO	Y
J1010+4159	0.71*	G	Sc	1.40	0.42	0.14	−0.90	−0.88	SS	0.27	∼1.90	1.66/VLBI	MSO	Y
J1019+4408	⋯	Q+abs	⋯	1.04	0.34	0.07	−0.82	−1.27	SS	0.16	<1.33	1.66/VLBI	CSO	Y
J1023+0424	0.71*	G	Sc	0.90	0.33	0.11	−0.75	−0.89	SS	0.56	∼4.03	8.5/VLA-A	MSO	Y
J1033+3935	1.095 :	G	Sc	0.82	0.41	0.65	−0.52	0.37	FS	0.005	0.039	5/VLBI	CJ	Y
J1034+1112	⋯	G+Q	⋯	4.59	1.21	0.36	−0.99	−0.98	SS	4.9	<41.7	4.9/VLA-A	LSO	N
J1043+0537	0.42*	G	E	2.67	0.67	0.20	−1.03	−0.97	USS	6.6	∼36.5	4.9/VLA-A	LSO	N
J1045+0455	⋯	Q+abs	⋯	1.18	0.38	0.14	−0.84	−0.82	SS	2.9	<24.8	4.9/VLA-A	LSO	N
J1048+3457	1.594	Q+abs	⋯	2.44	1.05	0.38	−0.63	−0.81	SS	0.045	0.385	1.4/VLBI	CPLX	Y
J1120+2327	1.819	Q	⋯	5.48	1.38	0.36	−1.02	−1.09	USS	4.5	38.4	4.9/VLA-A	LSO	N
J1125+1953	⋯	Q	⋯	1.60	0.43	0.15	−0.98	−0.83	SS	0.47	<4.02	4.9/VLA-A	CJ	Y
J1127+5743	0.49*	G	Sb	1.70	0.65	0.19	−0.71	−1.00	SS	0.49	∼2.95	8.5/VLA-A	MSO	Y
J1129+5638	0.892	G	Sa	1.25	0.50	0.12	−0.68	−1.16	SS	0.080	0.622	1.4/VLBI	CSO:	Y
J1142+0235	0.37*	G	Sa	0.89	0.38	0.20	−0.63	−0.50	SS ✓	1.5	∼7.67	4.9/VLA-A	MSO	Y
J1147+4818	⋯	Q	⋯	1.89	0.50	0.12	−0.99	−1.18	SS	1.0	<8.32	4.9/VLA-A	CJ/GA	Y, I:
J1148+1404	0.54*	G	Sc	1.00	0.33	0.10	−0.84	−0.97	SS	1.5	∼9.29	4.9/VLA-A	MSO	Y
J1202+1207	⋯	G+Q	⋯	1.01	0.37	0.16	−0.75	−0.69	SS	0.098	<0.840	1.4/VLBI	CSO:	Y
J1203+4632	0.36*	G	E	0.52	0.42	0.20	−0.17	−0.58	GPS	0.040	∼0.200	5/VLBI	CSO:	Y
J1207+5407	0.61*	G	Sc	2.58	0.60	0.16	−1.09	−1.05	USS	1.4	∼9.74	4.9/VLA-A	MSO	Y
J1215+1730	0.268	Q+abs	⋯	2.40	1.03	0.62	−0.63	−0.41	SS ✓	0.14	0.551	5/VLBI	CSO:	Y
J1228+5348	⋯	G+Q	⋯	1.94	0.53	0.15	−0.96	−1.02	SS	4.9	<41.7	4.9/VLA-A	LSO	N
J1238+0845	0.65*	G	Sc	1.25	0.41	0.08	−0.82	−1.32	SS	3.2	∼22.0	4.9/VLA-A	LSO	N
J1300+5029	1.561	Q	⋯	0.67	0.38	0.39	−0.43	0.03	FS	0.10	0.855	4.9/VLA-B	CJ	Y
J1312+1710	0.63*	G	Sc	0.95	0.34	0.11	−0.78	−0.90	SS	0.056	∼0.385	1.4/VLBI	CSO:	Y
J1315+0222	0.85*	G	Sc	1.33	0.52	0.16	−0.70	−0.93	SS	2.4	∼18.2	4.9/VLA-A	LSO	Y
J1341+1032	⋯	Q+abs	⋯	2.62	0.69	0.17	−1.00	−1.12	USS	1.0	<8.72	4.9/VLA-A	MSO	Y, I:
J1345+5846	⋯	G+Q	⋯	1.81	0.42	0.12	−1.08	−1.00	USS	2.3	<19.3	4.9/VLA-A	LSO	N
J1347+1217	0.122	G	Sa	8.31	4.86	3.09	−0.40	−0.36	FS	0.10	0.217	1.66/VLBI	CSO	Y
J1348+2415	2.879	Q	⋯	2.74	0.56	0.14	−1.19	−1.14	USS	3.0	23.8	4.9/VLA-A	LSO	N
J1354+5650	0.65*	G	Sc	1.86	0.72	0.28	−0.71	−0.76	SS	2.5	∼17.4	4.9/VLA-A	LSO	N
J1357+0046	⋯	G+Q	⋯	4.74	2.00	0.49	−0.64	−1.11	SS	0.086	0.647	1.4/VLBI	CSO:	Y
J1410+4850	0.592	G+Q	⋯	0.76	0.33	0.11	−0.63	−0.86	SS	0.043	0.284	1.4/VLBI	CSO:	Y

Table 2
(Continued)

Object	z	SED Type	G Type	S_{365} (Jy)	$S_{1.4}$ (Jy)	$S_{4.9}$ (Jy)	α_l	α_h	Spec. Type	LAS ($''$)	LLS (kpc)	Freq.(GHz)/ Telescope	Morph.	EVAL
(1)	(2)	(3)	(4)	(5)	(6)	(7)	(8)	(9)	(10)	(11)	(12)	(13)	(14)	(15)
J1413+1509	0.22*	G	S0	<0.25	0.50	0.41	>0.52	−0.16	GPS ✓	0.015	∼0.051	5/VLBI	CSO	Y
J1414+4554	0.38*	G	S0	0.40	0.41	0.21	0.02	−0.53	GPS	0.031	∼0.162	5/VLBI	CSO	Y
J1415+1320	0.247	G	Sb	2.74	1.18	0.84	−0.63	−0.27	FS	0.12	0.450	1.66/VLBI	CSO	Y
J1421−0246	0.49*	G	E	1.73	0.55	0.16	−0.85	−0.97	SS	3.5	∼21.2	4.9/VLA-A	LSO	N
J1424+1852	⋯	Q+abs	⋯	2.69	0.70	0.19	−1.00	−1.06	USS	1.6	<13.8	4.9/VLA-A	MSO	Y
J1502+3753	⋯	Q+abs	⋯	1.11	0.34	0.12	−0.89	−0.81	SS	2.0	<17.5	4.9/VLA-A	LSO	N
J1504+5438	0.621	G	Sc	0.78	0.38	0.17	−0.53	−0.64	SS	0.002	0.014	5/VLBI	PS	Y
J1504+6000	1.024	Q	⋯	5.22	1.55	0.44	−0.90	−1.01	SS	0.62	4.98	8.5/VLA-A	MSO	Y
J1523+1332	⋯	Q+abs	⋯	1.59	0.35	0.11	−1.13	−0.92	USS	3.7	<32.0	4.9/VLA-A	LSO	N
J1527+3312	0.32*	G	Sb	0.75	0.32	0.11	−0.64	−0.89	SS	0.13	∼0.601	8.5/VLA-A	CPLX	Y
J1528−0213	0.54*	G	E	1.06	0.47	0.16	−0.61	−0.85	SS	1.4	∼8.79	4.9/VLA-A	MSO	Y
J1548+0808	0.51*	G	E	1.79	0.63	0.21	−0.78	−0.89	SS	0.25	∼1.51	1.4/VLBI	MSO	Y
J1551+6405	⋯	G+Q	⋯	0.59	0.68	0.21	0.10	−0.96	GPS	0.074	<0.630	5/VLBI	CJ	Y
J1559+4349	1.232	Q+abs	⋯	2.08	0.75	0.19	−0.76	−1.12	SS	0.79	6.62	4.9/VLA-A	MSO/GA	Y, I:
J1604+6050	0.559	G	S0	0.64	0.59	0.20	−0.06	−0.88	GPS	0.014	0.089	1.4/VLBI	CSO:	Y
J1616+2647	0.755	G	Sc	1.71	1.41	0.70	−0.14	−0.56	GPS	0.12	0.915	1.4/VLBI	CSO	Y
J1625+4134	2.550	Q	⋯	2.47	1.72	1.36	−0.27	−0.19	FS	0.006	0.049	5/VLBI	CJ	Y
J1629+1342	0.74*	G	Sc	1.95	0.71	0.23	−0.75	−0.92	SS	5.1	∼37.4	4.9/VLA-A	LSO	N
J1633+4700	⋯	Q+abs	⋯	1.46	0.46	0.15	−0.87	−0.91	SS	5.2	<44.5	4.9/VLA-A	LSO	N
J1724+3852	1.542	Q+abs	⋯	0.88	0.37	0.14	−0.64	−0.77	SS	0.040	0.340	1.4/VLBI	CSO:	Y
J2203−0021	0.729	G	Sc	1.71	0.61	0.18	−0.77	−0.98	SS	0.88	6.38	4.9/VLA-A	MSO	Y

Notes. Columns list: (1) object name; (2) redshift, where suffix "*" indicates a photometric redshift fit by its optical+NIR SED in Paper I, and the suffix ":" means the redshift is uncertain; (3) the optical+NIR SED type from Paper I; (4) the Hubble type for pure "G"-type objects in column (3); (5) the flux density at 365 MHz; (6) the flux density at 1.4 GHz; (7) the flux density at 4.9 GHz; (8) the low-frequency spectral index (α_l) between 365 MHz and 1.4 GHz; (9) the high-frequency spectral index (α_h) between 1.4 and 4.9 GHz; (10) the radio spectral classification, where the check mark ✓ means the classification has been modified using additional information to the spectral indices in columns (8) and (9). Classifications include SS = Steep Spectrum, FS = Flat Spectrum, USS = Ultra-Steep Spectrum, and GPS = Giga-Hertz Peak Spectrum; (11) the largest angular size (LAS) in arcsecs between major components; (12) the largest linear size (LLS) in kpc, where "∼" means a photometric redshift is used and "<" means $z = 1.6$ is used to obtain the largest size possible, (13) frequency and telescope with which the LAS and LLS are measured; (14) radio source morphological classification, where CPLX means complex, CJ means core-jet, GA means gravitational arc, PS means point source, SL means single lobe, and CSO: means CSO candidates; (15) an evaluation (EVAL) of whether the object remains a good candidate for an absorption-line search at radio frequencies (Y or N) and whether it is an intervening system (I) or candidate (I:).

[a] The redshift listed is for a background radio source that has an SDSS detected Galaxy in the foreground.

[b] The redshift listed is for a background radio source that is gravitationally lensed by a foreground Galaxy at $z = 0.349$.

[c] This is an intervening system with a foreground Galaxy at $z = 0.206$. The radio source redshift is unknown.

During the transitional period, there were problems in VLA-EVLA baselines, including phase jumps and closure errors. Among the 27 antennas, 10 were EVLA antennas in 2007 June and July and 11 in 2007 August. EVLA antennas were excluded for the 4.9 GHz reduction in AIPS. Therefore the sensitivity is reduced by a factor of ∼1.6.

We used the VLBA to obtain 1.4 GHz images for sources that are unresolved or have compact components in VLA-A images (project # BY0020). Overall, 36 sources were observed in 2009 December and 2010 January. The observations were centered at 1.446 GHz with an effective bandwidth of 32 MHz in full polarization. To achieve best *uv*-coverage for each object, ∼15 minute observing scans were conducted at three well-separated hour angles over a time span of 3–10 hr. The target source was phase-referenced every 4–5 minutes by a phase calibrator within 5° on the sky. The data reduction of the VLBA observations was carried out in AIPS following standard calibration and imaging procedures. The flux density scales of these data were set using the online measurements of the antenna gains and system temperatures.

The observing log is shown in Table 1, along with brief comments about individual observations. For the archive data, if an image is available in the literature the reference paper is cited; otherwise we processed the archive data ourselves and cite the project ID as a reference in Table 1. The flux density calibrator is completely flagged or not observed for three objects at 4.9 GHz and two objects at 8.5 GHz. In these cases, a rough flux density calibration was made by setting the flux density of the phase calibrator to its flux density reported in the VLA Calibrator Manual. One object at 4.9 GHz and five objects at 1.4 GHz are not detected, which means either that the object is too faint/extended to be detected, or that a few of the shortest baselines have a signal but are not sufficient to make a synthesized image. The data for one object at 4.9 GHz are completely flagged. These sources are identified in the tables in the Appendix.

We have an almost complete set of VLA-A 4.9 GHz images from our own data, the literature, and archive data processed by us. A few exceptions without VLA-A images are objects that have been well-studied or proven to be unresolved in VLA-A 8.5 GHz images, and so are likely unresolved at 4.9 GHz as well. The 8.5 GHz data are summarized in Table 1 including our own data, as well as data from the literature or archives that would help us understand the nature of the source. In other words, if a source was of little interest for this project based on its VLA-A 4.9 GHz image (for example, consisting of two

Table 3
Summary of CSOs and CSO Candidates

Object	z	LAS (mas)	LLS (pc)	z References	CSO References	Status
(1)	(2)	(3)	(4)	(5)	(6)	(7)
J0134+0003	0.879	18[a]	140	(5)	(3)	?
J1129+5638	0.892	80	622	(1)	This work	?
J1202+1207	⋯	98	<840	⋯	This work	?
J1203+4632	0.36*	40	∼200	(2)	(12)	?
J1215+1730	0.268	135[b]	551	(12)	(12)	?
J1312+1710	0.63*	56	∼385	(2)	This work	?
J1357+0046	⋯	86	<738	⋯	This work	?
J1410+4850	0.592	43	284	(1)	This work	?
J1604+6050	0.559	14	89	(1)	This work	?
J1724+3852	1.542	40	340	(1)	This work	?
J1019+4408	⋯	155[c]	<1326	⋯	(4)	Y
J1347+1217†	0.122	100[d]	217	(6)	(10), (13), (8)	Y
J1413+1509	0.22*	14[b]	∼49	(2)	(12)	Y
J1414+4554	0.38*	31[b]	∼160	(2)	(7)	Y
J1415+1320†	0.247	117[e]	450	(11)	(9), (7)	Y
J1616+2647	0.755	124	915	(1)	This work	Y

Notes. The two sections separated by a horizontal line summarize the 10 CSO candidates (at top) and the 6 previously known/confirmed CSOs (at bottom). Columns list: (1) object name; (2) redshift, where suffix "*" indicates photometric redshift fit by optical-NIR SED in Paper I; (3) largest angular size (LAS) between major components in milliarcsecs; (4) largest physical size (LLS) in parsecs, where "∼" means a photometric redshift is used and "<" means $z = 1.6$ is assumed because no good redshift estimate is available; (5) redshift reference; (6) CSO reference; (7) status, where "?" indicates a CSO candidate and "Y" means confirmed CSO.
[a] Measured at 2.3 GHz (Beasley et al. 2002).
[b] Measured at 5 GHz (Helmboldt et al. 2007).
[c] Measured at 1.66 GHz (Dallacasa et al. 2002b).
[d] Measured at 1.66 GHz (Xiang et al. 2002).
[e] Measured at 1.66 GHz (Perlman et al. 1996).
References. (1) Spectroscopic redshift (Paper I), (2) photometric redshift derived by fitting the optical–NIR SED (Paper I), (3) Beasley et al. (2002), (4) Dallacasa et al. (2002b), (5) Drinkwater et al. (1997), (6) Grandi (1977), (7) Gugliucci et al. (2005), (8) Lister et al. (2003), (9) Perlman et al. (1996), (10) Stanghellini et al. (2001), (11) Stocke et al. (1992), (12) Tremblay (2011), (13) Xiang et al. (2002).

well-separated lobes with an optical/NIR source right between them), we did not process its archive data.

3.2. Observational Results

The basic observational results of this study are detailed in the Appendix, including high resolution and dynamic range VLA and VLBA maps of these sources, as well as measurements of the component fluxes, sizes, and locations. In this section, we use the basic data from the Appendix to investigate the systematic relationships between the radio source sizes, morphologies and spectral indices, and optical-NIR morphologies and SEDs.

3.2.1. Morphological Classification of Radio Images

We find that 52 out of the 80 sources are compact or have compact components with size $<0\farcs5$ and flux density >0.1 Jy at 4.9 GHz. Another 29 objects are unresolved in VLA-A images and their morphological types are determined only by the VLBA observations.

In Table 2, we compile the optical-NIR properties of each source and the basic radio data from the Appendix. For each source we list the spectroscopic or revised photometric redshift if available, the optical+NIR SED types, and Hubble types in columns (2), (3), and (4), respectively. The optical+NIR SEDs were divided into four classes in Paper I: quasar (Q), quasar with extinction signatures in the bluer bands (Q + abs), galaxy with a quasar signature in the bluer bands ($G + Q$), and pure galaxy (G). We fit the G-type objects with template spectra of five Hubble types (E, S0, Sa, Sb, and Sc), and give the best-fit Hubble types in column (4) (see Paper I for the details of the procedure used). Also in Paper I, we used the SDSS photometry and our newly acquired APO NIR photometry to determine more accurate photometric redshifts for G sources only; these revised $z_{\rm phot}$ values are listed in column (2) with asterisks. Radio continuum flux densities are listed at three frequencies in columns (5)–(7), followed by the low-frequency (between 365 MHz and 1.4 GHz) spectral index in column (8), and the high-frequency spectral index (between 1.4 and 4.9 GHz) in column (9). Column (10) lists the abbreviated spectral type of the source (SS = steep spectrum, USS = ultra-steep spectrum, GPS = Giga-Hertz Peaked Source, and FS = flat spectrum). Each object's largest angular size (LAS) in arcsecs is listed in column (11) and its largest linear size (LLS) in kpc is in Column (12). Because radio source size is frequency and resolution dependent, we also list the observing frequency and telescope/configuration in Column (13) for these measurements. When an object's spectroscopic redshift is not available, its photometric redshift is used to estimate its linear size. In Paper I we fit photometric redshifts and Hubble types from optical+NIR SEDs for objects with galaxy-like SEDs; in these cases, the redshift uncertainties are ±0.1–0.2. For objects with a quasar-like signature in their optical+NIR SEDs, due to the uncertain amount of quasar contribution and extent of obscuration, it is not possible to derive a reliable photometric redshift. In this case, an upper limit on LLS is set by using the maximum angular scale possible over cosmic time, 8.6 kpc/″ at $z \sim 1.6$.

Table 4
Statistics of Morphological Types and Radio Spectral Types

Radio SED\Morphology		CJ	CSO	MSO	LSO	PS	CPLX
		8	16	19	23	2	3
FS	7	5	2	0	0	0	0
GPS	8	1	6	0	0	1	0
SS	47	2	8	15	18	1	3
USS	9	0	0	4	5	0	0

Note. This table shows the number of objects with a particular morphological type and radio spectral type. The row header lists morphological types and the column header lists spectral types. The total number of objects for each type are shown in the first row and the first column.

Table 5
Statistics of Radio Morphologies and Optical+NIR SEDs

OIR SED\Morphology		CJ	CSO	MSO	LSO	PS	CPLX
		8	16	19	23	2	3
G	37	3	10	12	8	2	2
G+Q	16	2	3	3	8	0	0
Q+abs	11	0	3	3	4	0	1
Q	7	3	0	1	3	0	0

Note. This table shows the number of objects with a particular radio morphology and optical+NIR SED. The row header lists radio morphological types and the column header lists optical+NIR SED types. The total number of objects for each type are shown in the first row and the first column.

Most of the objects show classic double-lobe structure with or without a core. The separation of the two lobes ranges from tens of parsecs to tens of kpcs. We adopt the terminology introduced by Fanti et al. (1995) to indicate an LLS of $>$15 kpc, 15 kpc to 1 kpc, and $<$1 kpc with the terms Large Symmetric Object (LSO), Medium-size Symmetric Object (MSO), and Compact Symmetric Object (CSO), respectively. In general, 1 kpc is considered a typical size for the narrow-line emission regions around an AGN, and 15 kpc is a typical size for the visible portions of the faint optical host galaxies in this sample. We find 24 LSOs, 22 MSOs, and 16 CSOs in the sample. LSOs are classic FRI or FRII radio galaxies (Fanaroff & Riley 1974) with extended radio emission that expands to scales much larger than their host galaxies. These objects are not likely to be intrinsic absorbers due to their extended structure and large scale, unless a strong core is present. In contrast, MSOs and CSOs are better candidates because of their compact structure and small scale close to the gas-rich galaxy with which they are identified. However, from its morphology at one band alone, a CSO can hardly be discriminated from a core-jet object with multiple jet components if small-scale spectral index data is lacking. Therefore, 10 of the CSOs remain candidates because multi-wavelength and multi-epoch observations are necessary to characterize "bona-fide" CSOs. CSOs are discussed in detail in Section 3.2.2.

If the jet of a radio source axis is oriented toward us, the radiation close to the core could be strongly boosted due to relativistic beaming of the jet. The radio structure of these sources generally consists of a compact core and some extended jet components aligned on one side of the core (core-jet [CJ] morphology). Sometimes a weak counterjet is also detected. These are also good candidates for absorption-line searches, given their very compact structure.

Morphological classifications are listed in Column (14) of Table 2. Except for the double-lobe and core-jet types mentioned above, there are four minor types: single-lobe [SL], gravitational-arc [GA], complex [CPLX], and point-source [PS] objects. J0834+1700 and J0917+4725 have a single, extended component in their VLA-A images. We classify them as SL objects because they are very likely one of the two lobes in a classic double-lobe structure. J0751+2716 is a GA system with an arcuate shape to its radio image (Lehar et al. 1997). We find two more objects showing potential gravitational arcs: J1147+4818 and J1559+4349. Four objects are classified as CPLX objects for their atypical morphologies. All the above sources will be discussed in detail in subsequent sections. The point-source (PS) objects, J0901+0304 and J1504+5438, are unresolved in their VLBA images and are most likely core-jet objects without the jet components detected separately.

Column (15) is our overall evaluation ("EVAL") concerning the likelihood for a radio absorption line to be present based primarily upon the compactness of the radio emission. Approximately 70% of these sources appear to be good candidates ("Y" in column (15)) for absorption searches once spectroscopic redshifts are in-hand. Intervening ("I") and possibly intervening ("I:") galaxies are also good candidates for absorption-line searches.

3.2.2. Compact Symmetric Objects

CSOs are luminous radio galaxies that have a symmetrical, double-lobe structure fully contained within 1 kpc. Rather than "frustrated" jets obstructed by a dense interstellar medium (ISM), CSOs are now believed to be young objects with age $\lesssim 10^4$ year that will evolve into classical FRI or FRII radio galaxies (Fanti et al. 1995; Begelman 1996; Readhead et al. 1996). The hotspot advance speed of CSOs is found to be sub-luminal (Owsianik & Conway 1998) with nearly equal-brightness extended lobes, which is in sharp contrast to the core-jet objects. CSOs also have low flux variability and low polarization. All of these are consistent with the speculation that the jets are propagating nearly perpendicular to the line of sight (Readhead et al. 1996). While CSO candidates are often selected based on their morphologies in one band, it is preferred that a flat spectrum or inverted core between two symmetric lobes is identified using multi-wavelength observations. Because the cores of CSOs are often weak or undetected, the advance speed of hotspots and jet components can be measured to make sure that there is no strong projection effect (i.e., no apparent superluminal motion as in the core-jet sources). The detection rate of H I 21 absorption is exceptionally high in CSOs, 30%–50% (e.g., Pihlström et al. 2003; Gupta et al. 2006), which may at least in part be due to their very compact radio structure (Curran & Whiting 2010). One of the two known intrinsic atomic and molecular absorbers, J1415+1320, is a CSO (Perlman et al. 1996, 2002). The high frequency of occurrence of H I absorption in CSOs may be due to them having physical sizes (10 pc to 1 kpc) that are comparable in size to the absorbing screen (Curran et al. 2013). Thus, identification of CSO candidates in this sample is

Table 6
Statistics of Optical+NIR SEDs and Radio Spectral Types

OIR SED\Radio SED		FS	GPS	SS	USS
		7	8	47	9
G	37	4	7	24	2
G+Q	16	1	1	13	1
Q+abs	11	0	0	7	4
Q	7	2	0	3	2

Note. This table shows the number of objects with a particular optical-NIR SED type and radio SED type. The row header lists radio SED types and the column header lists optical-NIR SED types. The total number of objects for each type are shown in the first row and the first column.

an important step toward discovering new H I and molecular absorption systems.

There are five previously known CSOs in our sample (see Table 3; previously known CSOs are listed below the solid line in this table). J1019+4408 was observed by Dallacasa et al. (2002b) at 1.67 GHz and exhibits all the typical CSO features in morphology (i.e., symmetric, edge-brightened, and S-shaped lobes). J1347+1217 is an ultra-luminous infrared galaxy at $z = 0.122$ in an ongoing merger. It was observed using VLBI by Stanghellini et al. (1997) at 5 GHz, and the presence of a core was confirmed by Stanghellini et al. (2001) at 15 GHz and Xiang et al. (2002) at 1.66 GHz, although the luminosities of the two lobes are quite asymmetrical, especially at higher frequencies. Lister et al. (2003) found that J1347+1217 has atypical CSO features, including superluminal motions and large linear polarization, suggesting a small angle relative to the line of sight. H I 21 cm absorption is detected toward the weak lobe (Morganti et al. 2004).

J1413+1509 was classified by Helmboldt et al. (2007) as a CSO candidate at 5 GHz and later confirmed by Tremblay (2011) using VLBI observations at 4.8, 8.3, and 15 GHz. J1414+4554 also has typical CSO morphology; Gugliucci et al. (2005) did not detect motions between the two hotspots from 1997 to 2002 and set an upper limit of 0.014 mas yr^{-1}. This indicates a relative projected velocity of $\leqslant 0.24\ c$, assuming a photometric redshift $z = 0.38$ (Paper I). J1415+1320 is an atomic and molecular absorber at radio frequencies. Perlman et al. (1996) identified the core using multi-frequency VLBI observations. Gugliucci et al. (2005) measured the motion of the hotspots and estimate an age as young as 130 ± 47 year for this CSO.

We identified a new CSO (J1616+2647 with typical CSO morphology, an extended double-lobed morphology with, at best, a very weak core; see its VLBA map in the Appendix) and 10 new CSO candidates (CSO: in Column 15 in Table 2 and all listings above the solid line in Table 3). They are all compact in 8.5 GHz VLA-A images (i.e., there is no extended flux detected at or larger than the $\sim 0\farcs1$ level). For 9 of the 10 objects, 70%–85% of the flux density detected by the FIRST survey is accounted for in our 1.4 GHz VLBA images. J1312+1710 has only 52% of its FIRST flux detected, indicating it may have a second set of weak lobes further out from the core.

Since we lack spatially resolved multi-frequency VLBA images and/or very accurate optical-NIR/radio astrometry, we cannot unambiguously identify the core component in these sources either by its flat or inverted spectral index or its position with respect to the host galaxy. This means that in most cases (all but J1616+2647) a CSO morphology cannot be distinguished from a CJ morphology. Until better VLBA maps and/or multi-epoch VLBA maps become available, the 10 sources listed above the line in Table 3 remain CSO candidates.

Three of our CSO candidates were previously observed with VLBA. J0134+0003 was observed in the VLBA Calibrator Survey by Beasley et al. (2002). J1215+1730 and J1203+4632 were selected by Helmboldt et al. (2007) as CSO candidates in five GHz VLBA maps. Tremblay (2011) claim there is no structure seen in the counterjet of J1215+1730 and refute it as a CSO candidate. But we still consider it a candidate based on our CSO-selection criteria.

Once all 10 CSO candidates are confirmed, the frequency of CSO occurrence in this sample will be ~20%, nearly three higher than the 7.5% identification rate found by Polatidis et al. (1999) in a flux-limited sample with flux density $\geqslant 0.7$ Jy at 5 GHz. While selecting at high frequencies tends to include more compact objects than at low frequencies, our selection frequency is 1.4 GHz compared to 5 GHz in Polatidis et al. (1999). We show in Section 3.3 that most of the CSO candidates have multi-band properties that are consistent with typical CSOs, implying a very high success rate of CSO selection. The high CSO detection rate might be caused by our selection of non-elliptical galaxies, which is consistent with the fact that the disturbed optical structure is often seen in nearby CSOs (Perlman et al. 2001). Once confirmation of these CSO candidates is obtained, our sample will have returned a much higher frequency of CSOs than other selection techniques.

3.2.3. Radio SED Types

To classify radio SEDs, flux densities at three frequency bands are used: 365 MHz, 1.4 GHz, and 5 GHz. The Texas Survey of Radio Sources at 365 MHz (Douglas et al. 1996) detected all objects in the sample except J1413+1509, for which the flux density limit of the survey, 25 mJy, is used as an upper limit. Flux densities at 1.4 GHz from the FIRST survey are compared with those from other lower-resolution (45″) surveys, such as the NRAO VLA Sky Survey (Condon et al. 1998), to make sure all the flux is accounted for by FIRST. In fact, the differences are all within ~10%, comparable to the uncertainties. At 5 GHz, all the sources with declination higher than 2°.5 are in the 87 GB catalog of radio sources (Gregory & Condon 1991). For those lower than 2°.5, flux densities at 5 GHz are cited from the Parkes-MIT-NRAO surveys (Griffith et al. 1994, 1995) or the Parkes Catalog (Wright & Otrupcek 1990). Flux densities of the three bands are listed in Columns (5)–(7) of Table 2.

We define α_l ("l" for low) as the spectral index between 365 MHz and 1.4 GHz, and α_h as between 1.4 and 5 GHz ($S_\nu \propto \nu^\alpha$). While slightly different criteria are adopted by different authors, the following empirical criteria are commonly used at the aforementioned frequencies: flat-spectrum (FS) objects ($\alpha_h \geqslant -0.5$; e.g., Healey et al. 2007), steep-spectrum (SS) objects ($\alpha_h < -0.5$ and $\alpha_l < -0.5$), gigahertz-peaked-spectrum (GPS) objects ($\alpha_h < -0.5$, $\alpha_l \geqslant -0.5$, and $\alpha_l - \alpha_h \geqslant 0.3$; e.g., O'Dea 1998), and ultra-steep-spectrum (USS) objects ($\alpha_l \leqslant -1.0$; e.g., Roettgering et al. 1994). In Table 2, α_l and α_h are shown in Columns (8) and (9), respectively, with the inferred radio SED type in Column (10).

Our spectral classification scheme described above can be interpreted in terms of turnover frequency: $\nu_m \lesssim 400$ MHz for SS objects and $\nu_m \gtrsim 400$ MHz for GPS objects. A small

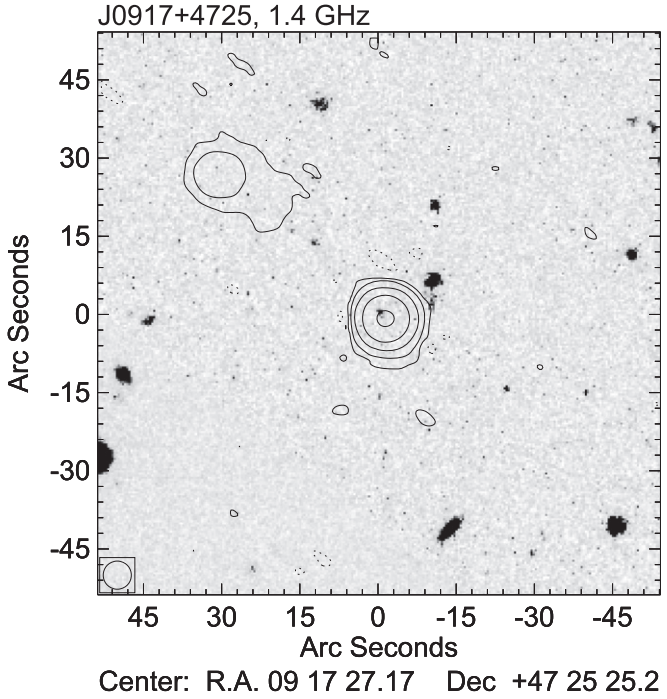

Figure 1. The 1.4 GHz FIRST flux contours of the field of J0917+4725 overlaid with an optical *r*-band SDSS image. The radio contour levels are −0.45, 0.45, 2.3, 11, 54, and 267 mJy.

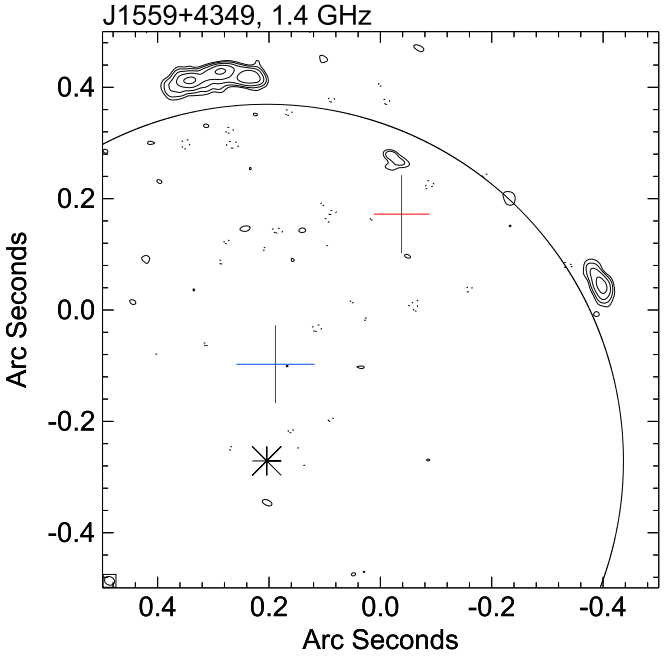

Figure 2. The 1.4 GHz VLBA contours of J1559+4349. The black arc is part of a circle with radius 0.″64 centered at the position labeled with an asterisk. The NIR centroid is shown as a red cross, while the optical *r*-band centroid is shown as a blue cross. (This plot is otherwise the same as the 1.4 GHz plot in the Appendix.)

fraction of SS objects are USS with $\alpha < -1.0$ due to extreme energy loss that is probably caused by electron depletion or inverse-Compton radiation. It has been found that USS objects are excellent candidates for finding high-z radio galaxies (Miley & De Breuck 2008). When the radiation becomes opaque at a range of physical sizes, the spectrum has a shallower and often bumpy character, which makes it an FS object.

We have double-checked the radio SED types using flux densities measured from other radio frequencies, with help from the NASA/IPAC Extragalactic Database (NED). Two FS objects, J0901+0304 and J1413+1509, are reclassified as GPS objects because their turnover frequencies (ν_m) are between 5 and 8.5 GHz. Two FS objects, J1215+1730 and J1142+0235, are reclassified as SS because their SEDs are straight from 365 MHz to 8.5 GHz with $\alpha \simeq -0.5$. One GPS object, J0843+4215, is reclassified as SS because $\nu_m \leqslant 500$ MHz with $\alpha_l = -0.4$ and $\alpha_h = -0.7$. However, one object, J0939+0304, does not fall into any of the four categories listed above. It has $\alpha_h < -0.5$, $\alpha_l > -0.5$, and $(\alpha_l - \alpha_h) < 0.3$. Flux densities at higher or lower frequencies are needed to pin down the SED types of objects like J0939+0304. It could be either FS or GPS because no flux density is available >5 GHz, so it is marked as "FS:."

Overall, there are seven FS objects, eight GPS objects, forty-seven SS objects, nine USS objects, and one uncertain object (FS or GPS?). The reliability of the original classification method is 60% for FS objects and 83% for GPS objects. A spectral index between ∼1 and ∼10 GHz might be a better choice for α_h to classify FS and GPS objects than the spectral index between ∼1 GHz and ∼5 GHz used here. For SS and USS objects, 100% are indeed steep spectrum, although the critical spectral index −1.0 is rather arbitrarily chosen. The radio spectral types are shown in Column (10) of Table 2.

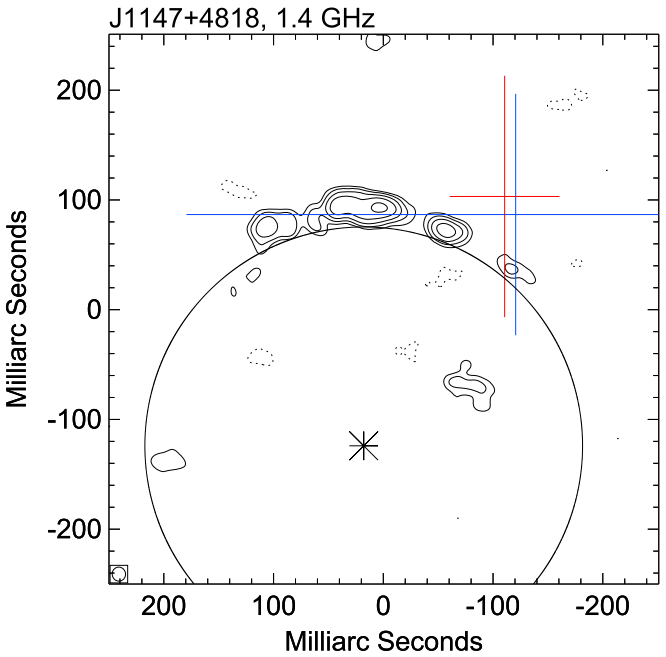

Figure 3. The 1.4 GHz VLBA contours of J1147+4818. The black arc is part of a circle with radius 0.″20 centered at the position labeled with an asterisk. The blue and red crosses are the SDSS *r*-band and NIR centroids, respectively. (This plot is otherwise the same as the 1.4 GHz plot in the Appendix.)

3.3. Statistical Properties of the Radio Continuum Emission

In this section we study the statistical properties of our sample, including radio morphologies, radio SEDs, and optical +NIR SEDs in order to identify correlations between different types of sources that would make eventual redshifted H I 21 cm absorption searches more effective. To study a homogeneous

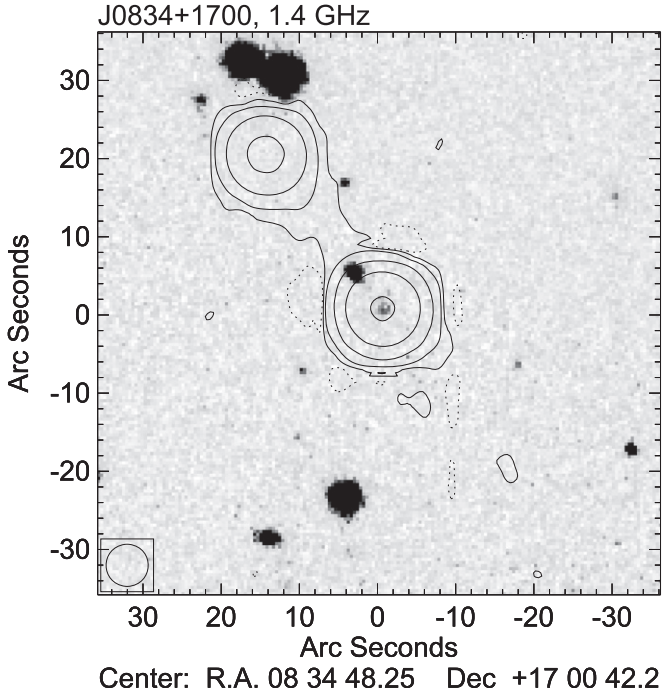

Figure 4. The 1.4 GHz contour of the field of J0834+1700 overlaid with optical image in the SDSS *r*-band. The radio contour levels are −0.9, 0.9, 5.5, 33, 203, and 1239 mJy.

sample with only intrinsic obscuration (and possible related absorption), systems with intervening galaxies need to be excluded. Column (15) of Table 2 lists four intervening systems and five suspect objects (see Sections 3.4.1–3.4.3 for more details). Excluding these nine objects gives us a statistical sample of seventy-one objects with which to study source systematics.

3.3.1. Radio Morphologies and SEDs

We summarize the number of objects with each radio morphological type and SED type in Table 4. The following statistical trends are clearly shown in the data.

1. There is not a single MSO or LSO among the FS and GPS objects. This implies that $\nu_m \gtrsim 1$ GHz almost guarantees a small-scale core-jet object, CSO, or unresolved source. On the other hand, 75% of the core-jet objects and 50% of the CSOs are FS or GPS objects.
2. FS objects are mostly or all core-jet objects (at least five out of seven).
3. Most of the GPS objects (six out of eight) are CSOs. As previously noted, GPS objects are an excellent source for finding CSOs (Stanghellini et al. 1997; Liu et al. 2007).
4. Steep spectrum (SS) CSOs have a larger median size (622 pc) than GPS CSOs (162 pc). Meanwhile, most of the SS CSOs have $\nu_m \sim 365$ MHz to 1.4 GHz, which means that ν_m varies inversely with size. This correlation has been found previously, both in a sample of CSOs and MSOs (Fanti et al. 1990) and in a sample of Compact Steep Spectrum (CSS) and GPS sources (O'Dea & Baum 1997). While this trend could also apply to MSOs and LSOs, their inferred ν_m shifts to frequencies lower than the 365 MHz band and so cannot be verified using current data.
5. Double-lobe sources in the sample have $\nu_m < 10$ GHz and their sizes are inversely proportional to ν_m, while FS objects have no turnover frequency up to at least 10 GHz (O'Dea 1998). It is also worth noting that the intervening systems/candidates are exclusively SS objects, that is, the radio sources in these systems are of the most common variety, unlike those with intrinsic obscurations.

The presence in the current sample of the same trends found in more traditionally defined samples means that these radio sources are all examples of previously known types, not some new radio morphology associated only with gas-rich systems. However, some of these types (e.g., CSOs) are greatly favored by the novel selection method used here (i.e., selecting radio sources by their host galaxy's optical morphology).

3.3.2. Radio Morphologies and Optical+NIR SEDs

Similar to Table 4, Table 5 summarizes the number of objects with a particular radio morphology and optical+NIR SED type (see Paper I for a list of these types and details of their determination). We find the following statistical tendencies in the sample.

1. Core-jet (CJ) objects have a high percentage (∼60%) of quasar-type SEDs (Q, Q + abs, and $G + Q$). Because our sample-selection criteria were meant to exclude sources with stellar counterparts, the actual fraction of CJ sources that are quasars is much higher in traditionally selected samples. As expected, this indicates that CJ objects are predominantly unobscured quasars; the few found in this sample are present either due to a misclassification of SDSS images or to a partial obscuration of the nuclear regions.
2. CSOs and MSOs have a high percentage (>80%) of galaxy-type SEDs (G and $G + Q$), implying that their AGN are mostly obscured in the optical and even in the NIR in some cases. Use of mid-IR survey work by the *Spitzer* and *WISE* satellites should find large numbers of CSOs and MSOs by cross-correlation of bright radio and mid-IR sources.
3. The fraction of G-type objects decreases and that of Q-type objects increases with increasing size (CSOs, MSO, LSOs). This suggests that optical obscuration diminishes with increasing radio size and thus with AGN age (Fanti et al. 1995; Begelman 1996). This result also suggests that, while highly obscured radio-loud AGN may exist in abundance at high-z, they are exceptionally difficult to identify and confirm (i.e., obtain redshifts) because the counterparts rapidly become optically invisible with increasing redshift.

3.3.3. Radio SEDs and Optical+NIR SEDs

Table 6 summarizes the number of objects with a particular radio SED type and optical+NIR SED type. Following the discussions in Sections 3.3.1 and 3.3.2, we find that GPS objects are associated with G or G+Q-type objects, while two out of the seven FS objects show Q-type optical-NIR SEDs. Here again we see that the fraction of quasars in FS objects is much lower than in traditionally selected samples. We conclude that there is a good correspondence between radio morphological types, radio SED types, and optical-NIR SED types: CSO-GPS-G, MSO-CSS-G, LSO-SS-G, CJ-FS-Q, where

Table 7
Observing Log

Object	z	z ref	Line(s) Searched	Telescope/Receiver	Date	Line(s) Detected
(1)	(2)	(3)	(4)	(5)	(6)	(7)
J0003−1053[a]	*0.42 ± 0.02	(Yan 2013)	H I	GBT/PF2	28 and 30 Sep 09	···
J0003−1053[a]	1.474 ± 0.001	(Yan 2013)	H I	GMRT	21 Jan 10 and 19 Oct 13	···
J0134+0003	0.879	NED	H I	Arecibo/800 MHz	09 Oct 09	···
J0134+0003	0.879	NED	H I, OH	GBT/PF1 680–920 MHz	07 Feb 13	···
J0751+2716[b]	0.34937 & 3.2	NED	H I	GBT/PF2	08 Oct 09	···
J0805+1614	:0.632 ± 0.002	(Yan 2013)	H I	GBT/PF1 680–920 MHz	10 Feb 13	···
J0805+1614	:0.632 ± 0.002	(Yan 2013)	OH	GBT/PF2	08 Jun 09	···
J0805+1614	:0.632 ± 0.002	(Yan 2013)	OH	GBT/PF2	13 Oct 09	···
J0824+5413	0.6385 ± 0.0003	(Yan 2013)	H I	GBT/PF1 680–920 MHz	21 May 09	···
J0839+2403	*0.88 ± 0.19		H I	GBT/PF1 680–920 MHz	22 May 09	···
J0839+2403	*0.88 ± 0.19	···	H I	Arecibo/800 MHz	14 Mar 11	···
J0839+2403	*0.88 ± 0.19	···	H I	Arecibo/800 MHz	15 Mar 11	···
J0901+0304	0.2872 ± 0.0001	(Yan 2013)	H I	GBT/PF2	09 Oct 09	H I
J0901+0304	0.2872 ± 0.0001	(Yan 2013)	H I	VLA	28 Dec 09	H I
J0901+0304	0.2872 ± 0.0001	(Yan 2013)	H I	GMRT	28 Jan 10	H I
J0910+2419	*0.70 ± 0.06	···	H I	GBT/PF1 680–920 MHz	21 May 09	···
J0920+2714	0.2064 ± 0.0002	(Yan 2013)	H I	GBT/L-band	10 Sep 06	H I
J0939+0304	*0.47 ± 0.03	···	H I	GBT/PF2	08 Jun 09	···
J0951+1154	*0.62 ± 0.26	···	H I	GBT/PF1 680–920 MHz	01 Jul 09	···
J1008+2401	*0.88 ± 0.22	···	H I	GBT/PF1 680–920 MHz	01 Jul 09	···
J1023+0424	*0.63 ± 0.15	···	H I	GBT/PF1 680–920 MHz	22 May 09	···
J1023+0424	*0.63 ± 0.15	···	H I	Arecibo/800 MHz	15 Mar 11	···
J1033+3935	1.095 ± 0.002	NED	H I	GBT/PF1 510–690 MHz	03 Nov 09	···
J1043+0537	*0.87 ± 0.29	···	H I	GBT/PF1 680–920 MHz	22 May 09	···
J1043+0537	*0.87 ± 0.29	···	H I	Arecibo/800 MHz	14 Mar 11	···
J1129+5638	0.892 ± 0.002	Gemini	H I	GBT/PF1 680–920 MHz	15 Apr 12	H I
J1238+0845	*0.83 ± 0.14	···	H I	GBT/PF1 680–920 MHz	22 May 09	···
J1238+0845	*0.83 ± 0.14	···	H I	Arecibo/800 MHz	14 Mar 11	···
J1238+0845	*0.83 ± 0.14	···	H I	Arecibo/800 MHz	15 Mar 11	···
J1315+0222	*0.55 ± 0.48	···	H I	GBT/PF1 680–920 MHz	01 Jul 09	···
J1357+0046	*1.00 ± 0.17	···	H I	GBT/PF1 680–920 MHz	22 May 09	H I
J1357+0046	*1.00 ± 0.17	···	H I	GBT/PF1 680–920 MHz	01 Jul 09	H I
J1357+0046	*1.00 ± 0.17	···	OH	GBT/PF2	08 Jun 09	···
J1410+4850	0.592 ± 0.001	Gemini	H I	GBT/PF1 680–920 MHz	08 Feb 13	···
J1414+4554	:0.186 ± 0.002	NED	H I	GBT/L-band	12 Mar 09	···
J1414+4554	:0.186 ± 0.002	NED	H I	GMRT/L-band	29 Jan 10	···
J1421−0246	*0.53 ± 0.02	···	H I	GBT/PF2	05 Jun 09	···
J1424+1852	*0.53 ± 0.02	···	H I	GBT/PF1 680–920 MHz	22 May 09	···
J1504+5438	0.62244 ± 0.00013	SDSS	H I	GBT/PF1 680–920 MHz	21 May 09	···
J1604+6050	0.559 ± 0.001	Gemini	H I	GBT/PF1 680–920 MHz	08 Feb 13	H I:
J1616+2647	0.755 ± 0.001	Gemini	H I	GBT/PF1 680–920 MHz	15 Apr 12	H I
J2203−0021	0.729 ± 0.001	(Yan 2013)	H I	Arecibo/800 MHz	09 Oct 09	···
J2203−0021	0.729 ± 0.001	(Yan 2013)	OH	GBT/PF2	01 Oct 09	···

Notes. Columns list: (1) Object name in IAU convention; (2) the redshift used for the line search, either (a) a spectroscopic redshift obtained by us or found in the literature, or (b) a photometric redshift from SDSS DR6 ("*"). Uncertain redshifts are indicated by a colon; (3) redshift reference ("Gemini" indicates a new redshift obtained by us at Gemini North and reported here for first time); (4) line(s) searched; (5) telescope/receiver used; (6) observing date; (7) line(s) detected.
[a] J0003−1053 was observed at the foreground photometric redshift at the GBT (first line entry above) and at the background spectroscopic redshift at GMRT (second line entry).
[b] J0715+2716 was observed only at its foreground photometric redshft at GBT, not at its $z = 3.2$ intrinsic AGN redshift.

"CSS" stands for CSS sources, a name that combines morphological and SED features (Fanti et al. 1990). Although the radio SED types require fewer observations to classify, they do not specify a radio morphology (e.g., CSOs can be FS, GPS, or SS objects depending on the source's turnover frequency). Therefore, high-resolution radio images are crucial to reveal the nature of these objects.

Among the nine USS objects, seven have quasar-type SEDs; additionally, they are all MSOs or LSOs. Redshifts for three USS objects are available, all at high-z = 1.8–2.9. For comparison, the other two objects with $z \geqslant 1.8$ are the gravitational lens system J0751+2716 and an FS core-jet object J1625+4134. In objects with $\alpha_l < -0.9$, only J0920+2714 has a G-type SED, and we show in Section 3.4.1 that this is an intervening absorption system with a foreground galaxy at $z = 0.206$ that is much brighter than the AGN host galaxy in the optical+NIR. The radio source host remains undetected on our deepest optical ($r > 23$) and NIR ($K_s > 19$)

images (see Paper I). Our findings in this sample are consistent with many of the USS objects at high-z (e.g., Roettgering et al. 1994).

3.4. Individual Sources of Interest

3.4.1. Positional Offsets

In Paper I, we detected an NIR counterpart for every optical counterpart (i.e., the offset between the NIR and optical centroid positions is within 5σ of their combined uncertainties). The measurement errors of the optical/NIR objects are of order $\sim 0\farcs1$–$0\farcs2$ and their observed angular sizes are $\lesssim 2''$, except for a few larger objects ($\sim 5''$). However, the diffuse, asymmetrical morphology of some of these galaxies makes their centroid determination more uncertain than the measurement errors. In addition, the resolution of the FIRST survey is $\sim 5''$, which is insufficient to determine a precise offset between the optical/NIR and radio positions. Using our new high-resolution radio images, we scrutinized each object's radio core position to see whether there is a significant offset that might indicate unusual systems, such as intervening or interacting galaxies. In Figure 5 in the Appendix, the optical and NIR centroids are located on the VLA and VLBA maps. These positions are seen most easily on the 4.9 GHz maps as blue (optical) and red (NIR) crosses. When the centroid positions are inside the green boxes marking the VLBA map field of view, the centroids are also located on the 1.4 GHz VLBA maps, although typically the positional errors are much larger than the component sizes, making firm identifications of the VLBI core difficult with current data in most cases.

We discuss here all sources with significant radio/optical-NIR positional offsets. The radio and NIR images and component solutions for all of these sources can be found in the Appendix.

J0003−1053 has four components in its 4.9 GHz and 8.5 GHz images. Its NIR centroid position is coincident with the "C" component, which has an inverted spectral index. All other components have steep spectral indices $\alpha < -0.5$. However, the optical centroid position is close to the "B" component. A redshift of 1.474 ± 0.001 is obtained from emission lines in the NIR (see Paper I), but the photometric redshift given by SDSS DR8 is 0.57 ± 0.12. The optical-NIR SED is very red with $(r - K_s) = 5.5 \pm 0.3$, redder than typical elliptical galaxies, and classified as Q + abs. We suggest that the object at $z = 1.474$ is heavily obscured either intrinsically or, more likely, by the foreground galaxy that may or may not have associated radio emission. The co-linearity of components B, C, and D strongly favors component B being a part of the background radio source at $z = 1.474$, not emission from the foreground galaxy. Either situation makes this source favorable for the detection of absorption lines at $z = 0.5$–0.7.

J0807+5327 has a double-lobe radio structure. However, the entire radio structure is to the south of the optical and NIR centroid positions by $\sim 1\farcs5$, which makes it possible that the radio source is not associated with the optical+NIR object we detect. If this is a core-jet object with a core in the "A" component, the core is still $\sim 0\farcs5$ away from the NIR centroid position. The VLBA detected source appears morphologically similar to a hotspot in a single radio lobe, identified as component "A" in Figure 14 in the Appendix. However, there is no bright source to the NE of this position, which would be the second associated lobe of this source. Regardless of the overall nature of the source, the coincidence on the sky of a diffuse galaxy and a ∼100 mJy compact radio source is favorable for the detection of absorption lines.

J0917+4725 shows an extended structure in its 4.9 GHz and 8.5 GHz images, and the radio center is $1\farcs3$ away from the NIR center. We overlay a larger field of view FIRST map with an r-band SDSS image in Figure 1. The maps in Figure 14 in the Appendix are at higher resolution than the FIRST image and show a morphology consistent with being a single radio lobe, with its hotspot detected by the VLBA. A second radio lobe is seen in the northeast $\sim 40''$ away, making it unlikely that the NIR object shown in Figure 1 is the host galaxy. It is unknown which is the optical counterpart to the radio source. Absorption lines are unlikely to be detected due to the positional offset between the compact source seen with VLBA and the NIR galaxy, even if the optical+NIR object is in the foreground of the radio source.

J0920+2714 is an LSO with the brighter lobe overlapping with but not centered on an elliptical galaxy at $z = 0.209$ ($1\farcs5$ away from optical center). An H I absorption line has been detected at the redshift of the elliptical galaxy (see Section 4). We conclude that the optical–NIR galaxy is not the counterpart to the radio source; the radio source counterpart is too faint and/or too obscured to be seen on our deepest optical and NIR images. The USS for this radio source and the absence of a strong core suggest that this radio source is likely at high-z.

J1341+1032 is an MSO that is offset from its optical+NIR center, similar to J0807+5327 and J0920+2714. This makes it a good candidate to detect absorption lines at the redshift of the offset foreground galaxy, which is very diffuse and has an SDSS $z_{\rm phot} \approx 0.4$. A possible detection of the optical/NIR counterpart to the radio source can be seen between the 4.9 GHz map components A and B in the NIR image overlay in Figure 14 in the Appendix.

3.4.2. Gravitational Lens Candidates

If well-aligned, the foreground galaxy in an intervening system can substantially deflect the light from the background source and form a gravitationally lensed arc. In this case, the optical/NIR object we identify may be a foreground galaxy with a positional offset from the radio source core. Therefore, an arc-like structure to the radio source can help us discover candidates for lensing systems. Three objects show arc-like features in the sample, including J0751+2716, a previously known gravitational lens system (Lehar et al. 1997), which will not be discussed further here.

J1559+4349 has a NIR redshift of 1.232 ± 0.001 (Paper I) and an optical photometric redshift of 0.42 ± 0.09 according to SDSS DR8 (Eisenstein et al. 2011). We classify its optical +NIR SED as Q + abs because it is bluer than an Sc-type galaxy. Figure 2 shows that the K-band center (red cross) is close to the radio core position. If the radio structure is part of an Einstein ring with radius $0\farcs64$, the center of the ring is close to the r-band center (blue cross). Therefore, we suggest that the foreground lens dominates the optical light, while the background AGN host at $z = 1.232$ is dominant in the NIR. J1559 +4349 has two components in its VLA-A 4.9 GHz and 8.5 GHz images with spectral indices −1.0 and −1.2, respectively. However, extrapolated to 1.4 GHz, only ∼50% of the total flux density of "A" and ∼20% of "B" are detected in the VLBA image.

Table 8
H I Detections

Object	Comp. ID	Resolution (kHz)	rms (mJy)	Center (MHz)	FWHM (km s^{-1})	τ_p	z	$\int \tau dv$ (km s^{-1})	$N_{\rm H\,I}$ (10^{20} cm^{-2})
(1)	(2)	(3)	(4)	(5)	(6)	(7)	(8)	(9)	(10)
J0901+0304[a]	A	24	1.5	1102.277 (2)	46 (2)	−0.0775 (23)	0.288611 (3)	3.79 ± 0.17	6.82 ± 0.31
	B								
	Int[b]							3.82 ± 0.10	6.88 ± 0.18
J0901+0304[c]	A	65	2.0	1102.267 (8)	54 (5)	−0.0560 (47)	0.288623 (10)	4.70 ± 0.22	8.46 ± 0.39
	B			1103.486 (15)	92 (10)	−0.0387 (36)	0.287199 (18)	5.52 ± 0.31	9.94 ± 0.56
	Int							10.22 ± 0.38	18.40 ± 0.68
J0901+0304[d]	A	48	2.0	1102.341 (6)	34 (4)	−0.0608 (62)	0.288536 (7)	3.04 ± 0.17	5.47 ± 0.30
	B			1103.625 (13)	68 (9)	−0.0401 (44)	0.287036 (15)	4.03 ± 0.22	7.26 ± 0.39
	Int							7.07 ± 0.27	12.73 ± 0.49
J0920+2714	A	24	1.8	1177.131 (2)	13 (1)	−0.0819 (107)	0.206668 (2)	1.10 ± 0.19	1.97 ± 0.34
	B	24	1.8	1177.072 (13)	33 (5)	−0.0405 (47)	0.206728 (13)	1.42 ± 0.26	2.56 ± 0.47
	Int							2.61 ± 0.12	4.70 ± 0.21
J1129+5638	A	12	5.0	750.764 (15)	104 (12)	−0.0276 (68)	0.891947 (38)	3.07 ± 0.83	5.52 ± 1.49
	B	12	5.0	751.033 (193)	170 (109)	−0.0063 (24)	0.891270 (487)	1.13 ± 0.85	2.04 ± 1.53
	Gfit[e]	12	5.0	750.788 (6)	127 (6)	−0.0285 (11)	0.891886 (15)	3.85 ± 0.22	6.93 ± 0.40
	Int							4.16 ± 0.14	7.49 ± 0.24
J1357+0046[f]	A	24	2.8	790.764 (5)	80 (5)	−0.0130 (6)	0.796246 (11)	1.12 ± 0.08	2.01 ± 0.15
	B	24	2.8	790.396 (7)	71 (6)	−0.0088 (7)	0.797081 (16)	0.66 ± 0.08	1.19 ± 0.14
	Int							1.82 ± 0.04	3.28 ± 0.07
J1357+0046[g]	A	24	3.7	790.767 (5)	90 (4)	−0.0140 (6)	0.796239 (10)	1.34 ± 0.08	2.41 ± 0.15
	B	24	3.7	790.410 (8)	59 (7)	−0.0068 (7)	0.797049 (18)	0.42 ± 0.07	0.76 ± 0.12
	Int							1.74 ± 0.05	3.14 ± 0.09
J1604+6050	Gfit	6	3.0	911.025 (2)	8 (2)	−0.0142 (25)	0.559130 (4)	0.12 ± 0.03	0.22 ± 0.06
	Int							0.14 ± 0.02	0.25 ± 0.04
J1616+2647	Gfit	49	3.4	809.133 (34)	447 (30)	−0.0084 (5)	0.755467 (73)	3.98 ± 0.35	7.16 ± 0.63
	Int							4.00 ± 0.16	7.21 ± 0.28

Notes. Columns list: (1) object name in IAU convention; (2) ID of the absorbing component, where "Gfit" means there is only one component and "Int" means an integrated value for all components; (3) spectral resolution of the spectrum; (4) rms measured from continuum-subtracted background; (5)–(8) Gaussian fit results of the line center in frequency, FWHM in rest-frame velocity, peak of optical depth, and redshift of line center; (9) integrated optical depth $\int \tau dv$ either from a Gaussian fit or in the case of "Int," directly integrated from the spectrum non-parametrically; (10) the column density of the absorbing component assuming an 100% covering factor and a spin temperature of 100 K.

[a] GBT observation.
[b] "A" component only.
[c] GMRT observation.
[d] VLA observation.
[e] Gaussian fit of single compoent.
[f] GBT observation on 2009 May 22.
[g] GBT observation on 2009 July 01.

J1147+4818 is classified as a CJ object based on its VLA-A images. No emission from component "B" (as seen on the VLA-A 4.9 and 8.5 GHz maps in the Appendix) is detected in the 1.4 GHz VLBA image. We show in Figure 3 that the arc-like string of VLBA components lies on a circle with radius 0.″20. The optical and NIR centroid positions are coincident and both are in the vicinity of the arc, although their uncertainties are large. J1147+4818 is a *Q*-type object but DR8 gives a photometric redshift of $z = 0.17 \pm 0.05$ by assuming it is a galaxy. Compared to J1559+4349, J1147+4818 is a less-likely gravitational-arc system due to the absence of evidence for two distinct optical and NIR objects, as in the previous case. In addition, radio sources often show modest intrinsic curvature of core-jet components as seen in Figure 3. We conclude that while J1559+4349 almost certainly possesses arcuate radio structure due to a foreground galaxy, J1147+4818 is a much less-likely gravitationally lensed background source.

3.4.3. Other Objects of Interest

J0834+1700 is one lobe in a double-lobe structure 25″ apart (see Figure 4), similar to another single-lobe object, J0917+4725. The radio source is so well-aligned with the optical +NIR object that no significant positional offset is present, unlike in the case of J0917+4725. Absorption lines may be detected if the radio source is in the background, although the large amount of extended radio flux makes this a poor candidate for finding intervening absorption.

J1048+3457 is a likely C IV broad-absorption-lines (BAL) QSO at $z = 1.6$ (Willott et al. 2003). Without spectral information for the VLBA components, we cannot distinguish a core-jet structure from a CSO-type structure in this source. The multi-component sub-arcsec scale structure might indicate interactions with a dense ISM at an early stage of its radio activity (Kunert-Bajraszewska & Marecki 2007; Kunert-Bajraszewska et al. 2010).

Table 9
H I Upper Limits

Object	Search Freq. (MHz)	rms (mJy)	$\tau_{3\sigma}$	$N_{\rm H\,I}$ (10^{20} cm^{-2})
J0003−1053[a]	574.13	2.6	<0.010	<0.80
J0134+0003[b]	755.94	11.6	<0.030	<1.8
J0134+0003[c]	755.94	5.4	<0.010	<0.61
J1414+4554[a]	1197.64	1.5	<0.0084	<0.65

Notes. The rms noise and the 3σ optical depth limits are computed at velocity resolutions of 16.3 km s^{-1} (J0003−1053), 10 km s^{-1} (J0134+0003), and 15.6 km s^{-1} (J1414+4554). The $N_{\rm H\,I}$ limits assume a spin temperature of 100 K, a covering factor of unity, and a FWHM of 100 km s^{-1} for the absorption line. These calculations use the rms noise after smoothing the spectra to a velocity resolution of 100 km s^{-1}.
[a] GMRT observation.
[b] AO observation.
[c] GBT observation.

J1527+3312 is unresolved in the 8.5 GHz VLA-A image, but is very extended in the higher-resolution 1.4 GHz VLBA image for which only 25% of the total flux density is accounted. While further observations are needed to detect the diffuse radio emission, this "missing flux" makes J1527 +3312 a poor candidate for detecting H I in absorption.

4. REDSHIFTED H I 21 CM SPECTROSCOPY

In this section we report the results of an incomplete search for redshifted H I 21 cm and OH absorption at sub-GHz frequencies. Due to the presence of substantial, site-specific RFI, the most successful portion of our attempted radio spectroscopy is for those six sources where accurate spectroscopic redshifts were available and where those redshifts move the H I 21 cm absorption to a spectral region that is relatively clear of RFI. Seven sources with good spectroscopic redshifts have significant RFI at the frequency of the redshifted H I 21 cm, precluding a sensitive search for absorption. Four of the six sources that have usable data at their spectroscopic redshifts have clear H I detections with a fifth showing a tentative detection. Optical spectroscopy supporting these observations was presented in Paper I although, since that publication, four new spectroscopic redshifts were obtained at the *Gemini North Observatory* using the multi-object spectrograph (GMOS) in a single-object mode. Based on the detection and measurement of strong, narrow emission lines in these spectra, these redshifts appear in Table 7 with a reference of "Gemini."

Because we lacked optical and/or NIR spectroscopy for most of the sources in this sample, we attempted radio spectroscopy for 14 additional sources at their photometric redshifts, making only one detection. While these sources were chosen using the same optical/NIR photometric classifications (i.e., pure "G"- and "G+Q" types preferred) and radio continuum observations (i.e., CSOs and GPS preferred) as guides to determine those most likely to have observable H I and molecular absorption, the rather coarse accuracy of the photo-zs (±0.1–0.2, which translates into a frequency uncertainty of ±35–70 MHz at $z = 1$) made these searches mostly unsuccessful. Given the strength and ubiquity of the RFI over these very broad observing bands, it is not possible even to establish viable detection limits for the 14 sources observed with only photometric redshifts.

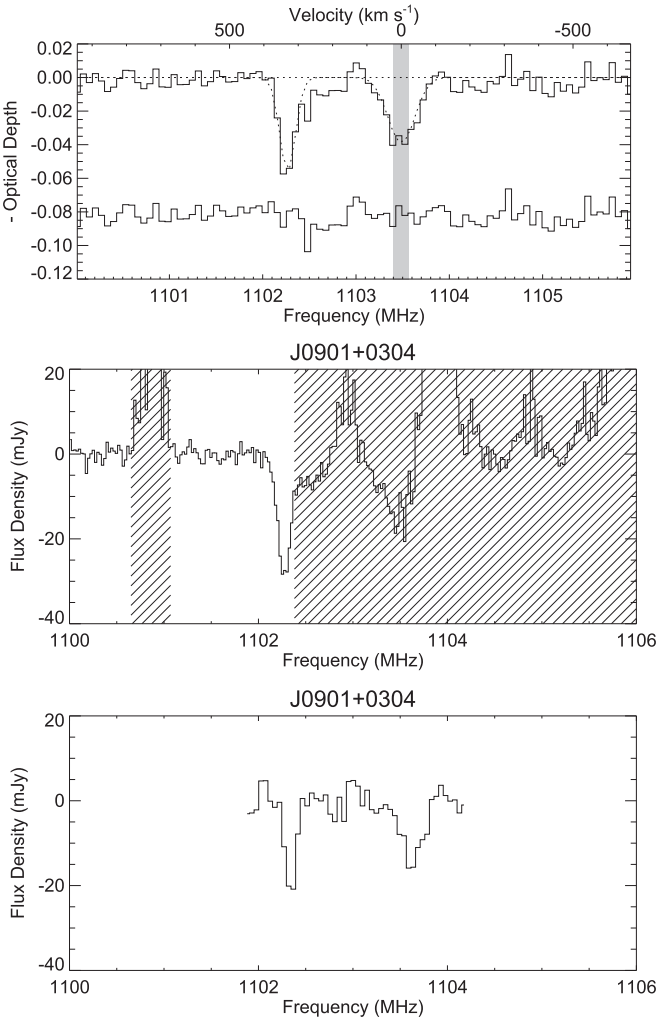

Figure 5. The H I 21 cm spectrum in J0901+0304 as observed by GMRT (top), GBT (middle), and VLA (bottom). On the GMRT plot, Gaussian fits to the two absorption components are shown as dotted lines. Residuals are displayed at the bottom of this plot offset in the "y"-coordinate for clarity. Zero velocity is set to the redshift of the optical galaxy at $z = 0.2872 \pm 0.0001$, with redshift uncertainty shown in gray shade. The hatched regions in the GBT spectrum are regions contaminated by RFI.

4.1. Observations and Data Reduction

Observations were carried out at several radio telescopes, each using specific receivers and observing modes to access the location in frequency of the redshifted H I 21 cm line. The observing log shown in Table 7 indicates the telescope/receiver combinations used for these various observations.

At the Robert C. Byrd Green Bank Telescope (GBT) of NRAO, observations were conducted with the two prime focus receivers—PF1 (~510–690 or ~680–920 MHz) and PF2 (~901–1230 MHz)—at the appropriate frequency bands for the redshifted H I hyper-fine transition. The spectrometer was set to the narrow-bandwidth, high-resolution mode with dual linear polarizations and multiple spectral windows taking spectra simultaneously. Usually four spectral windows were used, with each having a 50 MHz bandwidth and 4096 channels. Position-switched scans were performed on the target and sky reference positions with 5 minute durations and 2 s integration time. For a typical object of 0.8 Jy at 900 MHz, five position-switched pairs were carried out to

detect a $\tau = 0.01$ absorption line at 5σ significance. The total observing time for each target ranged from ~20 minutes to ~2 hr due to the large flux density range of our targets. Flux densities are calibrated using the noise diode calibrator, which was turned on half of the time for each integration. The uncertainty of this "standard" flux calibration is ±10%. Nonetheless, only relative fluxes (optical depths) are of interest to this work. The data were reduced using GBTIDL, which is an interactive package for the reduction and analysis of spectral-line data taken with GBT. Each integration and polarization was calibrated separately and then averaged together. However, the RFI, while either intermittent or persistent, is always strong and variable. Therefore, a median spectrum of all integrations for each polarization is calculated to eliminate sporadic RFIs not present in most integrations. The noise of a median spectrum is $\pi/2$ larger than that of a mean spectrum if the frequency range is RFI-free or only slightly contaminated. If a possible absorption line is identified, each integration is carefully inspected to flag those with the strongest RFI. A final spectrum is obtained by averaging all remaining integrations.

At the GBT, 12 objects were searched at their spectroscopic redshift, which led to five detections (the absorption in J0901+0304 was contaminated by RFI, but confirmed later by VLA and Giant Metrewave Radio Telescope (GMRT) observations). Additionally, one tentative detection (J1357+0046) was made. Five spectra are in RFI-rich regions, precluding a sensitive search at $z_{\rm spec}$. A 3σ upper limit of $\tau < 0.01$ ($N_{\rm H\,I} < 2.0 \times 10^{20}\,{\rm cm}^{-2}$) was obtained for J0134+0003 from an observation free of RFI at the spectroscopic redshift of the source. These GBT observations targeted all sources in this sample with spectroscopic redshifts (see Table 1 in Paper I) that placed the redshifted H I 21 cm line in an observable band that is relatively free of intense RFI at GBT. Since the publication of Paper I, three new spectroscopic redshifts were obtained for sources in this program (see below). The targets observed at GBT were mostly those with either point-like or CSO radio continuum emission, pure galaxy SEDs ("G-type"; see Paper I), and GPS SEDs in the radio. The detection rate for "G-type"/GPS/CSO type sources is at least 70% (i.e., five out of seven), with only one firm non-detection (J0134+0003) completely clear of RFI at its spectroscopic redshift. Therefore, the actual detection rate in this class of source could be even higher.

Additionally, 13 objects were searched at GBT with wide bandwidth for 21 cm absorption lines at their photometric redshifts. These observations led to only one detection in the CSO: "G+Q"-type source J1357+0046. Interestingly, the detected H I absorption lines were found at $z = 0.7971$, 0.7962, which is quite far away from the SDSS $z_{\rm phot} = 0.57 \pm 0.17$ for the optical host galaxy. While the selection criteria for observing these sources were similar to the group with spectroscopic redshifts, a much smaller detection rate was obtained: $1/13 = 8\%$ for sources with $z_{\rm phot}$ only versus $5/12 = 42\%$ for sources with accurate $z_{\rm spec}$ values. And since only seven of the $z_{\rm spec}$ sources were in regions clear of RFI, the detection rate is actually $5/7 = 71\%$ for our sample (i.e., conservatively including the tentative detection among the non-detections). We infer that redshifted H I likely is present in most of the 13 $z_{\rm phot}$ sources we observed, but its presence was hidden from detection by RFI.

At the Arecibo Observatory (AO), six objects were observed with the 800 MHz receiver (~700–800 MHz) in dual polarization mode. J0134+0003 was searched for H I at its spectroscopic redshift, but an upper limit was obtained with less sensitivity compared to our GBT observations. Additionally, four objects were searched at their photometric redshifts. These four objects were also searched at GBT using the 680–920 MHz receiver. No detection or RFI-clear upper limits were obtained.

At the AO, the Mock Spectrometer contains 14 independent boxes that were configured to have 8192 channels and a bandwidth of 12 MHz with some overlap to cover the entire 100 MHz frequency range of the receiver. Double position-switched scans were performed to cancel residual standing waves, which resulted in an observing sequence containing four scans: on-target, off-target, on-reference, and off-reference. A reference source was observed close to each target source in space and time. Each scan was three to five minutes long, and the total observing time was one to two hours for each source. The data were reduced by IDL routines provided by AO. The reference sources are also used as flux calibrators. The AO observations took advantage of a period that was relatively RFI-free just prior to the inception of digital television in Puerto Rico. This observing window has now been closed.

Observations to confirm the GBT detection of the redshifted H I 21 cm H I absorption lines toward J0901+0304 were carried out with the VLA of NRAO on 2009 December 28. The array was in the D-configuration, and the total observing time was 1 hr. These observations used 21 antennas that were converted to the EVLA standards. The data were correlated using the old VLA correlator. The aliasing that was known to affect the lower 0.5 MHz of the bandwidth for EVLA data, which were correlated with the old VLA correlator, was avoided by properly placing the frequencies of the two redshifted H I 21 cm lines within a more restrictive 3.125 MHz band. The calibrator source 3C147 (J0542+4951) was used to set the absolute flux density scale, while the compact source J0925+0019 was used as the complex gain calibrator. The editing, calibration, and imaging of the VLA data were carried out using AIPS. The H I line-free channels were split, and the continuum emission from J0901+0304 was self-calibrated in both phase and amplitude in a succession of iterative cycles. The final phase and amplitude solutions were then applied on the spectral-line data set. The continuum emission was subtracted in the UV-domain, and a Stokes I image cube was made with a synthesized beam width of $97'' \times 67''$ (PA = −26.60).

The GMRT was also used to confirm the GBT detection of H I 21 cm absorption at $z = 0.2872$ in J0901+2734, as well as to search for absorption at $z = 0.186$ toward J1414+4554 (also observed at GBT) and $z = 1.474$ toward J0003–1053 (observed at GBT at $z_{\rm phot} = 0.42$). The initial GMRT observations of the three sources were carried out in 2010 January, using 23–25 working antennas, the GMRT hardware correlator as the backend, two circular polarizations, and the GMRT L-band (J0901+2734 and J1414+4554) and 610-MHz band (J0003–1053) receivers. A bandwidth of 4 MHz was used for all observations, sub-divided into 128 channels (L-band) or 256 channels (610-MHz band); this yielded a velocity resolution of ≈8–8.5 km s^{-1} and a total velocity coverage of ≈1100 km s^{-1} (L-band) and ≈2100 km s^{-1} (610-MHz band). Observations of one of the standard calibrators—3C48, 3C147, or 3C286—were used to calibrate the flux density scale and the

system passband, while nearby compact sources were used for secondary calibration.

The initial GMRT observations of J0003–1053 resulted in a tentative ($\approx 5\sigma$) detection of a weak absorption feature. We re-observed this source with the GMRT in 2013 October, using the GMRT Software Backend, two circular polarizations, and a bandwidth of 4.167 MHz sub-divided into 512 channels, yielding a velocity resolution of $\approx 4.3\,\mathrm{km\,s^{-1}}$ and a velocity coverage of $\approx 2175\,\mathrm{km\,s^{-1}}$. No detection was made.

All GMRT data were analyzed in "classic" AIPS, using standard data editing and calibration procedures to obtain the antenna-based complex gains by interpolating between the values derived from observations of the secondary calibrator. An iterative self-calibration procedure was then used to determine more accurate gains on the target field, and finally, to obtain a continuum image of the field. 3D imaging techniques were used for all sources, sub-dividing the field into 13 (L-band) or 19 (610-MHz band) facets to correct for the non-coplanarity of the GMRT. The target flux densities were measured via a single Gaussian fit to the central region of the final image with the AIPS task JMFIT. We obtained flux densities of (402.39 ± 0.92) mJy for J0901+2734 at ≈ 1104.2 MHz, (385.09 ± 0.78) mJy for J1414+4554 at ≈ 1198.5 MHz, and $\approx (753.0 \pm 1.6)$ mJy for J0003–1053 at ≈ 574.2 MHz. The final continuum image was then subtracted out from the calibrated visibility data using the AIPS task UVSUB, after which a first-order polynomial was fit to the visibility spectra on each interferometer baseline and subtracted. For each source, the residual UV data were then shifted to the barycentric frame and imaged in all channels to obtain the final spectral cube. A cut through this cube at the target location yielded the H I 21 cm spectrum. The root mean square (rms) noise values were measured (in off-line regions of the spectra) to be ≈ 0.0012 per $17.0\,\mathrm{km\,s^{-1}}$ channel (J0901+2734), ≈ 0.0028 per $15.6\,\mathrm{km\,s^{-1}}$ channel (J1414+4554), ≈ 0.0034 per $16.3\,\mathrm{km\,s^{-1}}$ channel (J0003–1053, in 2010), and ≈ 0.0030 per $8.5\,\mathrm{km\,s^{-1}}$ (J0003–1053, in 2013), all in units of optical depth. We note that the weak feature seen in the original spectrum of J0003–1053 was not detected in the deeper spectrum of 2013, and is hence likely to have arisen from low-level RFI.

Details of the H I detections made in this program are shown in Table 8, including the optical depth τ and inferred column density H I assuming a spin temperature $T_s = 100$ K and a 100% fraction of the source covered by the absorbing gas (i.e., $f = 1$). By integrating the optical depth τ over the velocity width (v) of the H I absorption line, we find that the H I column density of the absorbing gas is:

$$N_{\mathrm{H\,I}} = 1.8 \times 10^{18}\,\mathrm{cm^{-2}} \frac{T_s}{f} \int \tau dv. \quad (1)$$

Assuming the same formalism as stated above, our observations made clear non-detections only when: (1) an accurate spectroscopic redshift was available and (2) observations of the redshifted H I 21 cm line frequency were made in an RFI-clear region at the telescope of choice. Sources with only photometric redshift estimates have redshift errors so large that RFI covers a significant percentage of the range of possible redshifts. This renders our observations incapable of determining non-detections without doubt in most cases. So only three non-detections are firm: one at GBT and two at GMRT. Details of the H I non-detections made in this program are shown in Table 9.

In summary, of the fourteen sources with spectroscopic redshifts observed at redshifted H I, only five definite and one tentative detections were made, three observations netted clear non-detections, and five objects were indeterminant due to RFI. Five of our six total H I detections (one detection has only a photometric redshift) are CSOs, while only one (J0134+003) of our three non-detections is a CSO. Thus, the detection rate of CSOs in our sample is very high ($83 \pm 17\%$), although our sample size is quite small.

No OH main or satellite absorption line has been detected in any source in our sample, although only six sources have usable data for this purpose. We obtained good 3σ upper limits for column density of the 1667 MHz main and satellite lines ($N_{\mathrm{OH}} < 1.6$ and $16 \times 10^{14}\,\mathrm{cm^{-2}}$, respectively) in J2203−0021 and limits on one of the two satellite lines in J0751+2716 and J1357+0046 (<20 and $6 \times 10^{14}\,\mathrm{cm^{-2}}$, respectively). These limits assume an excitation temperature of 100 K, a covering factor of 100%, and a rest-frame velocity line-width of $100\,\mathrm{km\,s^{-1}}$. Three other sources (J0805+1614, J1129+5638, and J1357+0046) have the main or satellite lines observable in the band but have RFI present, which precludes an accurate upper limit. Among these six, only J1129+5638 and J1357+0046 have detected redshifted H I 21 cm absorption.

4.2. Individual Sources

4.2.1. J0134+0003

J0134+0003 is a GPS source and a VLBA calibrator that has an optical counterpart with a "G"-type SED best fit by an Sa galaxy template (Mannucci et al. 2001) and spectroscopic $z = 0.8790$. This redshift places the potential H I line in a clear spectral region, but no detection was made either at GBT or AO. At a search frequency of 755.94 MHz, our better GBT observations set a 3σ upper limit of $\tau < 0.010$ and $N_{\mathrm{H\,I}} < 2.0 \times 10^{20}\,\mathrm{cm^{-2}}$ (assuming a $T_s = 100$ K and a 100% covering factor; this limit is less than all of our definite H I detections in the same sample. Evidently, not all compact/GPS/"G"-type sources have detectable H I absorption. Curran et al. (2006) observed this source for H I absorption at Westerbork and also reported a non-detection, although the predicted redshifted 21 cm location was at the edge of intense RFI at that site.

4.2.2. J0901+0304

See Figure 5 for the 21 cm spectra of J0901+0304. We first observed this object using the GBT and found two tentative absorption features. One feature is in a small RFI-free window, while the other is badly contaminated by RFI at Green Bank. We later confirmed both features using the VLA and GMRT where the RFI was not as difficult an issue.

J0901+0304 has a pure Sc galaxy ("G"-type) optical+NIR SED (based on template SEDs from Mannucci et al. 2001) and its optical and NIR images suggest that it may be an interacting system with some diffuse structure extending to the NE of the main galaxy. The optical spectrum obtained by us at the APO 3.5 m telescope includes moderate strength narrow emission lines whose line ratios suggest a LINER or weak Seyfert ionization source (Kewley et al. 2006). J0901+0304 is a GPS source that is not resolved in our VLBA map with a resolution of ~10 mas at 1.4 GHz, which means it could either be a very

small-scale CSO or a core-jet object. The GPS SED suggests that this source is likely a very small CSO.

Two H I absorption lines are detected, one coincident with the optical redshift of $z = 0.2872 \pm 0.0001$, the other redshifted by a velocity of 328 km s^{-1}. Since the broad line has a velocity consistent with the nucleus, we identify this absorption as disk gas, which leaves the narrow component as a likely infalling high-velocity cloud (HVC). This broad-narrow absorption-line pairing is quite similar to the H I 21 cm absorption lines found by Keeney et al. (2011) at low redshift ($z = 0.018$) in PKS 1327−206. In that case the broad, shallow H I absorber is coincident in velocity with the emission-line H II region gas in a spiral arm in the interacting galaxy ESO 1327−2041 and the narrower H I absorption is HVC gas at a velocity of $\Delta v \approx 250$ km s^{-1} with respect to the disk. The low-z of ESO 1327−2041 allowed a definitive determination of which H I absorber is disk gas and which is an HVC. With more examples of broad and narrow H I absorption, we may be able to use the line widths as indicators for where in the galaxy the absorbing clouds are located. However, similar, very broad H I absorption has also been seen to originate from a circumnuclear disk as in 4C 31.04 (Mirabel 1990) and 3C 190 (Ishwara-Chandra et al. 2003).

There is also a very broad absorption blueward of the narrow absorption line in these spectra, which is almost certainly real. It is a cumulative 10σ depression below the continuum in the GMRT spectrum (see Figure 5, top spectrum) with a velocity width of ∼140 km s^{-1}. A similar feature is seen in the GBT spectrum, but it is in a frequency region that is possibly affected by RFI. While this broad absorption is not obviously seen in the VLA spectrum, the continuum level to lower frequencies is not well-defined and so may be present in those data as well. Even though the VLA receivers have lower system temperatures than at the GMRT, the GMRT has ∼25% more aperture (29 antennas to only 21 VLA antennas working for our observation). Because these two differences largely cancel, the >4 times longer on-source integration time at GMRT makes this observation 2–3 times more sensitive. We conclude that the broad absorption is real and is most easily visible as the excess absorption below the dotted line-fit in the GMRT spectrum. Given its redshift relative to the disk absorption and to the emission-line redshift for the nucleus, this feature also appears to be infalling gas.

4.2.3. J0920+2714

See Figure 6 for the 21 cm spectrum from the GBT where we observed J0920+2714 in 2006 through an exploratory program. We later obtained an optical redshift in 2009 and found that the broad 21 cm absorption feature is slightly redshifted ($\Delta v \approx 65$ km s^{-1}) with respect to the galaxy nucleus.

This is an "intervening" H I system in which a double-lobe, steep-spectrum radio source is in the background (unknown redshift) and is well-offset on the sky from the center of an S0 galaxy at $z = 0.2064 \pm 0.0002$ in the foreground. The S0 classification is based both upon a visual inspection of the SDSS and APO 3.5 m NIR images and the optical+NIR SED, which is matched quite well by an S0 template from Mannucci et al. (2001). An APO/DIS spectrum shows absorption lines from starlight and a weak Hα emission line. The clear positional offset between the radio source and the optical/NIR galaxy is described in Section 3.4.1 and shown explicitly in the radio/NIR image overlay in the Appendix.

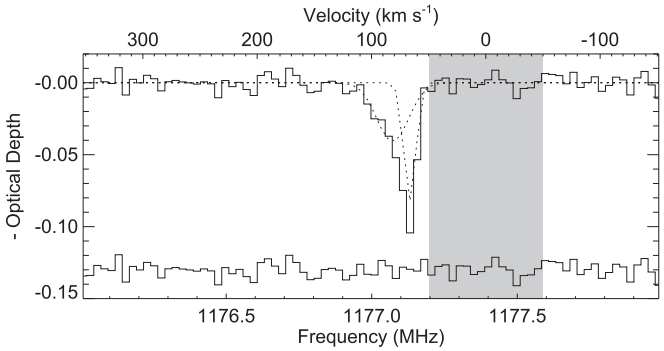

Figure 6. The H I 21 cm spectrum in J0920+2714 as observed by the GBT. We fit the absorption feature with two Gaussian components shown as dotted lines. The narrow component is not resolved (FWHM ≈2 spectral channels). Residuals between the data and the models are displayed with an offset in "y" for clarity. Zero velocity is set to the redshift of the optical galaxy, with the uncertainty in the galaxy velocity shown in gray.

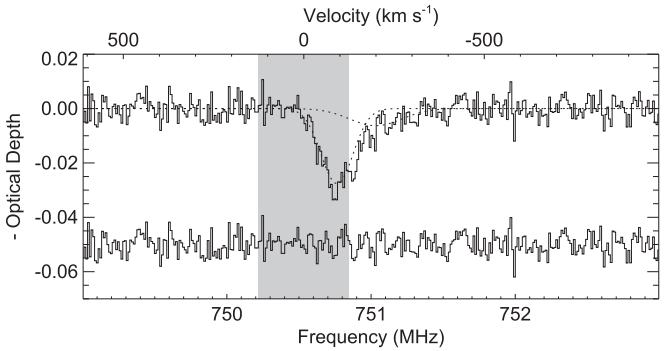

Figure 7. The H I 21 cm spectrum in J1129+5638 as observed by the GBT. Although an asymmetry is present in the absorption line, the shallower component is not well detected (<2σ for a two-component Gaussian fit). We also fit the feature with a single component, which gives a slightly larger χ^2. Gaussian fits to the two absorption components are shown as dotted lines. Residuals are displayed with an offset in "y" for clarity. Zero velocity is set to the redshift of the optical galaxy, with 1σ velocity uncertainty shown in gray.

We fit two Gaussians (dotted lines) to the asymmetric H I absorption feature shown in Figure 6. The deep narrow component is not resolved in velocity and the shallower component has a FWHM of 33 km s^{-1}. Both are redshifted with respect to the systemic galaxy redshift by 66 and 81 km s^{-1}, respectively. However, the rotation curve of the S0 galaxy is redshifted toward the southwest where the strongest radio source component lies. Therefore, at least one of these absorptions is consistent with being normal disk gas in the S0.

4.2.4. J1129+5638

See Figure 7 for the redshifted H I 21 cm spectrum of J1129+5638 taken at the GBT. It is a steep-spectrum source, which is a CSO candidate according to our VLBA observations (see the radio images in the Appendix). Its optical/NIR SED is best fit by a pure "G"-type SED with an Sc-type spiral galaxy template, and at ground-based resolution the optical/NIR morphology is amorphous (see Appendix) with a blue extension to the south that may be a companion galaxy. We recently used Gemini/GMOS to obtain a redshift of

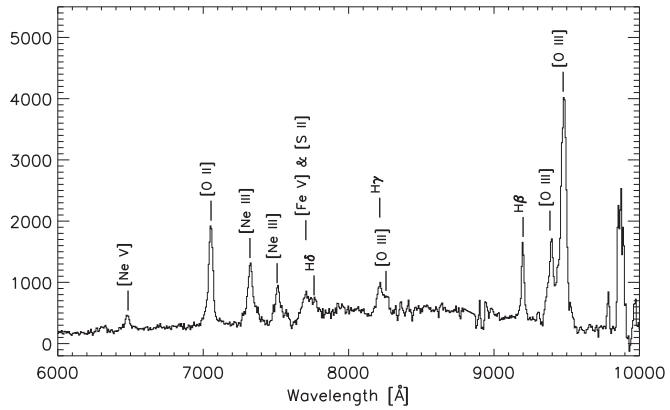

Figure 8. The Gemini/GMOS spectrum of J1129+5638 in counts vs. wavelength (i.e., no flux calibration applied). Unidentified spikes are residual cosmic rays and sky lines. This spectrum is typical for a high-ionization, narrow-line radio galaxy. The apparent emission line at ∼9900 Å is spurious.

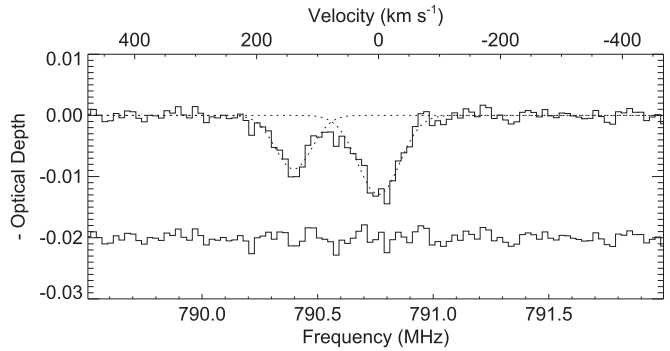

Figure 9. The H I 21 cm spectrum for J1357+0046 as observed by the GBT. J1357+0046 does not have a spectroscopic redshift in the optical. Gaussian fits to the two absorption components are shown in dotted lines. Residuals are displayed with an offset in "y" for clarity. The zero velocity is set to the center of the low-redshift H I component ($z = 0.7962$) because only a photometric redshift is available for this source.

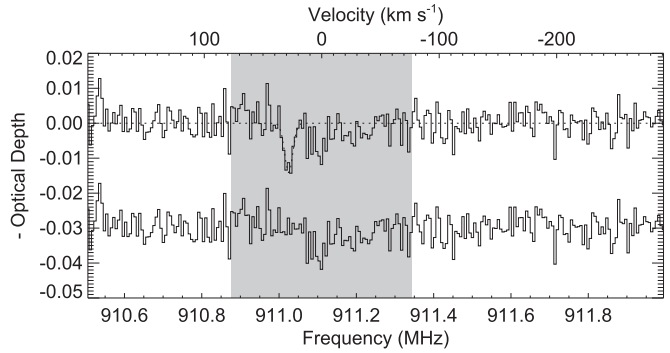

Figure 10. The H I 21 cm spectrum in J1604+6050 as observed by the GBT. There is a tentative absorption line at 911.025 MHz. A Gaussian fit to the absorption component is shown in dotted lines and is almost unresolved by these observations. Residuals are displayed with an offset in "y" for clarity. Zero velocity is set to the redshift of the optical galaxy determined from emission lines with the 1σ redshift uncertainty shown in gray. The apparent absorption at ∼911.03 MHz is an instrumental artifact.

0.8925 ± 0.0008 from strong narrow emission lines (see Figure 8). The presence of the high-ionization [Ne V] line classifies this source as a narrow-line radio galaxy.

The 21 cm absorption is quite broad (FWHM $= 318\,\mathrm{km\,s^{-1}}$ if fit by a single Gaussian profile) at a redshift consistent with

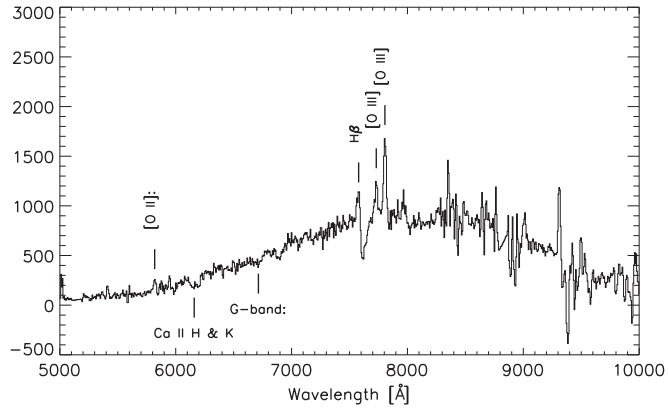

Figure 11. The GMOS spectrum of J1604+6050 displayed as counts vs. wavelength (i.e., no flux calibration). Unidentified spikes are residual cosmic rays and sky lines. The atmospheric oxygen B- and A-bands are visible in absorption. The redshift of $z = 0.5990 \pm 0.0004$ was obtained using just the emission lines.

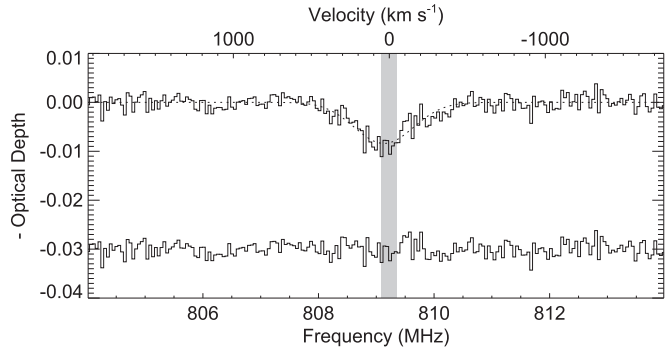

Figure 12. The H I 21 cm spectrum in J1616+2647 as observed by the GBT. A Gaussian fit to the absorption component is shown in dotted lines and has FWHM $= 447\,\mathrm{km\,s^{-1}}$. Residuals are displayed with an offset in "y" for clarity. Zero velocity is set to the redshift of the optical galaxy with 1σ redshift uncertainty shown in gray.

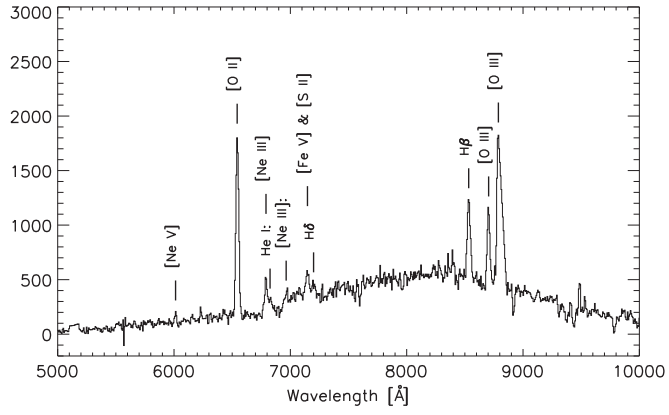

Figure 13. The Gemini/GMOS spectrum of J1616+2647 displayed as counts vs. wavelength (i.e., no flux calibration). Unidentified spikes are residual cosmic rays and sky lines. The redshift of $z = 0.7553 \pm 0.0003$ was determined from the emission lines only.

the redshift of the optical emission lines to within rather broad errors ($\pm 120\,\mathrm{km\,s^{-1}}$). Thus, this detection is consistent either with normal disk gas or outflowing material. However, the CSO-type radio morphology is not consistent with an outflow

in our direction. Therefore, we interpret this detection as being disk gas in a rather massive galaxy (~4L* including *K*- and evolutionary corrections).

4.2.5. J1357+0046

See Figure 9 for the redshifted 21 cm GBT spectrum for this source. This is the only successful detection made in our program without the benefit of an optical/NIR spectroscopic redshift, and was only made because the GBT PF-1 receiver has a very broad bandwidth since the H I detection redshift (z = 0.7971, 0.7962) is quite different from the $z_{\rm phot}$ = 0.57 of the optical galaxy. This large discrepancy is due almost certainly to the presence of a significant amount of non-thermal continuum in the spectrum, producing a substantial error in the photo-z estimate (i.e., the optical/NIR SED classification is "G+Q"). The SDSS and APO NIR images (see Appendix) are quite compact, but with a significant amount of diffuse emission around what may be a compact core. J1357+0046 shows an obvious CSO VLBA structure (see Appendix).

The two H I lines have a velocity separation of 140 km s^{-1} and FWHMs of 80 and 70 km s^{-1}, so neither absorption is the more obvious candidate for disk gas. Without an accurate spectroscopic redshift, an unambiguous assignment of these absorptions as disk gas, infall, or outflow is not possible.

4.2.6. J1604+6050

See Figure 10 for a tentative detection of a single, narrow 21 cm absorption component at the optical redshift obtained by Gemini-GMOS (Figure 11). The optical redshift of the weak, narrow emission lines is 0.5590 ± 0.0004 and that of the tentative H I absorption line is 0.55913 ± 0.00015 ($\Delta v \approx$ 25 km s^{-1}). The tentative 21 cm detection is an extremely narrow line with an FWHM of only 8 km s^{-1}. J1604+6050 is a CSO candidate in our VLBA map (see Appendix) with an optical+NIR SED best fit by a pure "G"-type SED with an S0-type galaxy template. The rather amorphous optical/NIR galaxy images have centroids that are consistent with the CSO centroid seen with the VLBA. Given the optical/NIR (pure "G"-type) and radio continuum properties (GPS and CSO) of this source, it would not be unusual to find an H I absorption-line detection associated with it. Longer integration times are required to confirm this tentative detection.

4.2.7. J1616+2647

See Figure 12 for the 21 cm GBT spectrum of J1616+2647, which reveals a very broad, symmetric profile at the optical redshift. J1616+2647 is a GPS source that is a CSO candidate according to our VLBA observations (see Appendix). Its optical+NIR SED is best fit by an Sc-type galaxy template (i.e., pure "G"-type). The optical/NIR images reveal a compact structure that is well-centered at the CSO position. This source was observed by Gemini/GMOS to obtain a redshift of 0.7553 ± 0.0003 from very strong, narrow emission lines (Figure 13).

J1616+2647 has one of the broadest H I absorption systems detected so far with an FWHM of 447 km s^{-1}. Four objects have 21 cm absorption lines broader than 400 km s^{-1}, including 3C 84 and PKS 2322−12, both cD galaxies close to the center of galaxy clusters (Sarazin et al. 1995; Inoue et al. 1996). While it would be natural to associate these broad absorptions with outflowing gas, the absorption in J1616+2647 is centered at the systemic redshift and could also be partly or largely disk gas in an extremely massive galaxy. Deep imaging to determine whether a rich cluster is present around this galaxy is needed to test this hypothesis.

5. DISCUSSION AND CONCLUSIONS

We have selected and studied a sample of highly obscured radio-loud AGN with the ultimate goal of discovering new highly redshifted absorption systems at radio frequencies. After demonstrating that most of the objects remain obscured in the NIR in Paper I, we find in this paper that their radio properties are also promising for absorption-line searches. There are 52 objects with a compact component with a size 0.″5, providing a small background source that can be efficiently covered by foreground, absorbing gas that might be present in the host galaxy. We have also identified nine potentially intervening systems and sixteen CSOs or CSO candidates (including two previously identified) in our sample. There are twenty MSOs and eight core-jet objects, which are also good potential targets for absorption-line searches. In fact, only the few (fourteen) LSOs not in intervening systems or without a bright, dominant radio core should be excluded from further searches (see Column 15 of Table 2) as unlikely to possess redshifted H I absorption lines in their low-frequency radio spectrum.

Using VLBA maps, the overall radio spectrum, and the optical/NIR SEDs of these sources, we find a strong correlation between compact radio source structure, a GPS radio spectrum, and a pure galaxy ("G"-type) SED. Reasoning that the absence of a non-thermal AGN spectrum in these CSO radio sources indicates that we are viewing the central AGN through an absorbing screen, we targeted these combined classes of sources (CSO/GPS/pure galaxy optical/NIR SED) in our survey for redshifted H I absorption-line spectroscopy.

Of the six CSO/GPS/"G"-type sources with accurate spectroscopic redshifts, we detected H I absorption lines in five of them at their spectroscopic redshift. This includes one tentative detection and one clear non-detection. Additionally, one absorber at a lower redshift than the AGN was also discovered. Using a different sample, Vermeulen et al. (2003) comes to similar conclusions concerning the high H I absorption detection rate from the CSO/GPS class of sources (~33% detection rate in their sample). Our small sample has a significantly larger detection rate for CSOs than was found by that study. Severe RFI at the frequencies of the redshifted H I 21 cm lines prevented a sensitive search in five other CSO/GPS/"G"-type sources with spectroscopic redshifts. Redshifted H I absorption searches in 13 other sources that had only photometric redshifts were largely frustrated by the presence of strong, ubiquitous RFI throughout the sub-GHz radio spectrum. Only one detection was made from this sample of 13, but the RFI is so strong that we cannot rule out the possiblity that many of these sources actually possess H I absorption that we cannot detect from the ground (or anywhere close to human-made RFI). Clearly, having a spectroscopic redshift in-hand is critical in the search for highly redshifted H I and, eventually, molecular absorption lines.

A higher detection rate of H I absorption in radio-loud galaxies compared to radio-loud quasars, in GPS objects compared to flat-spectrum (FS) objects, and in CSOs compared to core-jet sources is broadly consistent with unified schemes of radio-loud AGN (Urry & Padovani 1995). In their simplest

Table 10
Basic Observing Results

Object	VLA 4.9 GHz					VLA 8.5 GHz					VLBA 1.4 GHz				
	Maj. (″)	Min. (″)	P.A. (°)	rms (mJy/beam)	S_m (mJy/beam)	Maj. (″)	Min. (″)	P.A. (°)	rms (mJy/beam)	S_m (mJy/beam)	Maj. (mas)	Min. (mas)	P.A. (°)	rms (mJy/beam)	S_m (mJy/beam)
J0000−1054	0.60	0.44	−6.3	0.15	34.9	0.35	0.25	174.3	0.11	17.6	…	…	…	…	…
J0003−1053	0.60	0.45	−3.3	0.17	31.1	0.40	0.32	32.7	0.15	22.4	…	…	…	…	…
J0134+0003	0.54	0.44	−22.7	0.57*	541.5*	…	…	…	…	…	…	…	…	…	…
J0249−0759	0.72	0.46	−39.8	0.33*	117.9*	0.44	0.32	−44.6	0.71*	137.7*	…	…	…	…	…
J0736+2954	…	…	…	…	…	…	…	…	…	…	…	…	…	…	…
J0747+4618	…	…	…	…	…	…	…	…	…	…	…	…	…	…	…
J0749+2129	0.81	0.46	39.8	0.14	45.0	0.33	0.27	−19.3	0.23	10.0	…	…	…	…	…
J0751+2716	…	…	…	…	…	…	…	…	…	…	…	…	…	…	…
J0759+5312	0.74	0.48	61.0	0.15	97.5	0.33	0.28	1.5	0.18	50.8	11.93	7.02	1.4	0.34	66.7
J0805+1614	0.61	0.46	64.0	0.19	114.0	0.28	0.23	37.5	0.29	89.5	14.43	8.48	9.3	1.00	97.2
J0807+5327	0.75	0.49	59.5	0.15	81.0	0.33	0.28	1.4	0.12	39.0	61.82	55.91	−33.9	2.74	45.3
J0824+5413	0.75	0.49	58.6	0.15	62.9	0.33	0.28	3.9	0.11	30.1	…	…	…	…	…
J0834+1700	…	…	…	…	…	0.26	0.24	−171.1	0.49	226.7	21.78	14.14	66.6	0.17	65.2
J0839+2403	0.43	0.41	−43.6	0.25	97.5	…	…	…	…	…	…	…	…	…	…
J0843+4215	…	…	…	…	…	…	…	…	…	…	…	…	…	…	…
J0901+0304	0.62	0.42	50.4	0.35	160.5	…	…	…	…	…	14.56	6.21	−1.3	0.30	184.9
J0903+5012	0.63	0.49	52.2	0.20	230.0	0.31	0.27	−13.3	0.07	39.4	…	…	…	…	…
J0905+4128	…	…	…	…	…	…	…	…	…	…	…	…	…	…	…
J0907+0413	0.58	0.47	−41.5	0.25	81.8	…	…	…	…	…	…	…	…	…	…
J0910+2419	0.44	0.41	−59.6	0.19	97.1	…	…	…	…	…	…	…	…	…	…
J0915+1018	0.54	0.40	−9.7	0.21	51.6	…	…	…	…	…	…	…	…	…	…
J0917+4725	0.75	0.48	71.0	0.19	63.0	0.31	0.27	−19.4	0.09	24.4	51.39	48.50	−11.1	0.56	7.5
J0920+1753	0.49	0.43	−87.6	0.29	177.2	…	…	…	…	…	…	…	…	…	…
J0920+2714	0.54	0.44	73.8	0.17	91.7	0.35	0.25	78.3	0.22	42.2	34.52	15.91	46.7	0.25	34.6
J0939+0304	0.68	0.41	−40.5	0.26	198.0	…	…	…	…	…	15.38	6.90	1.2	0.24	160.6
J0945+2640	0.97	0.47	61.2	0.15	162.0	…	…	…	…	…	13.66	10.10	8.2	0.11	64.6
J0951+1154	0.49	0.44	−3.0	0.18	26.3	0.74	0.39	−46.7	0.15	15.9	…	…	…	…	…
J1008+2401	0.47	0.41	−47.5	0.16	58.7	…	…	…	…	…	…	…	…	…	…
J1010+4159	…	…	…	…	…	…	…	…	…	…	…	…	…	…	…
J1019+4408	…	…	…	…	…	…	…	…	…	…	…	…	…	…	…
J1023+0424	0.51	0.42	−24.4	0.21	71.5	0.35	0.25	30.0	0.09	38.6	14.69	6.62	5.6	0.28	43.7
J1033+3935	…	…	…	…	…	…	…	…	…	…	…	…	…	…	…
J1034+1112	0.54	0.46	51.4	0.17	123.7	0.31	0.27	71.7	0.28	53.7	…	…	…	…	…
J1043+0537	0.53	0.44	38.7	0.12	46.7	…	…	…	…	…	…	…	…	…	…
J1045+0455	0.55	0.46	42.3	0.14	52.0	0.49	0.30	56.9	0.20	23.1	…	…	…	…	…
J1048+3457	…	…	…	…	…	…	…	…	…	…	8.12	4.86	−5.9	0.60	73.7
J1120+2327	…	…	…	…	…	…	…	…	…	…	…	…	…	…	…
J1125+1953	0.47	0.43	54.8	0.21	101.9	…	…	…	…	…	15.40	8.37	−13.1	0.20	18.2
J1127+5743	0.53	0.41	2.0	0.21	147.3	0.44	0.26	−33.4	0.20	79.3	24.87	15.68	65.1	0.36	219.9
J1129+5638	0.58	0.44	−2.0	0.28	108.3	0.47	0.26	−35.9	0.18	54.0	9.67	6.78	3.0	0.14	80.5
J1142+0235	0.57	0.41	−1.3	0.23	64.6	0.29	0.25	−175.8	0.46	40.9	…	…	…	…	…
J1147+4818	0.49	0.43	71.3	0.20	93.2	0.54	0.26	73.4	0.33	50.8	12.83	12.19	8.6	0.45	33.3
J1148+1404	0.47	0.44	−44.8	0.25	57.8	0.29	0.25	15.7	0.12	31.4	47.11	28.02	29.3	0.57	11.7
J1202+1207	0.48	0.43	24.3	0.17	130.4	0.29	0.28	70.8	0.10	88.7	13.23	6.76	3.4	0.15	32.3
J1203+4632	0.42	0.41	87.3	0.25	184.2	…	…	…	…	…	…	…	…	…	…
J1207+5407	0.57	0.49	12.6	0.19	71.4	0.41	0.29	109.6	0.33	33.0	…	…	…	…	…
J1215+1730	0.44	0.41	−55.5	0.40	356.1	…	…	…	…	…	…	…	…	…	…
J1228+5348	0.74	0.46	85.9	0.17	47.6	0.56	0.42	−16.1	0.35	30.8	…	…	…	…	…
J1238+0845	0.55	0.45	45.0	0.13	86.6	0.29	0.29	−27.9	0.07	41.6	33.93	15.65	47.5	0.64	30.5
J1300+5029	…	…	…	…	…	…	…	…	…	…	…	…	…	…	…
J1312+1710	0.44	0.42	14.1	0.21	94.3	0.26	0.25	−46.7	0.07	56.3	13.86	7.64	15.5	0.40	36.7
J1315+0222	0.56	0.42	−22.2	0.20	68.6	0.30	0.25	−26.2	0.11	33.9	…	…	…	…	…
J1341+1032	0.61	0.44	68.9	0.16	80.8	0.30	0.28	96.6	0.17	34.5	…	…	…	…	…
J1345+5846	0.69	0.41	73.2	0.15	72.7	0.32	0.29	77.4	0.12	37.1	22.12	13.74	78.2	0.50	20.5
J1347+1217	…	…	…	…	…	…	…	…	…	…	…	…	…	…	…
J1348+2415	…	…	…	…	…	…	…	…	…	…	…	…	…	…	…
J1354+5650	0.68	0.40	73.2	0.14	141.9	0.32	0.29	77.8	0.11	76.2	…	…	…	…	…
J1357+0046	0.54	0.49	30.7	0.36	475.1	0.33	0.28	−30.2	0.12	229.0	14.81	5.91	0.1	0.65	401.1
J1410+4850	0.43	0.41	−54.1	0.20	115.9	0.25	0.24	6.8	0.14	63.9	10.15	6.69	9.4	0.13	94.1
J1413+1509	0.43	0.41	−89.4	0.29	221.2	…	…	…	…	…	…	…	…	…	…
J1414+4554	…	…	…	…	…	…	…	…	…	…	…	…	…	…	…

Table 10
(Continued)

Object	VLA 4.9 GHz					VLA 8.5 GHz					VLBA 1.4 GHz				
	Maj. (″)	Min. (″)	P.A. (°)	rms (mJy/beam)	S_m (mJy/beam)	Maj. (″)	Min. (″)	P.A. (°)	rms (mJy/beam)	S_m (mJy/beam)	Maj. (mas)	Min. (mas)	P.A. (°)	rms (mJy/beam)	S_m (mJy/beam)
J1415+1320	…	…	…	…	…	…	…	…	…	…	…	…	…	…	…
J1421−0246	0.68	0.46	33.7	0.13	21.6	0.32	0.24	10.1	0.11	11.9	…	…	…	…	…
J1424+1852	0.45	0.44	42.0	0.18	69.8	0.28	0.24	36.5	0.27	32.8	…	…	…	…	…
J1502+3753	0.47	0.42	61.4	0.19	32.5	0.24	0.24	46.7	0.11	11.8	…	…	…	…	…
J1504+5438	…	…	…	…	…	…	…	…	…	…	…	…	…	…	…
J1504+6000	0.55	0.44	77.0	0.41	297.1	0.35	0.29	81.3	0.15	175.1	10.29	8.68	19.1	0.60	132.5
J1523+1332	0.48	0.42	−43.0	0.15	63.1	0.29	0.26	−35.0	0.11	30.1	19.93	15.12	29.2	0.36	18.2
J1527+3312	…	…	…	…	…	0.31	0.24	41.5	0.38	73.7	13.11	7.23	9.2	0.19	59.9
J1528−0213	0.54	0.45	−13.8	0.18	60.4	0.33	0.27	−10.7	0.09	31.4	…	…	…	…	…
J1548+0808	0.68	0.41	−52.0	0.42	149.2	0.37	0.24	−51.0	0.09	59.0	49.00	37.85	17.3	3.50	113.6
J1551+6405	…	…	…	0.25	…	…	…	…	…	…	…	…	…	…	…
J1559+4349	0.51	0.42	80.6	0.19	134.3	…	…	…	…	…	18.49	15.02	66.5	0.33	30.0
J1604+6050	0.66	0.44	87.8	0.16	165.6	0.38	0.29	89.3	0.09	86.1	10.92	9.03	50.2	0.28	222.3
J1616+2647	0.46	0.41	−62.8	0.77	578.7	0.43	0.24	19.0	0.42*	605.1*	13.76	8.31	7.0	0.40	366.6
J1625+4134	…	…	…	…	…	…	…	…	…	…	…	…	…	…	…
J1629+1342	0.72	0.41	−56.5	0.14	79.8	0.40	0.24	122.3	0.07	41.2	…	…	…	…	…
J1633+4700	0.55	0.42	−84.4	0.13	73.9	0.32	0.24	89.4	0.06	35.8	27.64	23.72	27.9	0.65	26.7
J1724+3852	0.62	0.42	−71.0	0.19	126.1	0.36	0.24	102.8	0.20	68.7	12.26	8.96	−3.2	0.15	89.4
J2203−0021	0.62	0.43	38.1	0.33*	131.4*	…	…	…	…	…	…	…	…	…	…

Note. Flux densities designated with "*" lack accurate flux calibrations. See Table 1 for details.

form, unified schemes suggest that radio-loud galaxies are viewed close to the plane of a circumnuclear disk and torus (if present) while radio-loud quasars are viewed closer to the jet propagation direction. This suggests that the obscuration of the non-thermal light from the AGN is strongly related to the presence of 21 cm absorption gas. If so, this predicts the low (or zero) detection rate in high UV luminosity objects ($L_{\rm UV} > 10^{23}$ W Hz^{-1}) that has been seen by Curran & Whiting (2010).

Taken in the light of standard unified schemes, the results of this study do not bode well for finding higher redshift atomic and molecular absorption lines in the radio. However, we should not take the present results and this statement to mean that such sources do not exist, but rather that they will be quite difficult to find and study. In Paper I we embarked on a program to identify excellent candidates for discovering highly redshifted radio absorption lines by cross-correlating bright ($\geqslant$0.5 Jy) FIRST radio sources with SDSS counterparts that are less centrally concentrated than either a giant elliptical galaxy or a dominant nuclear point source typical of radio galaxies and quasars. The use of the SDSS for this work limited this search to $z \leqslant 1.0$ due to the faintness of the optical counterparts at higher redshifts (i.e., more distant AGN similar to the present sample are too faint to be detected in the SDSS photometric sample). This approximate redshift limit is confirmed by the photometric redshifts found by the SDSS and by us using NIR photometry in conjunction with the SDSS photometry in Paper I. This is specifically the case for those sources whose optical/NIR SEDs are dominated by galaxy starlight, not by AGN emission. Those few sources with quasar-like SEDs are biased toward $z > 1$ in this sample and thus at too high a UV rest-frame luminosity to be viable H I absorption candidates (Curran & Whiting 2010).

To locate and study higher redshift (>2) sources similar to the present sample does not require using fainter radio sources than the 0.3 Jy limit used here. As shown in this paper, the radio properties of such sources are easily studied with current instruments. The limiting factors are the optical/NIR identifications of faint host or intervening galaxies associated with these bright sources and obtaining spectroscopic redshifts for them. Our failure to discover significant numbers of redshifted H I absorbers using photometric redshifts alone makes the measurement of a spectroscopic redshift an essential step in this process.

The existence of sensitive IR sky surveys from the *Spitzer Space Telescope* and the *WISE* satellite can be used to construct substantial samples of optically faint (i.e., SDSS non-detects), radio, and NIR bright sources. VLBA mapping of such sources can isolate the CSO and point sources that are the best candidates for H I and molecular absorption-line searches. In a preview of this technique we used *Spitzer* IRAC and *WISE* 12 and 22 μ photometry to find that of the 13 CSOs and candidate CSOs from the present survey, 10 (7 definite and 3 probable) show mid-IR flux turnups. Of the four H I absorption-line detected CSOs observed by *WISE*, three show definite or probable mid-IR turnups. In this manner, the best candidates for the most heavily obscured radio-loud AGN can be identified. Then the problem becomes how to determine the source redshift to allow an H I detection in the forest of RFI confronting us at sub-GHz frequencies. Developing capabilities in the sub-mm wavelength regime may make such redshift determinations possible.

An alternative approach is to directly target molecular absorption at higher rest frequencies where observations would be uninhibited by significant RFI. But this would require a flat-spectrum (FS) radio source. CSOs are generally not FS sources. Instead, FS core-jet sources are generally dominated by luminous rest-frame UV continuum emission in the optical. The presence of the UV continuum appears to preclude the

Table 11
VLA 4.9 GHz Gaussian Fit Results

Object	ID	R.A. (hh mm ss.sss)	Decl. (dd mm ss.ss)	S_p (mJy /beam)	$S_{\rm tot}$ (mJy)	Maj. (″)	Min. (″)	P.A. (°)
(1)	(2)	(3)	(4)	(5)	(6)	(7)	(8)	(9)
J0000−1054	A	00 00 57.647	−10 54 32.87	35.3	42.6	0.28	0.17	40.2
	B	00 00 57.690	−10 54 31.50	18.8	23.8	0.36	0.14	32.0
J0003−1053	A	00 03 56.254	−10 53 02.49	30.7	39.6	0.30	0.23	96.1
	B	00 03 56.299	−10 53 02.47	30.5	40.5	0.40	0.07	60.0
	C	00 03 56.332	−10 53 01.92	22.3	23.0	0.11	0.07	140.9
	D	00 03 56.381	−10 53 01.06	24.3	27.8	0.21	0.17	48.7
J0134+0003		01 34 12.704	+00 03 45.14	548.3*	553.9*	0.05	0.05	106.0
J0249−0759	A	02 49 35.370	−07 59 21.92	118.9*	136.1*	0.23	0.18	5.9
	B	02 49 35.426	−07 59 20.21	55.6*	67.1*	0.29	0.23	149.8
J0749+2129	A	07 49 48.708	+21 29 33.47	44.7	63.5	0.68	0.18	27.6
	B	07 49 48.813	+21 29 32.87	28.2	36.0	0.45	0.22	27.5
	C	07 49 48.697	+21 29 34.90	8.6	10.3	0.34	0.21	43.5
J0759+5312	A	07 59 06.465	+53 12 47.95	97.8	100.1	0.11	0.07	40.5
	B	07 59 06.598	+53 12 47.23	3.7	4.5	0.34	0.24	79.9
J0805+1614	A	08 05 02.180	+16 14 05.10	107.1	114.2	0.18	0.10	72.6
	B	08 05 02.180	+16 14 04.60	69.2	73.0	0.16	0.09	72.4
J0807+5327	A	08 07 40.746	+53 27 38.63	81.9	86.3	0.15	0.10	152.9
	B	08 07 40.714	+53 27 37.60	22.1	24.9	0.27	0.16	35.9
J0824+5413	A	08 24 25.427	+54 13 48.06	62.5	79.4	0.36	0.23	112.3
	B	08 24 25.568	+54 13 49.37	35.2	48.0	0.39	0.29	139.0
J0839+2403	A	08 39 57.851	+24 03 11.27	100.8	108.0	0.12	0.10	50.9
	B	08 39 57.997	+24 03 12.52	33.9	36.9	0.15	0.09	58.2
	C	08 39 57.828	+24 03 10.57	8.2	21.9	0.70	0.39	55.5
	D	08 39 58.024	+24 03 13.72	4.5	18.6	1.00	0.52	120.9
J0901+0304		09 01 50.981	+03 04 22.66	166.5	172.5	0.14	0.06	44.9
J0903+5012	A	09 03 49.973	+50 12 36.55	233.3	268.4	0.26	0.15	105.6
	B	09 03 49.675	+50 12 34.73	11.2	22.7	0.76	0.38	81.7
J0907+0413	A	09 07 50.770	+04 13 36.30	82.5	106.9	0.38	0.14	8.6
	B	09 07 50.720	+04 13 38.80	64.0	89.7	0.41	0.23	7.5
J0910+2419	A	09 10 22.376	+24 19 19.48	97.5	118.3	0.22	0.17	91.1
	B	09 10 22.684	+24 19 19.48	51.8	78.3	0.33	0.28	109.0
J0915+1018	A	09 15 12.960	+10 18 27.20	50.2	67.5	0.31	0.21	113.1
	B	09 15 12.960	+10 18 28.00	28.3	40.6	0.34	0.27	135.1
	C	09 15 12.980	+10 18 26.10	19.9	28.5	0.36	0.23	120.2
J0917+4725		09 17 27.032	+47 25 24.07	60.9	95.7	0.58	0.29	29.3
J0920+1753	A	09 20 11.143	+17 53 25.12	167.8	181.6	0.15	0.10	24.7
	B	09 20 11.142	+17 53 24.70	106.2	113.6	0.13	0.10	159.4
J0920+2714	A	09 20 45.142	+27 14 05.58	93.0	105.0	0.20	0.15	39.1
	B	09 20 45.060	+27 14 02.90	5.7	6.9	0.23	0.20	166.1
J0939+0304		09 37 09.249	+03 18 03.33	199.9	216.0	0.17	0.12	111.6
J0945+2640	A	09 45 30.950	+26 40 53.90	161.2	171.8	0.16	0.13	154.3
	B	09 45 31.000	+26 40 48.60	7.9	16.1	0.72	0.51	170.1
	C	09 45 30.970	+26 40 53.10	3.6	11.3	1.68	0.41	29.2
J0951+1154	A	09 51 33.780	+11 54 58.20	26.0	44.3	0.46	0.32	46.7
	B	09 51 33.880	+11 55 00.70	25.6	39.8	0.37	0.32	127.3
	C	09 51 33.850	+11 54 59.70	1.4	14.7	2.10	0.95	48.5
J1008+2401	A	10 08 32.681	+24 01 19.77	57.7	84.1	0.38	0.19	77.8
	B	10 08 32.548	+24 01 18.93	10.5	21.3	0.46	0.43	44.0
J1023+0424	A	10 23 37.550	+04 24 14.20	71.3	74.4	0.12	0.07	5.5
	B	10 23 37.560	+04 24 13.60	29.0	31.7	0.20	0.00	164.8
J1034+1112	A	10 34 05.014	+11 12 30.58	120.3	143.9	0.24	0.19	153.9
	B	10 34 05.299	+11 12 33.07	41.8	53.5	0.36	0.17	71.1
	C	10 34 05.216	+11 12 32.35	16.8	61.7	1.44	0.37	61.8
	D	10 34 05.132	+11 12 31.57	6.1	9.4	0.58	0.10	80.2
	E	10 34 05.024	+11 12 31.08	15.3	56.8	1.09	0.59	95.1
J1043+0537	A	10 43 40.425	+05 37 13.01	43.5	78.4	0.58	0.28	71.5
	B	10 43 39.984	+05 37 12.28	23.8	53.0	0.62	0.44	91.5
J1045+0455	A	10 45 51.764	+04 55 52.34	51.2	92.5	0.61	0.29	2.6
	B	10 45 51.723	+04 55 49.52	14.9	32.6	0.83	0.29	16.2
J1125+1953		11 25 55.240	+19 53 43.68	101.4	113.9	0.20	0.09	2.0
J1127+5743	A	11 27 43.773	+57 43 15.84	147.8	152.1	0.09	0.06	60.0
	B	11 27 43.718	+57 43 15.63	25.4	27.7	0.16	0.10	128.2
J1129+5638		11 29 04.147	+56 38 44.14	109.6	112.9	0.11	0.03	88.6

Table 11
(Continued)

Object	ID	R.A. (hh mm ss.sss)	Decl. (dd mm ss.ss)	S_p (mJy /beam)	$S_{\rm tot}$ (mJy)	Maj. ($''$)	Min. ($''$)	P.A. ($^\circ$)
(1)	(2)	(3)	(4)	(5)	(6)	(7)	(8)	(9)
J1142+0235	A	11 42 06.370	+02 35 33.40	64.9	72.3	0.18	0.14	38.3
	B	11 42 06.390	+02 35 32.80	41.2	65.5	0.49	0.27	9.6
	C	11 42 06.380	+02 35 34.30	8.7	21.0	0.73	0.45	175.4
J1147+4818	A	11 47 52.288	+48 18 49.48	94.9	107.0	0.19	0.12	128.1
	B	11 47 52.193	+48 18 49.29	11.0	18.0	0.39	0.33	21.9
J1148+1404	A	11 48 25.410	+14 04 49.70	57.9	77.2	0.28	0.24	15.4
	B	11 48 25.440	+14 04 48.30	15.3	21.5	0.32	0.25	83.1
J1202+1207		12 02 52.086	+12 07 20.76	133.9	140.2	0.12	0.07	105.5
J1203+4632		12 03 31.795	+46 32 55.48	184.3	187.2	0.07	0.03	99.9
J1207+5407	A	12 07 14.249	+54 07 54.49	72.6	76.7	0.16	0.08	44.7
	B	12 07 14.088	+54 07 54.18	49.3	61.3	0.35	0.10	79.4
J1215+1730		12 15 14.724	+17 30 02.23	369.4	388.8	0.12	0.06	50.1
J1228+5348	A	12 28 50.815	+53 48 04.00	49.6	91.9	0.67	0.24	2.4
	B	12 28 50.487	+53 48 00.08	31.9	50.9	0.54	0.33	48.3
J1238+0845	A	12 38 19.260	+08 45 01.63	86.3	94.2	0.19	0.08	171.8
	B	12 38 19.282	+08 44 58.47	4.7	8.3	0.56	0.33	41.0
	C	12 38 19.277	+08 45 00.08	0.8	4.3	1.93	0.49	11.9
J1312+1710		13 10 07.820	+17 26 49.70	98.8	109.4	0.17	0.11	0.1
J1315+0222	A	13 15 16.950	+02 22 20.90	70.1	86.1	0.27	0.17	30.9
	B	13 15 17.020	+02 22 21.40	31.1	74.1	0.74	0.34	58.2
	C	13 15 16.880	+02 22 20.30	1.9	9.5	1.30	0.66	107.9
J1341+1032	A	13 41 04.327	+10 32 06.56	83.0	92.3	0.25	0.11	80.3
	B	13 41 04.259	+10 32 06.36	62.2	65.3	0.13	0.10	48.4
J1345+5846	A	13 45 38.379	+58 46 53.48	74.5	87.9	0.22	0.21	96.8
	B	13 45 38.319	+58 46 54.24	5.6	10.5	0.54	0.39	140.2
	C	13 45 38.261	+58 46 55.54	3.0	7.8	0.84	0.56	78.0
J1354+5650	A	13 54 00.153	+56 50 06.13	141.1	157.1	0.21	0.15	57.0
	B	13 54 00.078	+56 50 03.70	38.5	99.4	0.98	0.42	57.5
J1357+0046		13 57 53.723	+00 46 33.32	483.0	495.6	0.10	0.06	18.4
J1410+4850		14 10 36.041	+48 50 40.35	117.0	118.7	0.07	0.01	11.9
J1413+1509		14 13 41.657	+15 09 39.51	233.7	236.4	0.06	0.01	151.3
J1421−0246	A	14 21 13.600	−02 46 44.33	21.0	52.9	0.87	0.53	7.1
	B	14 21 13.550	−02 46 45.94	12.6	27.3	1.01	0.31	32.0
	C	14 21 13.516	−02 46 47.63	20.2	53.3	0.87	0.57	176.2
J1424+1852	A	14 24 09.691	+18 52 52.21	68.0	85.3	0.29	0.14	20.6
	B	14 24 09.736	+18 52 53.69	71.2	79.8	0.18	0.13	40.6
J1502+3753	A	15 02 34.755	+37 53 54.49	14.4	19.9	0.44	0.00	102.4
	B	15 02 34.794	+37 53 52.50	10.5	12.4	0.25	0.06	127.0
	C	15 02 34.758	+37 53 53.54	9.0	22.0	0.92	0.09	142.8
	D	15 02 34.755	+37 53 54.27	21.0	46.9	0.79	0.17	175.1
J1504+6000	A	15 04 09.195	+60 00 55.68	306.8	323.7	0.12	0.11	13.4
	B	15 04 09.240	+60 00 55.16	128.8	138.9	0.16	0.11	119.1
J1523+1332	A	15 23 21.735	+13 32 29.11	62.5	76.5	0.23	0.20	171.0
	B	15 23 21.946	+13 32 31.23	1.9	3.0	0.38	0.26	80.7
J1528−0213	A	15 28 22.030	−02 13 19.67	56.4	91.3	0.47	0.31	165.7
	B	15 28 22.047	−02 13 18.30	52.1	67.5	0.29	0.25	9.1
J1548+0808		15 48 09.076	+08 08 34.73	152.4	187.4	0.29	0.05	36.8
J1559+4349	A	15 59 31.221	+43 49 17.18	135.3	143.7	0.16	0.06	82.2
	B	15 59 31.158	+43 49 16.77	50.0	59.5	0.25	0.11	16.5
J1604+6050		16 04 27.402	+60 50 55.25	168.4	168.6	0.03	0.00	121.5
J1616+2647		16 16 38.327	+26 47 01.50	579.3	610.2	0.14	0.00	107.6
J1629+1342	A	16 29 48.558	+13 42 05.71	65.8	81.5	0.38	0.16	102.4
	B	16 29 48.222	+13 42 07.23	77.5	96.6	0.36	0.19	101.7
J1633+4700	A	16 33 15.206	+47 00 16.31	74.6	82.8	0.18	0.13	138.9
	B	16 33 15.148	+47 00 16.74	1.3	3.9	1.30	0.25	82.3
	C	16 33 14.898	+47 00 17.42	2.7	13.2	1.95	0.38	104.6
	D	16 33 14.722	+47 00 17.89	17.2	32.4	0.64	0.28	124.0
J1724+3852		17 24 00.537	+38 52 26.63	127.7	130.3	0.09	0.06	112.7
J2203−0021	A	22 03 58.311	−00 21 47.46	127.7*	144.8*	0.21	0.15	85.6
	B	22 03 58.325	−00 21 48.31	134.4*	152.9*	0.22	0.13	107.0

Note. Flux densities designated with "*" lack accurate flux calibrations. See Table 1 for details.

Table 12
VLA 8.5 GHz Gaussian Fit Results

Object	ID	S_p (mJy /beam)	$S_{\rm tot}$ (mJy)	Maj. (″)	Min. (″)	P.A. (°)	α
(1)	(2)	(3)	(4)	(5)	(6)	(7)	(8)
J0000−1054	A	17.5	23.3	0.19	0.13	66.4	−1.1
	B	7.9	11.9	0.27	0.14	33.4	−1.2
J0003−1053	A	13.1	22.7	0.35	0.24	99.6	−1.0
	B	16.7	22.7	0.31	0.09	68.9	−1.0
	C	22.3	22.5	0.06	0.00	2.8	0.0
	D	13.2	16.1	0.19	0.15	49.1	−1.0
J0249−0759	A	138.3*	172.8*	0.20	0.16	13.9	⋯
	B	67.7*	89.1*	0.23	0.19	118.3	⋯
J0749+2129	A	18.3	31.7	0.61	0.14	26.8	−1.2
	B	13.1	17.4	0.33	0.18	21.8	−1.3
	C	3.5	4.7	0.35	0.19	43.1	−1.4
J0759+5312	A	53.4	55.1	0.08	0.05	67.1	−1.1
	B	1.4	2.0	0.34	0.13	81.9	−1.5
J0805+1614	A	89.1	93.4	0.06	0.05	74.0	−0.4
	B	54.5	57.8	0.07	0.05	136.9	−0.4
J0807+5327	A	41.1	45.3	0.13	0.09	139.7	−1.2
	B	11.8	15.2	0.21	0.18	57.3	−0.9
J0824+5413	A1	32.8	40.8	0.19	0.16	157.8	−1.2
	A2	2.7	6.7	0.48	0.41	136.5	⋯
	B	16.2	26.2	0.33	0.23	122.6	−1.1
J0834+1700		219.0	299.4	0.18	0.13	53.7	⋯
J0903+5012	A	118.9	134.3	0.13	0.09	102.5	−1.2
	B	2.9	9.1	0.73	0.25	85.3	−1.6
J0917+4725		21.6	47.8	0.41	0.22	31.1	−1.2
J0920+2714	A	40.8	50.0	0.18	0.09	50.8	−1.3
	B	2.6	4.3	0.38	0.10	68.3	−0.9
J0951+1154	A	13.2	21.7	0.44	0.33	15.5	−1.1
	B	15.6	22.1	0.35	0.25	53.5	−1.2
	C	1.2	7.7	2.04	0.55	24.9	−1.2
J1023+0424	A	38.5	39.2	0.04	0.03	68.0	−1.2
	B	16.6	17.8	0.11	0.04	67.7	−1.0
J1034+1112	A	51.0	83.0	0.25	0.21	174.4	−1.0
	B	17.8	28.2	0.30	0.15	78.0	−1.2
	C	4.7	41.9	1.69	0.34	63.3	−0.7
	D	2.7	4.9	0.42	0.10	55.7	−1.2
	E	7.7	10.1	0.20	0.13	64.6	3.1
J1045+0455	A	22.3	50.6	0.55	0.26	3.3	−1.1
	B	6.9	15.9	0.64	0.22	16.3	−1.3
J1127+5743	A	78.7	82.5	0.08	0.06	172.5	−1.1
	B	14.3	18.6	0.24	0.14	156.3	−0.7
J1129+5638		53.8	56.5	0.08	0.07	121.2	−1.2
J1142+0235	A	37.6	43.5	0.12	0.11	146.8	−0.9
	B	15.0	34.6	0.45	0.24	6.3	−1.1
	C	1.9	13.1	0.85	0.61	162.7	−0.8
J1147+4818	A	50.0	55.5	0.14	0.09	99.6	−1.2
	B	3.6	7.2	0.48	0.29	83.9	−1.6
J1148+1404	A	30.3	44.4	0.20	0.17	166.8	−1.0
	B	10.8	13.2	0.14	0.12	36.2	−0.9
J1202+1207		88.6	93.9	0.09	0.05	150.9	−0.7
J1207+5407	A	32.4	36.1	0.16	0.06	78.4	−1.4
	B	19.0	26.4	0.32	0.11	86.9	−1.5
J1228+5348	A	30.6	54.5	0.64	0.25	2.1	−0.9
	B	15.1	27.2	0.49	0.36	27.8	−1.1
J1238+0845	A	40.9	48.3	0.16	0.08	169.4	−1.2
	B	1.9	4.4	0.43	0.25	14.4	−1.1
J1312+1710		56.5	60.5	0.09	0.06	157.2	−1.1
J1315+0222	A	30.3	50.5	0.26	0.14	26.3	−1.0
	B1	11.8	19.2	0.23	0.16	92.9	−1.3
	B2	5.3	17.2	0.46	0.31	98.1	⋯
J1341+1032	A	35.1	47.3	0.25	0.07	83.5	−1.2
	B	31.2	33.6	0.09	0.07	54.9	−1.2
J1345+5846	A	36.2	47.2	0.20	0.13	147.5	−1.1
	B	5.3	6.1	0.14	0.10	136.8	−1.0
	C	0.6	5.8	1.07	0.77	57.8	−0.5
J1354+5650	A	75.0	88.0	0.14	0.11	66.9	−1.0
	B1	18.6	24.3	0.20	0.13	38.0	−1.1
	B2	8.2	31.1	0.59	0.43	118.4	⋯
J1357+0046		229.0	240.0	0.09	0.02	51.5	−1.3
J1410+4850		65.5	66.4	0.04	0.00	13.2	−1.0
J1421−0246	A	4.7	34.2	0.88	0.56	179.2	−0.8
	B	11.6	12.9	0.14	0.04	7.9	−1.3
	C	4.1	31.9	0.84	0.63	177.9	−0.9
J1424+1852	A	20.1	32.4	0.25	0.17	26.7	−1.7
	B	32.1	42.8	0.22	0.08	34.8	−1.1
J1502+3753	A	11.4	24.3	0.28	0.23	145.1	0.4
	B	3.8	5.7	0.20	0.14	128.0	−1.4
	C1	4.7	7.9	0.31	0.04	152.8	−1.2
	C2	3.2	3.6	0.11	0.04	13.8	⋯
	D	5.7	13.1	0.40	0.15	46.4	−2.3
J1504+6000	A	173.7	183.7	0.09	0.05	143.4	−1.0
	B	59.3	71.5	0.19	0.08	135.1	−1.2
J1523+1332	A	28.9	38.6	0.18	0.12	31.1	−1.2
	B	1.3	3.1	0.38	0.25	13.0	0.1
J1527+3312		73.8	81.0	0.13	0.03	46.6	⋯
J1528−0213	A	28.6	48.1	0.30	0.19	164.0	−1.2
	B	25.6	39.4	0.22	0.21	28.5	−1.0
J1548+0808	A1	42.5	43.9	0.06	0.04	166.8	−1.1
	A2	51.9	55.7	0.09	0.05	15.1	⋯
J1559+4349	A	68.4	79.6	0.15	0.05	85.4	−1.1
	B	22.2	30.2	0.20	0.10	13.7	−1.2
J1604+6050		86.1	86.2	0.03	0.00	126.9	−1.2
J1616+2647		650.6*	717.8*	0.14	0.08	29.2	⋯
J1629+1342	A	28.1	39.8	0.27	0.14	108.6	−1.3
	B	39.9	52.1	0.20	0.14	96.0	−1.1
	C	4.2	4.8	0.14	0.09	127.4	⋯
J1633+4700	A	34.6	37.6	0.09	0.06	150.1	−1.4
	B	4.0	9.5	0.42	0.21	154.2	1.6
	C	1.1	1.8	0.36	0.04	119.5	−3.6
	D1	0.4	6.8	1.99	0.52	122.6	−0.6
	D2	3.8	7.4	0.32	0.22	119.1	⋯
	D3	6.2	9.1	0.22	0.15	44.0	⋯
J1724+3852		71.6	72.8	0.06	0.01	140.9	−1.0

Note. Flux densities designated with "*" lack accurate flux calibrations. See Table 1 for details.

presence of strong absorption (Vermeulen et al. 2003; Curran & Whiting 2010). While very rare, FS core-jet sources whose optical/NIR continuum is dominated by galaxy starlight would be promising targets for redshifted absorption-line studies. However, blind surveys for molecular absorption in such sources have been unsuccessful up to now (e.g., Murphy et al. 2003; Kanekar et al. 2014).

A detailed description of all of the sources in the sample on which this work is based can be found in the dissertation of the first author (Yan 2013).

This work was supported financially by National Science Foundation grant AST-0707480 (JTS, PI). In addition, T.Y. acknowledges financial support for this work from an NRAO

Table 13
VLBA 1.4 GHz Gaussian Fit Results

Object	ID	R.A. (hh mm ss.ssss)	Decl. (dd mm ss.sss)	S_p (mJy /beam)	$S_{\rm tot}$ (mJy)	Maj. (mas)	Min. (mas)	P.A. (°)
(1)	(2)	(3)	(4)	(5)	(6)	(7)	(8)	(9)
J0759+5312	a	07 59 06.4744	+53 12 47.943	8.4	20.9	13	8	97.9
	b	07 59 06.4792	+53 12 47.917	1.5	7.3	21	15	119.3
	c	07 59 06.4664	+53 12 47.956	62.7	132.3	11	7	51.0
	d	07 59 06.4638	+53 12 47.938	8.8	43.2	26	12	32.3
J0805+1614	a	08 05 02.1877	+16 14 05.223	92.7	175.5	11	9	118.5
	b	08 05 02.1832	+16 14 04.772	37.4	87.6	13	11	95.7
J0807+5327		08 07 40.7482	+53 27 38.624	43.3	103.1	109	34	125.1
J0834+1700	a	08 34 48.2174	+17 00 42.594	10.8	69.0	51	31	107.5
	b	08 34 48.2126	+17 00 42.608	61.8	184.1	31	18	100.7
	c	08 34 48.2102	+17 00 42.634	11.3	57.6	52	23	91.6
J0901+0304		09 01 50.9780	+03 04 22.709	181.8	295.0	11	5	1.2
J0917+4725		09 17 27.0198	+47 25 23.865	7.4	24.7	90	63	110.2
J0920+2714		09 20 45.1428	+27 14 05.620	32.1	157.2	52	36	149.7
J0939+0304	a	09 39 45.1424	+03 04 26.491	137.9	165.3	4	3	101.0
	b	09 39 45.1429	+03 04 26.491	38.1	94.3	15	5	98.7
	c	09 39 45.1459	+03 04 26.485	2.6	49.9	79	20	84.5
	d	09 39 45.1577	+03 04 26.472	9.2	38.5	21	14	118.4
J0945+2640		09 45 30.9555	+26 40 54.063	52.0	205.8	27	13	67.1
J1023+0424	a	10 23 37.5518	+04 24 14.332	29.9	124.4	24	10	135.0
	b	10 23 37.5508	+04 24 13.757	14.1	57.9	19	15	172.1
J1048+3457	a	10 48 34.2480	+34 57 25.042	69.4	203.0	12	4	104.8
	b	10 48 34.2487	+34 57 25.055	27.3	203.5	18	13	73.6
J1125+1953		11 25 55.2424	+19 53 43.699	19.4	100.0	31	16	26.2
J1127+5743	a	11 27 43.7751	+57 43 15.861	187.3	243.5	13	8	18.8
	b	11 27 43.7732	+57 43 15.852	56.7	158.4	31	22	86.7
	c	11 27 43.7144	+57 43 15.669	7.0	21.9	33	24	41.3
J1129+5638	a	11 29 04.1439	+56 38 44.047	80.7	237.7	16	8	158.4
	b	11 29 04.1370	+56 38 44.042	50.4	96.2	9	6	139.8
	c	11 29 04.1343	+56 38 44.056	12.7	61.5	21	12	145.3
J1147+4818	a	11 47 52.2965	+48 18 49.522	9.8	38.2	29	14	103.2
	b	11 47 52.2900	+48 18 49.541	24.0	61.6	21	10	108.7
	c	11 47 52.2868	+48 18 49.538	31.5	98.6	27	10	93.9
	d	11 47 52.2804	+48 18 49.518	20.4	40.7	18	6	72.0
	e	11 47 52.2744	+48 18 49.484	2.9	11.9	44	6	57.4
	f	11 47 52.2783	+48 18 49.375	3.6	20.8	37	19	67.6
J1148+1404	a	11 48 25.4153	+14 04 49.937	9.8	20.4	51	4	119.4
	b	11 48 25.4204	+14 04 49.869	7.9	37.6	106	34	130.8
	c	11 48 25.4474	+14 04 48.424	12.1	19.6	35	10	119.5
J1202+1207	a	12 02 52.0847	+12 07 20.869	20.4	103.0	22	14	83.7
	b	12 02 52.0833	+12 07 20.823	28.4	58.0	18	4	18.1
	c	12 02 52.0844	+12 07 20.781	7.4	21.3	13	11	100.0
	d	12 02 52.0863	+12 07 20.774	17.0	73.6	22	12	124.0
J1238+0845	a	12 38 19.2580	+08 45 01.677	29.2	78.9	41	21	71.3
	b	12 38 19.2596	+08 45 01.660	24.4	53.4	36	17	57.1
	c	12 38 19.2601	+08 45 01.624	11.3	37.8	48	18	172.4
J1312+1710	a	13 12 35.2134	+17 10 55.914	23.0	27.3	8	0	72.2
	b	13 12 35.2125	+17 10 55.905	31.0	103.4	24	7	66.2
	c	13 12 35.2098	+17 10 55.892	12.9	43.6	20	10	97.9
J1345+5846		13 45 38.3909	+58 46 53.462	16.1	70.9	53	18	91.4
J1357+0046	a	13 57 53.7245	+00 46 33.354	390.7	929.4	15	5	46.8
	b	13 57 53.7216	+00 46 33.326	107.2	153.1	6	3	56.5
	c	13 57 53.7201	+00 46 33.298	117.1	449.5	23	9	34.0
J1410+4850	a	14 10 36.0386	+48 50 40.386	52.5	106.2	11	6	38.4
	b	14 10 36.0381	+48 50 40.344	88.1	147.0	9	4	52.3
J1504+6000	a	15 04 09.2075	+60 00 55.711	78.3	528.7	38	12	57.3
	b	15 04 09.2514	+60 00 55.158	45.7	131.1	15	11	175.6
J1523+1332	a	15 23 21.7418	+13 32 29.339	6.2	17.0	32	15	58.2
	b	15 23 21.7302	+13 32 29.113	14.1	27.7	19	14	112.6
	c	15 23 21.7321	+13 32 29.171	4.9	29.1	58	23	89.9
	d	15 23 21.7298	+13 32 29.139	6.7	87.0	92	37	126.6
J1527+3312		15 27 50.8757	+33 12 52.903	45.1	187.3	23	12	170.3
J1548+0808	a	15 48 09.0791	+08 08 34.890	112.5	180.4	43	22	60.7

Table 13
(Continued)

Object	ID	R.A. (hh mm ss.ssss)	Decl. (dd mm ss.sss)	S_p (mJy /beam)	S_{tot} (mJy)	Maj. (mas)	Min. (mas)	P.A. (°)
(1)	(2)	(3)	(4)	(5)	(6)	(7)	(8)	(9)
	b	15 48 09.0730	+08 08 34.661	85.5	135.6	44	16	135.6
J1559+4349	a	15 59 31.2239	+43 49 17.191	27.1	99.9	40	17	99.5
	b	15 59 31.2188	+43 49 17.206	27.3	82.8	35	14	102.5
	c	15 59 31.2140	+43 49 17.197	23.5	66.3	31	15	91.3
	d	15 59 31.1898	+43 49 17.051	4.2	9.1	31	8	57.1
	e	15 59 31.1556	+43 49 16.825	15.5	54.2	42	13	22.6
J1604+6050	a	16 04 27.4134	+60 50 55.197	219.9	257.3	5	4	74.0
	b	16 04 27.4116	+60 50 55.201	208.8	234.5	4	2	108.9
J1616+2647	a	16 16 38.3289	+26 47 01.516	315.3	416.0	8	5	170.4
	b	16 16 38.3288	+26 47 01.505	93.6	255.3	17	11	25.2
	c	16 16 38.3258	+26 47 01.399	148.4	408.3	22	9	19.4
J1633+4700		16 33 15.2092	+47 00 16.321	22.6	107.0	54	45	152.7
J1724+3852	a	17 24 00.5298	+38 52 26.652	82.5	159.1	10	9	76.5
	b	17 24 00.5274	+38 52 26.680	49.2	97.9	17	4	150.0

studentship and an observing grant from the *Spitzer Space Telescope* under project number 1439221. This work is a portion of the PhD dissertation of T.Y. presented to the Astrophysical & Planetary Sciences Department at the University of Colorado, Boulder.

Facilities: VLA, VLBA, Green Bank Telescope, Arecibo, GMRT, ARC, Gemini.

APPENDIX
BASIC RADIO SOURCE DATA AND MAPS FROM VLA-A AND VLBA

Table 10 lists basic observational parameters for all radio maps made for each source in the sample, including the following information: the major and minor axis sizes in arcsecs, the position angle (P.A.; angle east of north) of the restored beam, the map rms (σ) in the vicinity of the source in mJy per beam, and the maximum flux density in mJy per beam in the map. The median rms for the maps in Figure 14 is 0.19, 0.12, and 0.36 mJy at 4.9 GHz, 8.5 GHz, and 1.4 GHz (VLBA), respectively. Dynamic ranges of up to a few hundred are generally achieved through self-calibration. The median major axis value of the restored beam is $0\farcs5$, $0\farcs3$, and 15 milliarc seconds at 4.9 GHz, 8.5 GHz, and 1.4 GHz, respectively. For a few VLBA 1.4 GHz observations, the data were tapered to exclude long baselines with no signal.

Our VLA and VLBA images are shown in Figure 14. Each image has five contour levels ranging from 3σ to $0.8S_m$ and logarithmically spaced, where S_m is the maximum flux density; that is, by assuming $R = 0.8S_m/3\sigma$, the contour levels are (1, $R^{1/4}$, $R^{2/4}$, $R^{3/4}$, R) $\times$ 3σ. A negative 3σ value is shown as a dashed line. In the 4.9 and 1.4 GHz images, the optical centroid position in the *r*-band is labeled in blue with uncertainties along the R.A. and decl. axes. The red cross is the NIR centroid position (usually K_s band) with uncertainties. A green rectangle in the 4.9 GHz images represents the boundary of the object's 1.4 GHz VLBA image where available. Therefore, even if an object's NIR and/or optical position crosses are completely or partly outside its 1.4 GHz VLBA image, their relative positions can be inferred from the crosses and rectangle in the 4.9 GHz images. Center coordinates of the 4.9 GHz and 1.4 GHz images are shown at the bottom of each plot. Relative positions along R.A. and decl. are labeled on the "*X*" and "*Y*" axes, respectively. Please note that absolute 8.5 GHz astrometry is problematical and, for this reason, the central coordinates of the 8.5 GHz images are not given.

The 4.9 GHz images are overlaid with NIR images (see Paper I). K_s-band images are used with two exceptions: J1125 +1953 was not detected in the K_s band, so its *J*-band image is used. J1502+3753 was not observed in the K_s band, so its *H*-band image is used. NIR images have been re-gridded and smoothed by cubic interpolation to match the resolution of the 4.9 GHz images. This procedure sometimes resulted in artificially fracturing diffuse emission in the NIR image, due to trying to match the radio resolution. Pixel counts are displayed by grayscale where 0 is white and 1 is dark, and where 1 represents the maximum pixel count in the object and 0 and 0.2 represent the -2.5σ and $+2.5\sigma$ noise of the sky background, respectively. Between 0.2 and 1 the gray shade scales linearly with pixel counts. The host galaxies of these sources are often quite diffuse and irregular in morphology, as can be seen in the overlaid images and discussed in detail in Paper I. These asymmetrical morphologies make the determination of a galaxy centroid quite uncertain, often with errors much larger than the fitting errors shown on the radio maps.

For each radio image, we fit major components with elliptical Gaussian profiles and report the results in Tables 11–13 for the 4.9, 8.5, and 1.4 GHz VLBA images, respectively. Tables 11 and 13 list (1) object name, (2) component ID, (3, 4) R.A. and decl. of the component, (5, 6) peak and integrated flux density, and (7–9) deconvolved major axis, minor axis, and P. A. of the Gaussian component (angle east of north). The 8.5 GHz results are shown in Table 12 without coordinate information for the reason mentioned in Section 3.1. Without reliable astrometry, we match components in the 4.9 and 8.5 GHz images by eye, and mark the same component with the same letter ID. The associations are unambiguous in all cases despite the lack of accurate astrometrical registration. Spectral index data for each component in Column (8) of Table 12 is calculated between 4.9 and 8.5 GHz. In cases in which one component at 4.9 GHz is resolved into several components at 8.5 GHz, each sub-component is named by the letter ID at 4.9 GHz followed by a number, and the component flux

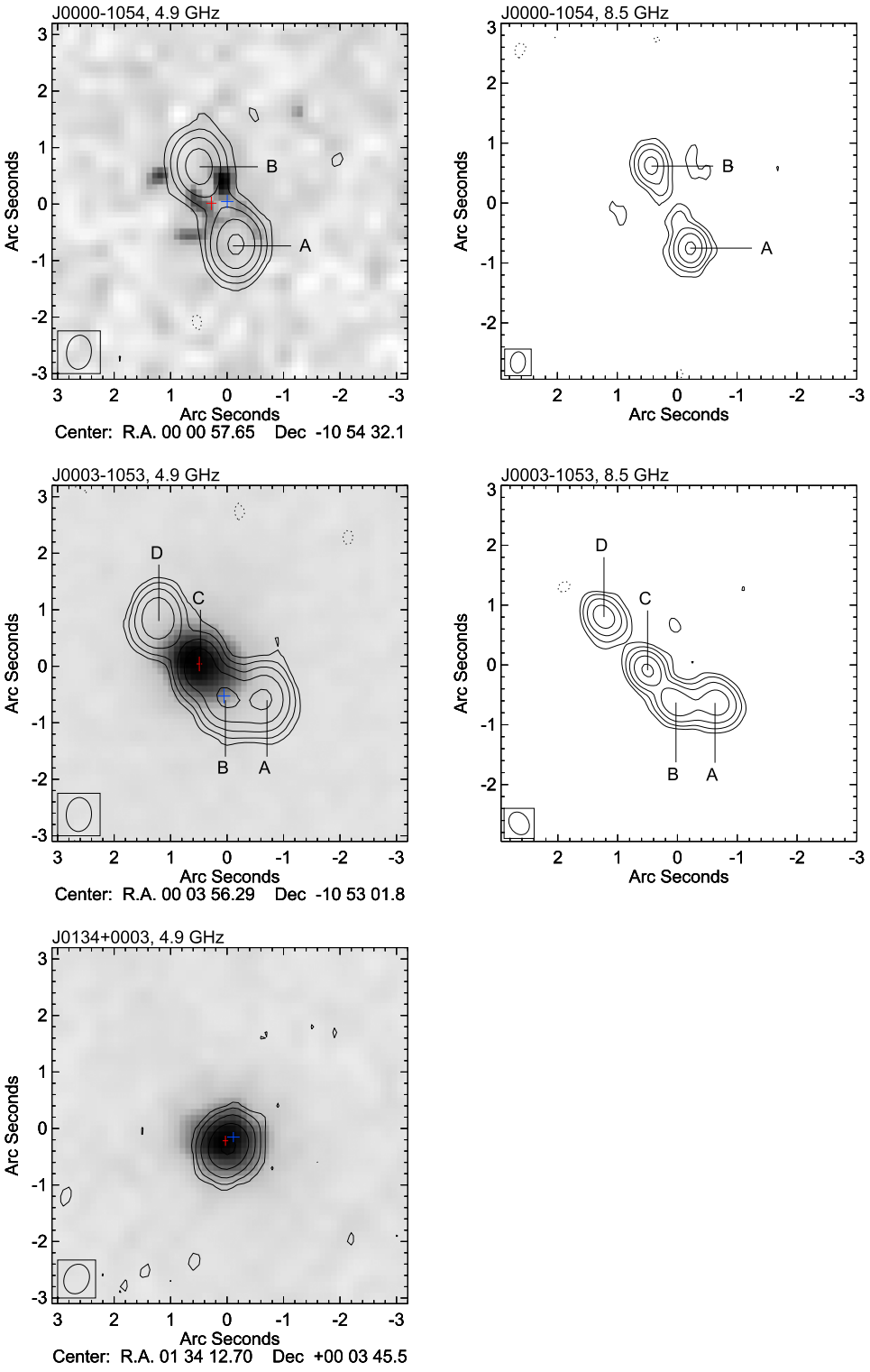

Figure 14. VLA 4.9 GHz, VLA 8.5 GHz, and VLBA 1.4 GHz images (left to right columns) for all sources observed in this study. The VLA and VLBA maps obtained for each individual source occupy one row in this figure. Each image has five contour levels ranging from 3σ to 0.8 F_m and logarithmically spaced, where F_m is the maximum of pixel counts, that is, assuming $R = 0.8F_m/3\sigma$, the contour levels are $(1, R^{1/4}, R^{2/4}, R^{3/4}, R) \times 3\sigma$. Where present, a negative 3σ value is shown as a dashed line. In the 4.9 and 1.4 GHz images, the optical centroid position in the r-band is shown as a blue cross with uncertainties. The red cross is the NIR centroid position (usually K_s-band) with uncertainties. A green rectangle in a 4.9 GHz image represents the boundary of the object's 1.4 GHz VLBA image where available (usually very small; see VLBA map field of view in righthand column). Therefore, even if an object's NIR and/or optical position crosses are completely or partly outside its 1.4 GHz image, their relative positions can be inferred from the crosses and rectangle in the 4.9 GHz image. The absolute coordinates of the map center of the 4.9 and 1.4 GHz VLBA images are shown at the bottom of each plot. Relative R.A. and decl. positions are labeled on the X and Y axes, respectively. We note that absolute 8.5 GHz astrometry is problematic (see Section 3.1) and the central coordinates of the 8.5 GHz images are not given for this reason. The 4.9 GHz images are overlaid with NIR images from the APO 3.5m telescope (see Paper I). NIR images have been re-gridded and smoothed by cubic interpolation to match the astrometry of the 4.9 GHz images. Nevertheless, in some cases, for the most diffuse sources the NIR images become fractured by the gridding in this display. See Paper I and Yan (2013) for better-quality NIR images where required. Pixel counts are displayed by grayscale between 0 (white) to 1 (dark), where 1 represents the maximum pixel count of the object; 0 and 0.2 represent the $-2.5\ \sigma$ and 2.5σ noise of the sky background, respectively; and between 0.2 and 1 the gray shade scales linearly with pixel counts between these extremes. The restored beam is shown at the lower left corner of each image. J0834+1700 and J1527+3312 have no 4.9 GHz images, so we overlaid their NIR images on the 8.5 GHz images. For those two cases, we label the optical and NIR centroid positions on their 8.5 GHz images, as well as the field of view of the 1.4 GHz VLBA images.

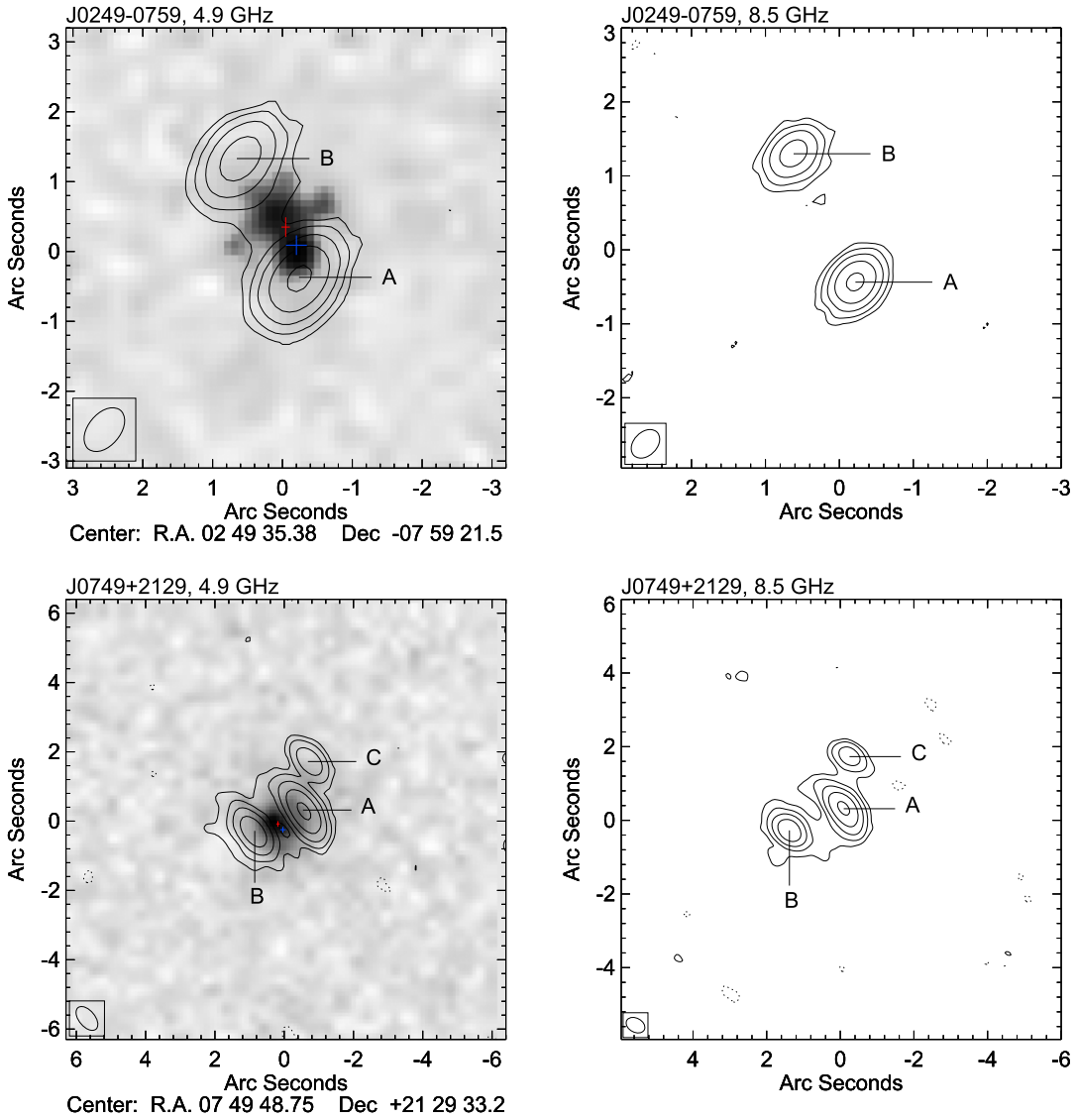

Figure 14. (Continued.)

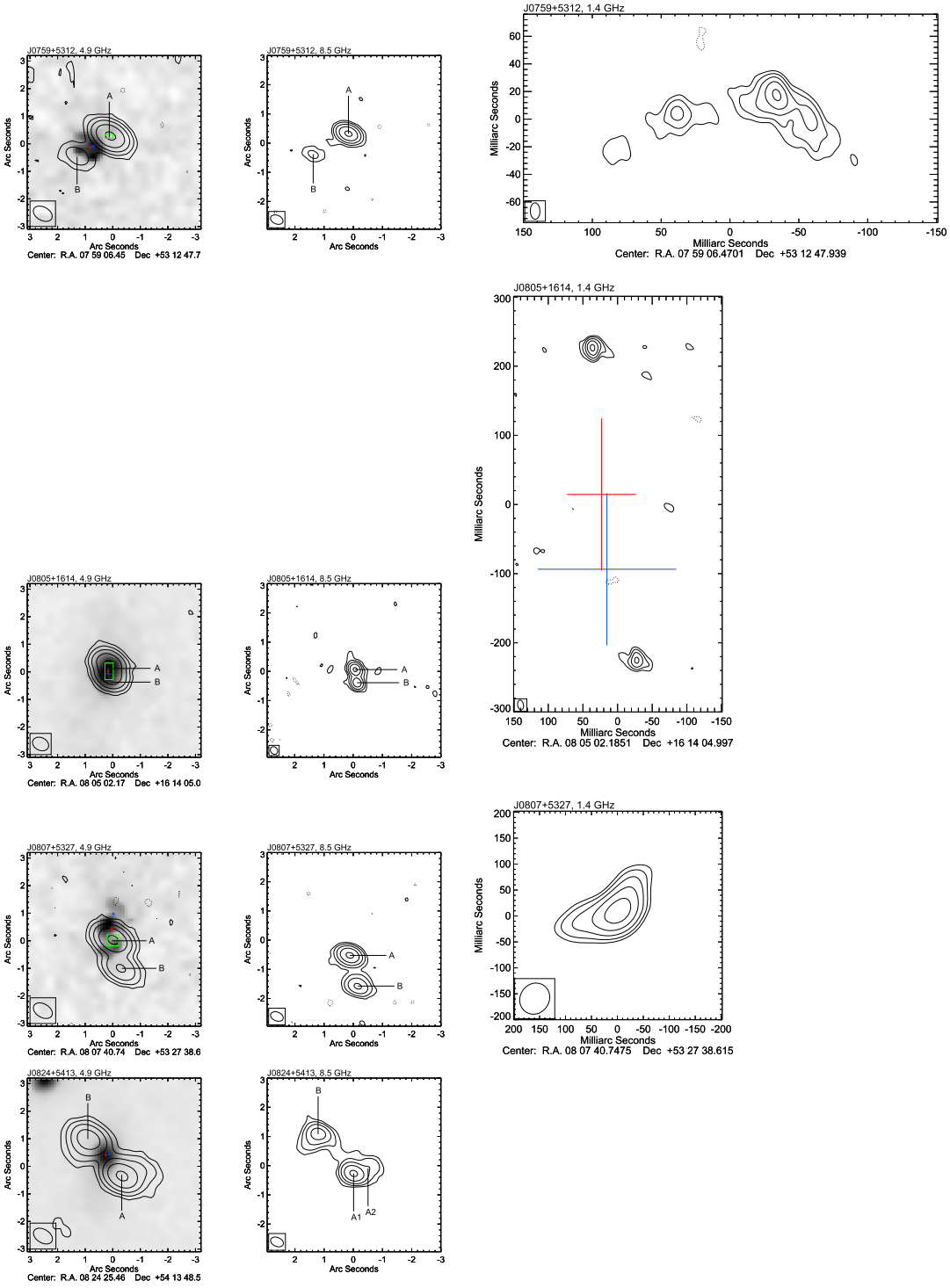

Figure 14. (Continued.)

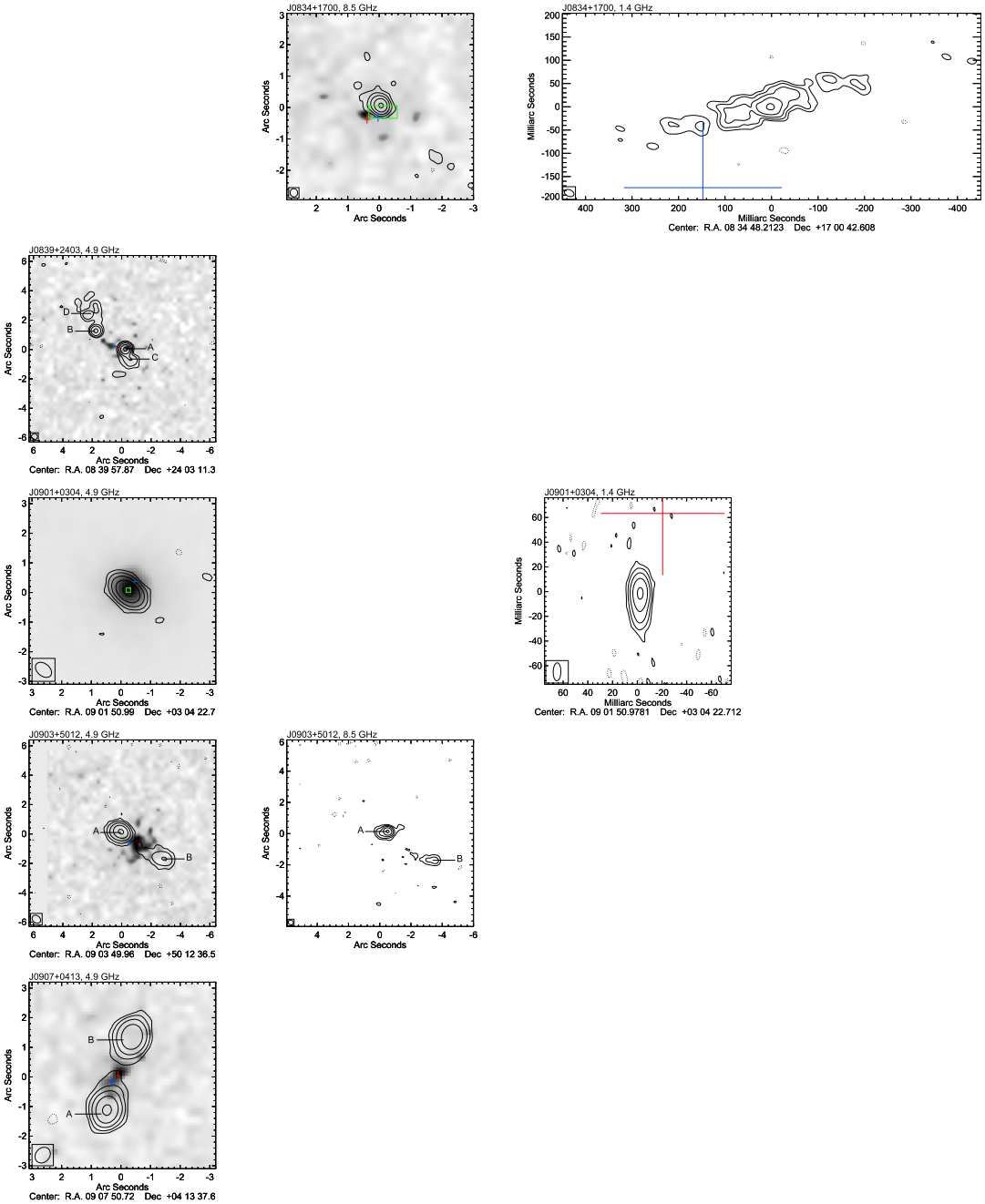

Figure 14. (Continued.)

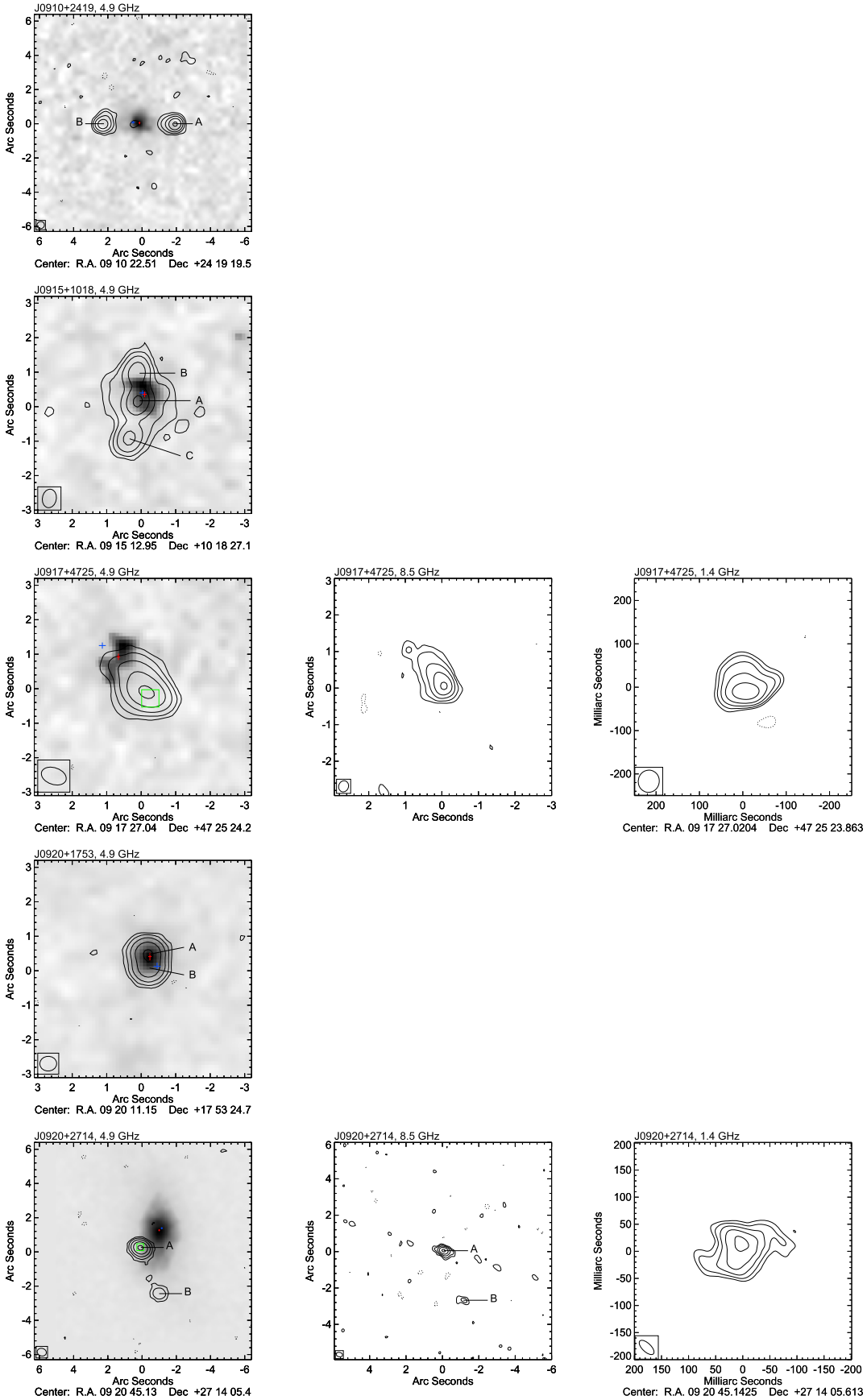

Figure 14. (Continued.)

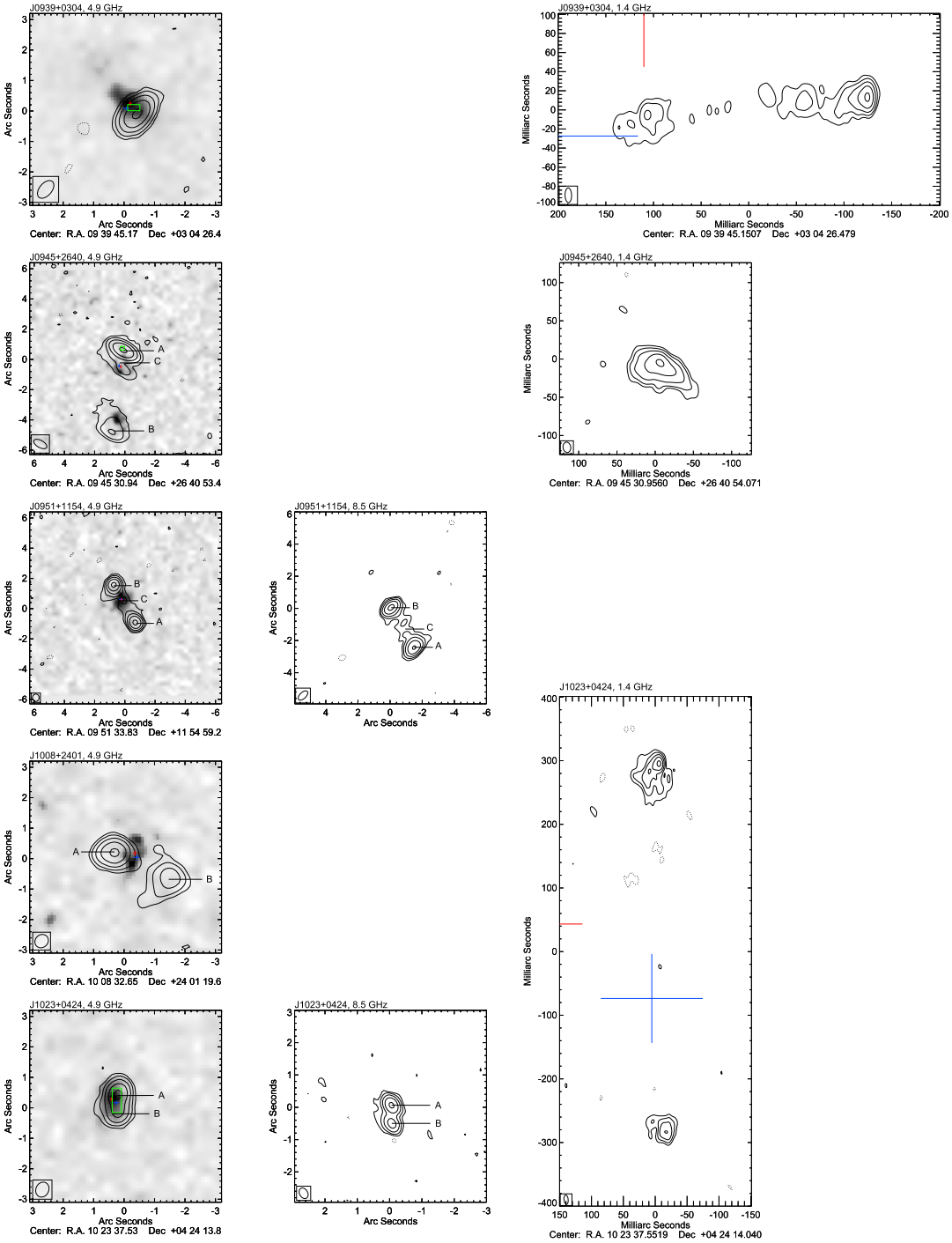

Figure 14. (Continued.)

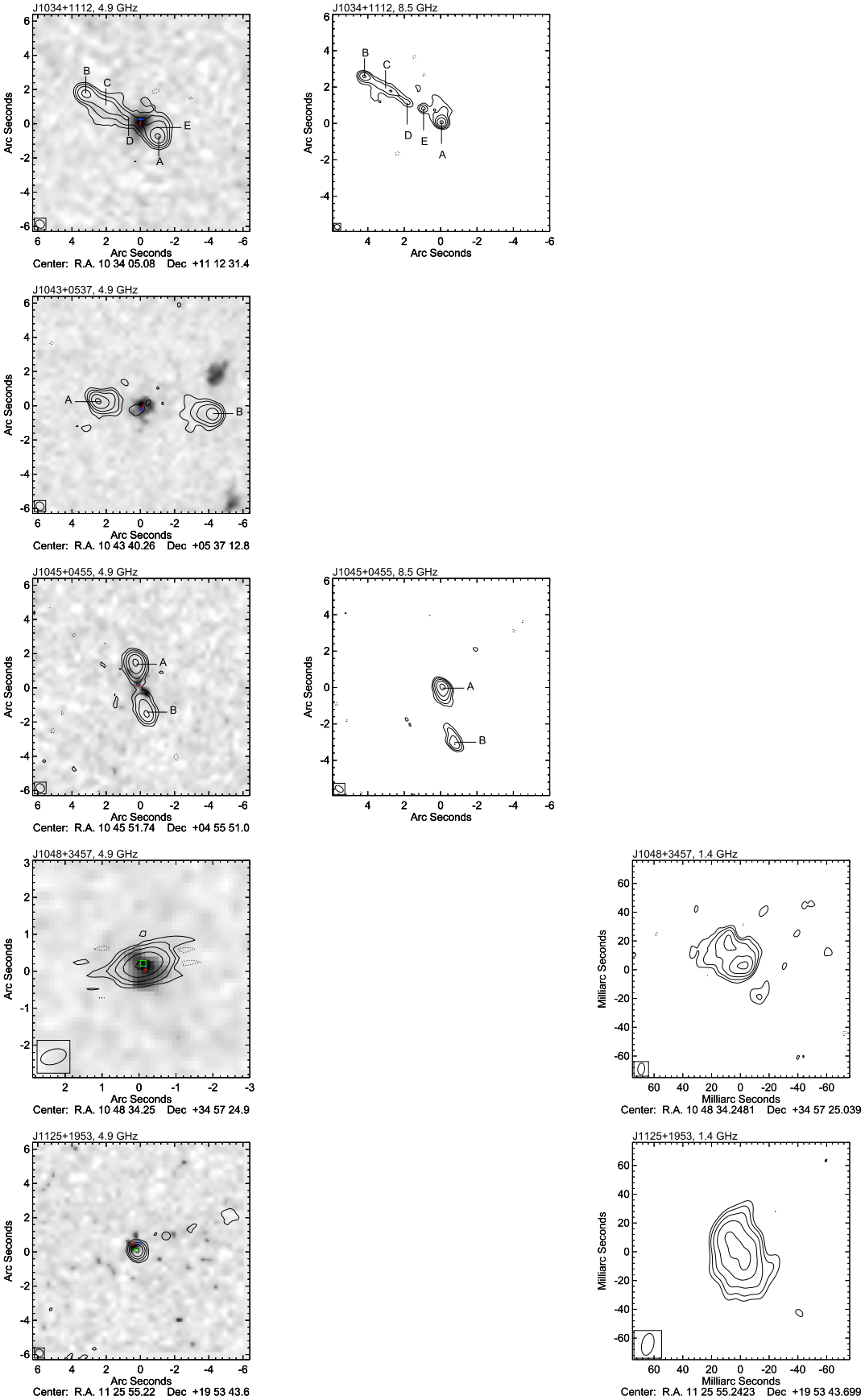

Figure 14. (Continued.)

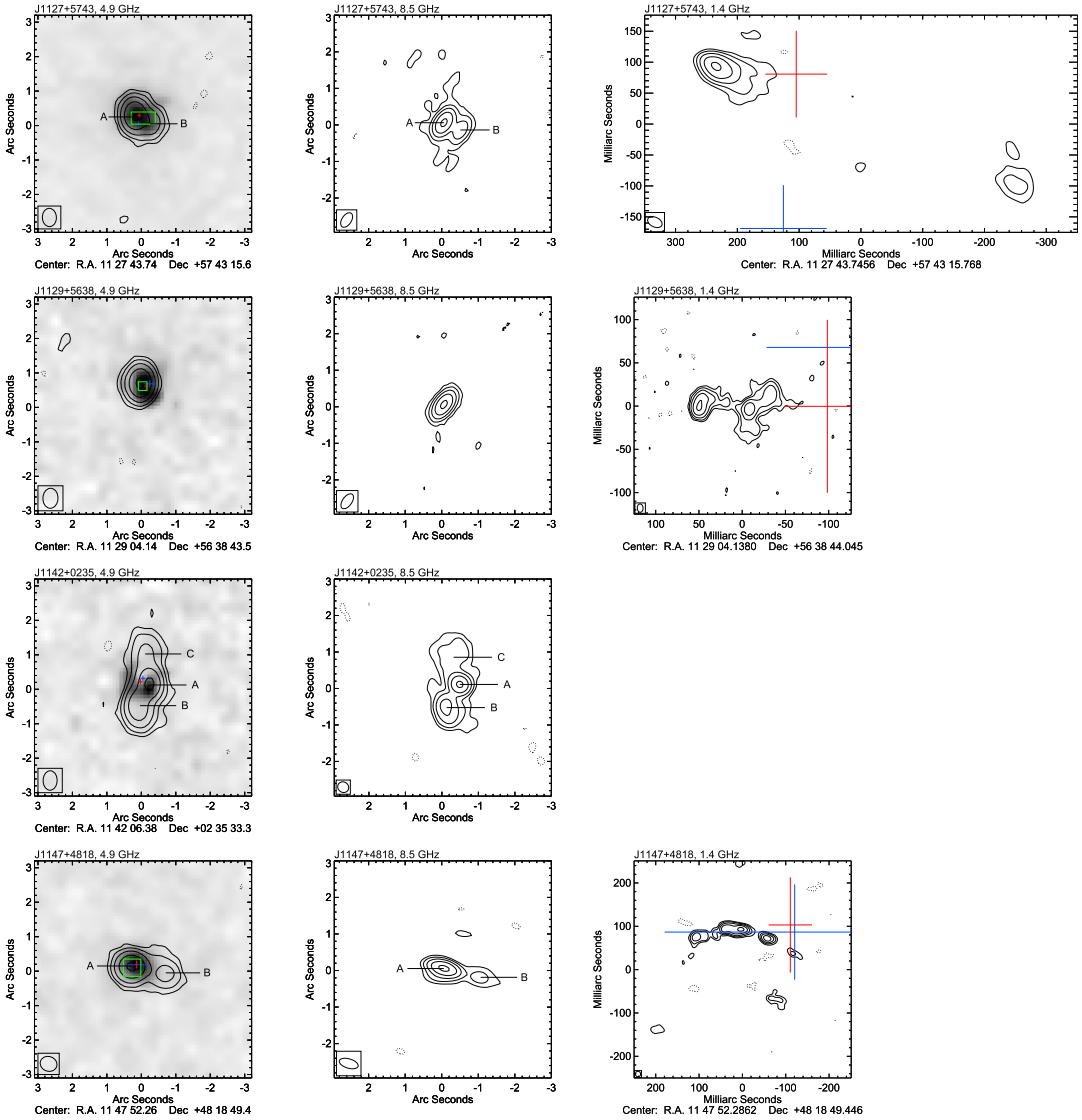

Figure 14. (Continued.)

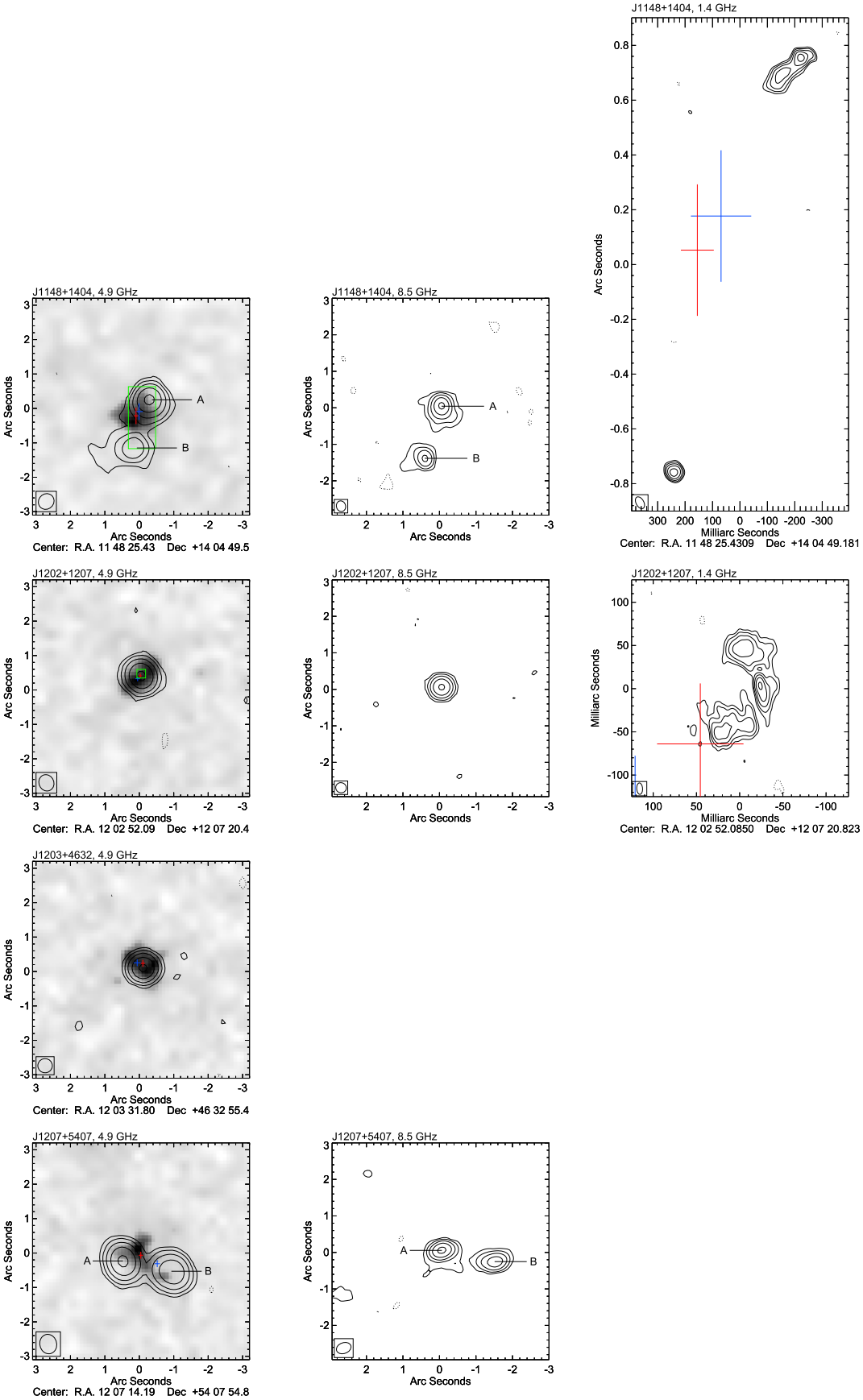

Figure 14. (Continued.)

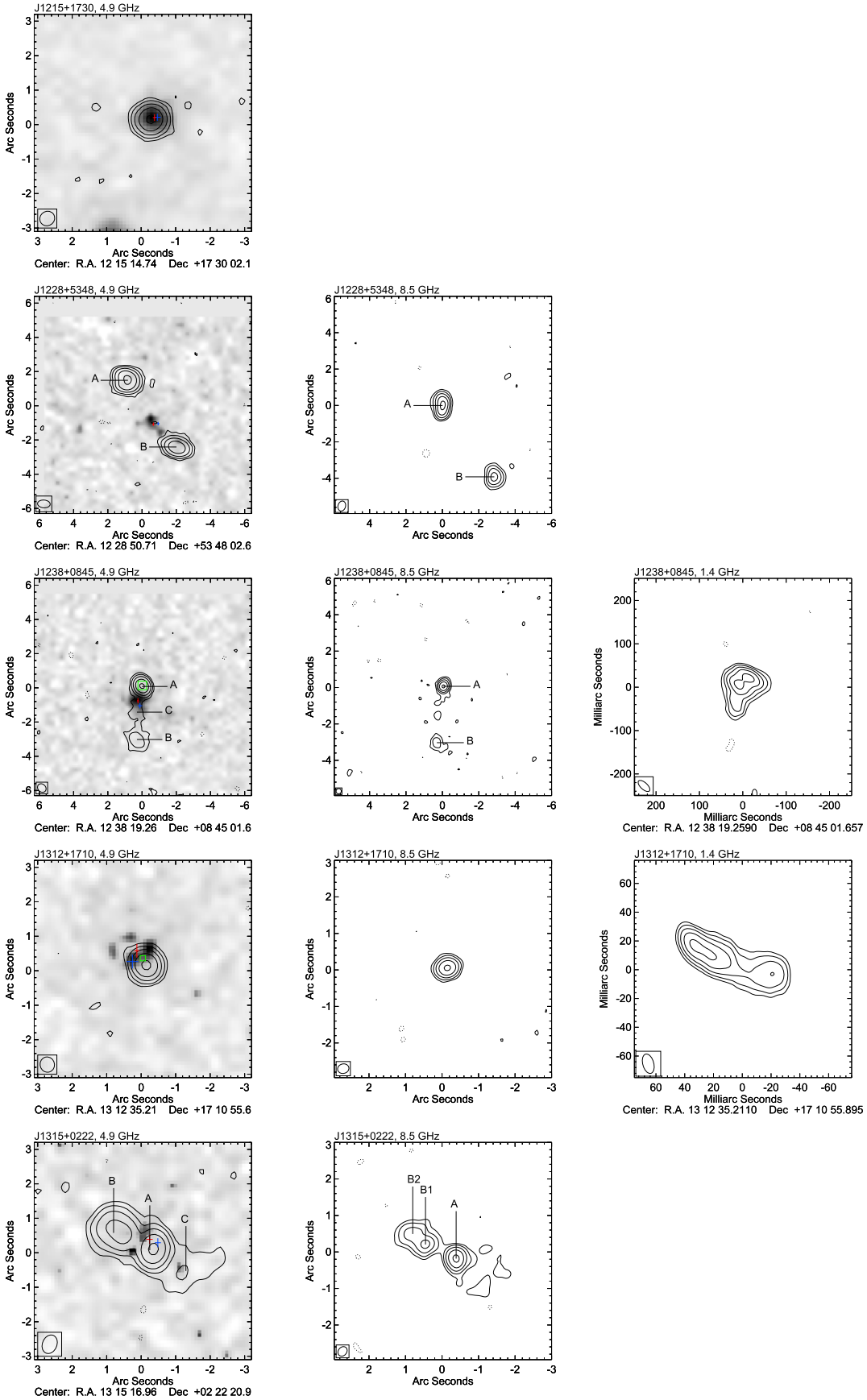

Figure 14. (Continued.)

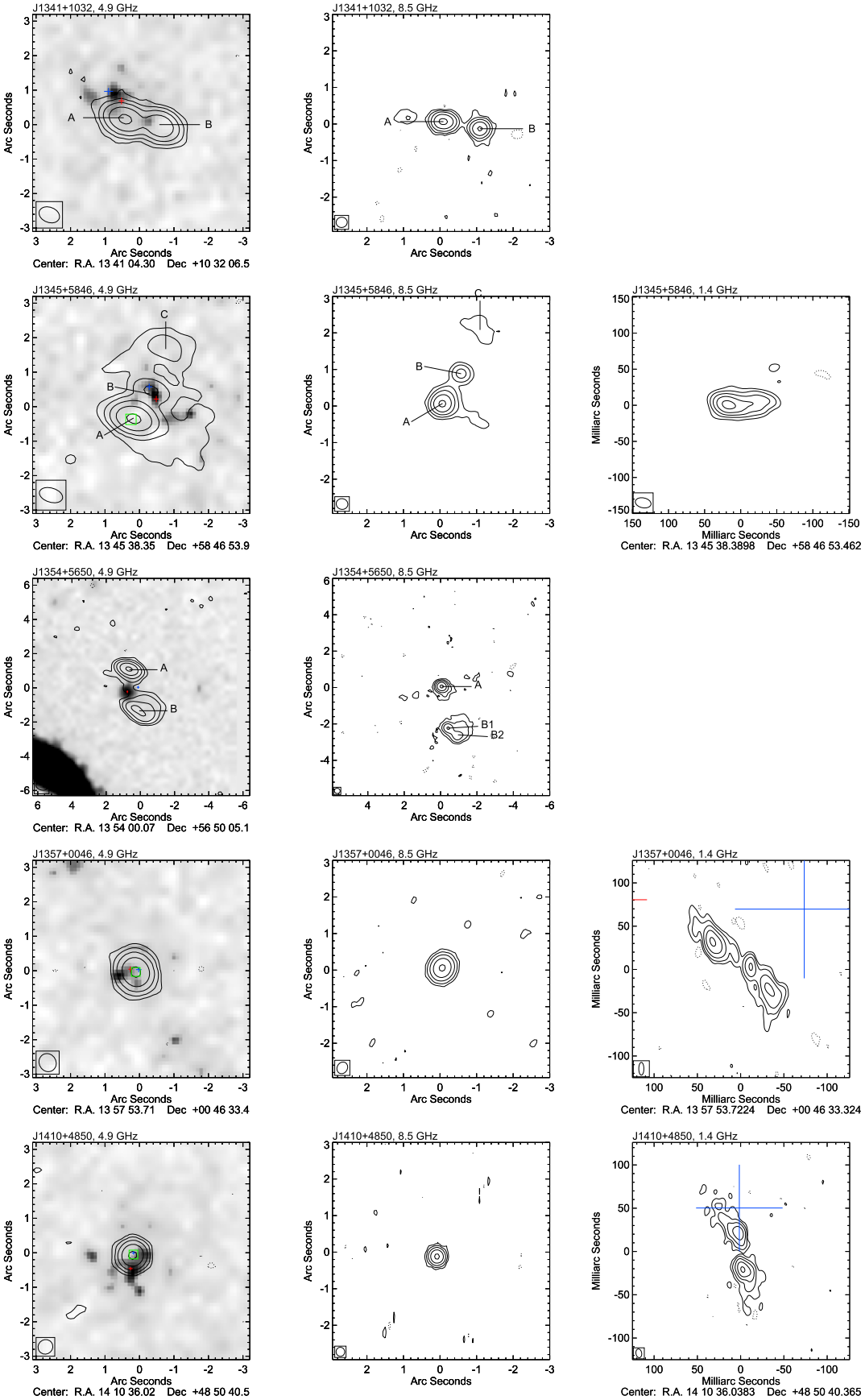

Figure 14. (Continued.)

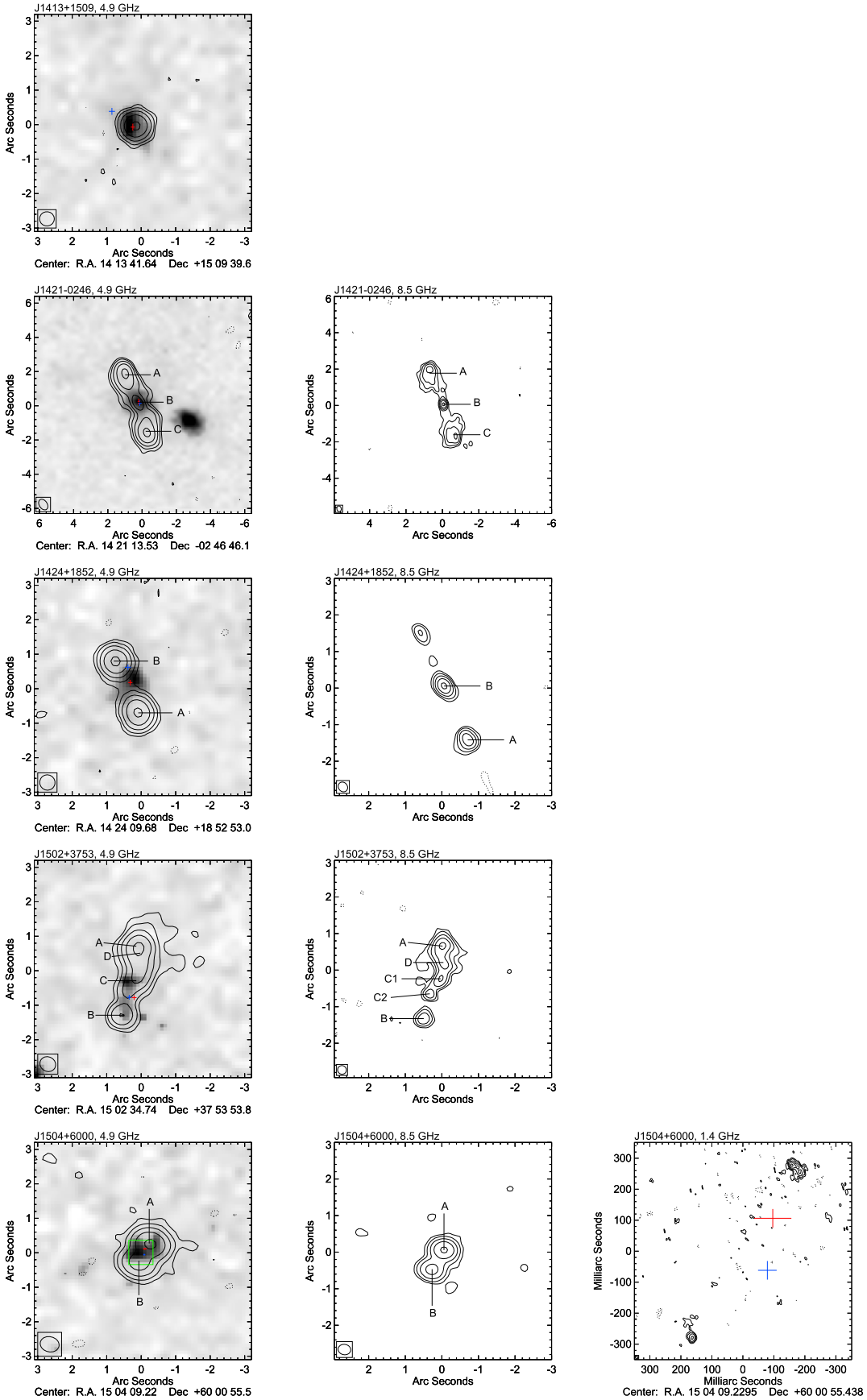

Figure 14. (Continued.)

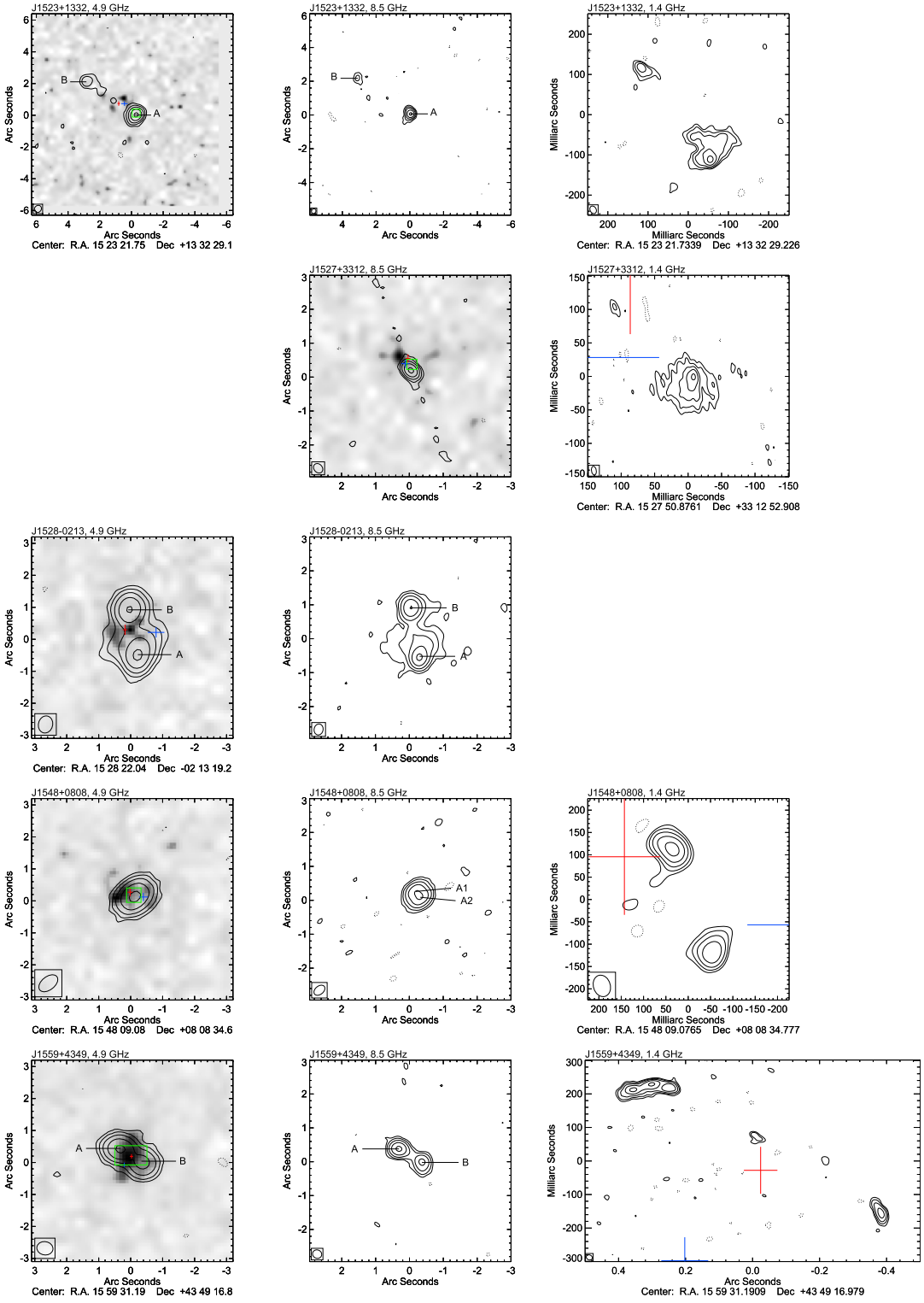

Figure 14. (Continued.)

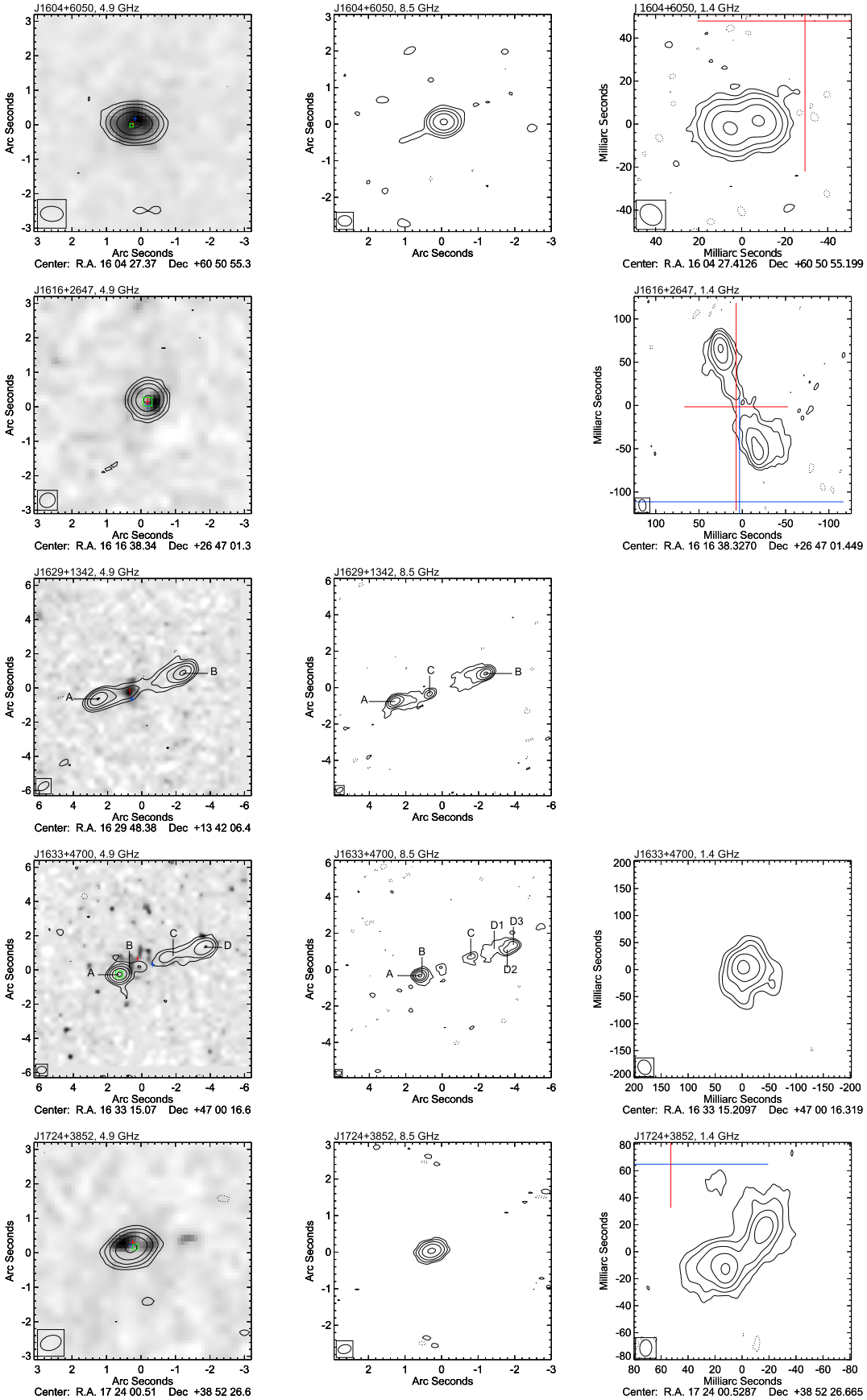

Figure 14. (Continued.)

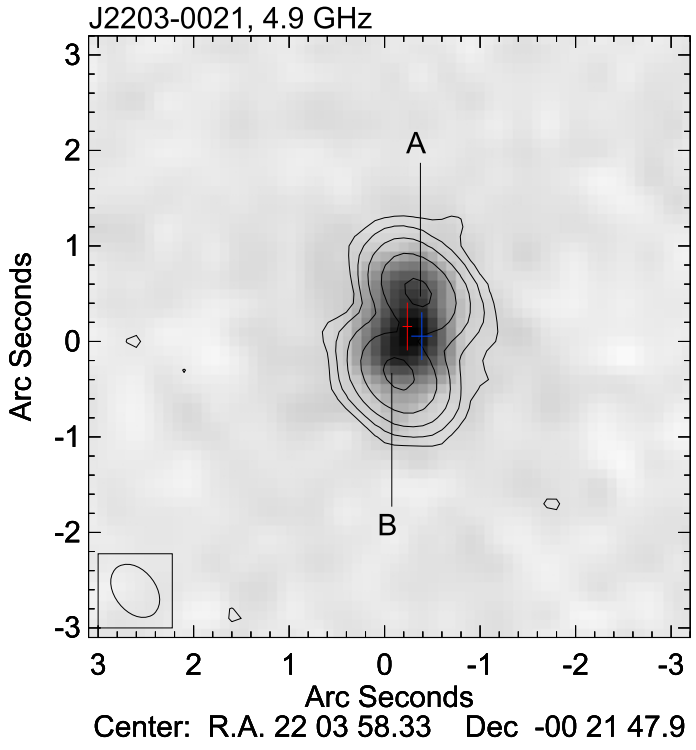

Figure 14. (Continued.)

densities are summed in calculating the spectral index. Note that because the beam sizes differ between 4.9 and 8.5 GHz in our observations, these spectral indices should be treated as estimates. The Gaussian profile may not be a good estimate for resolved components with complicated structures, but we make sure the total flux density is conserved during the fits.

REFERENCES

Adelman-McCarthy, J. K., Agueros, M. A., Allam, S. S., et al. 2007, ApJS, 172, 634
An, T., & Baan, W. A. 2012, ApJ, 760, 77
Barvainis, R., & Ivison, R. 2002, ApJ, 571, 712
Beasley, A. J., Gordon, D., Peck, A. B., et al. 2002, ApJS, 141, 13
Becker, R. H., White, R. L., & Helfand, D. J. 1995, ApJ, 450, 559
Begelman, M. C. 1996, in Cygnus A—Study of a Radio Galaxy, ed. C. L. Carilli, & D. E. Harris, 209
Best, P. N., Kauffmann, G., Heckman, T. M., et al. 2005, MNRAS, 362, 25
Cai, Z., Nan, R., Schilizzi, R. T., et al. 2002, A&A, 381, 401
Chambers, K. C., Miley, G. K., van Breugel, W. J. M., et al. 1996, ApJS, 106, 247
Chengalur, J. N., & Kanekar, N. 2003, PhRvL, 91, 241302
Condon, J. J., Cotton, W. D., Greisen, E. W., et al. 1998, AJ, 115, 1693
Curran, S. J., Allison, J. R., Glowacki, M., et al. 2013, MNRAS, 431, 3408
Curran, S. J., Murphy, M. T., Pihlström, Y. M., et al. 2004, MNRAS, 352, 563
Curran, S. J., & Whiting, M. T. 2010, ApJ, 712, 303
Curran, S. J., & Whiting, M. T. 2012, ApJ, 759, 117
Curran, S. J., Whiting, M. T., Combes, F., et al. 2011a, MNRAS, 416, 2143
Curran, S. J., Whiting, M. T., Murphy, M. T., et al. 2006, MNRAS, 371, 431
Curran, S. J., Whiting, M. T., Wiklind, T., et al. 2008, MNRAS, 391, 765
Dallacasa, D., Fanti, C., Giacintucci, S., et al. 2002a, A&A, 389, 126
Dallacasa, D., Tinti, S., Fanti, C., et al. 2002b, A&A, 389, 115
Darling, J. 2003, PhRvL, 91, 011301
Darling, J. 2004, ApJ, 612, 58
Douglas, J. N., Bash, F. N., Bozyan, F. A., Torrence, G. W., & Wolfe, C. 1996, AJ, 111, 1945
Drinkwater, M. J., Webster, R. L., Francis, P. J., et al. 1997, MNRAS, 284, 85
Eisenstein, D. J., Weinberg, D. H., Algol, E., et al. 2011, AJ, 142, 72
Fanaroff, B. L., & Riley, J. M. 1974, MNRAS, 167, 31P
Fanti, C., Fanti, R., Dallacasa, D., et al. 1995, A&A, 302, 317
Fanti, C., Pozzi, F., Dallacasa, D., et al. 2001, A&A, 369, 380
Fanti, R., Fanti, C., Schilizzi, R. T., et al. 1990, A&A, 231, 333
Grandi, S. A. 1977, ApJ, 215, 446
Gregory, P. C., & Condon, J. J. 1991, ApJS, 75, 1011
Griffith, M. R., Wright, A. E., Burke, B. F., & Ekers, R. D. 1994, ApJS, 90, 179
Griffith, M. R., Wright, A. E., Burke, B. F., & Ekers, R. D. 1995, ApJS, 97, 347
Gugliucci, N. E., Taylor, G. B., Peck, A. B., & Giroletti, M. 2005, ApJ, 622, 136
Gupta, N., Salter, C. J., Saikia, D. J., Ghosh, T., & Jeyakumar, S. 2006, MNRAS, 373, 972
Healey, S. E., Romani, R. W., Taylor, G. B., et al. 2007, ApJS, 171, 61
Helmboldt, J. F., Taylor, G. B., Tremblay, S., et al. 2007, ApJ, 658, 203
Inoue, M. Y., Kameno, S., Kawabe, R., et al. 1996, AJ, 111, 1852
Ishwara-Chandra, C. H., Dwarakanath, K. S., & Anantharamaiah, K. R. 2003, JApA, 24, 37
Kanekar, N., Carilli, C. L., Langston, G. I., et al. 2005, PhRvL, 95, 261301
Kanekar, N., Chengalur, J. N., & Lane, W. M. 2007, MNRAS, 375, 1352
Kanekar, N., Ellison, S. L., Momjian, E., York, B. A., & Pettini, M. 2013, MNRAS, 428, 532
Kanekar, N., Gupta, A., Carilli, C. L., Stocke, J. T., & Willett, K. W. 2014, ApJ, 782, 56
Kanekar, N., Langston, G. I., Stocke, J. T., Carilli, C. L., & Menten, K. M. 2012, ApJL, 746, L16
Keeney, B. A., Stocke, J. T., Danforth, C. W., & Carilli, C. L. 2011, AJ, 141, 66
Kewley, L. J., Groves, B., Kauffmann, G., & Heckman, T. 2006, MNRAS, 372, 961
Kunert-Bajraszewska, M., Janiuk, A., Gawroński, M. P., & Siemiginowska, A. 2010, ApJ, 718, 1345
Kunert-Bajraszewska, M., & Marecki, A. 2007, A&A, 469, 437
Lehar, J., Burke, B. F., Conner, S. R., et al. 1997, AJ, 114, 48
Lister, M. L., Kellermann, K. I., Vermeulen, R. C., et al. 2003, ApJ, 584, 135
Liu, X., Cui, L., Luo, W.-F., Shi, W.-Z., & Song, H.-G. 2007, A&A, 470, 97
Mannucci, F., Basile, F., Poggianti, B. M., et al. 2001, MNRAS, 326, 745
Miley, G., & De Breuck, C. 2008, A&AR, 15, 67
Mirabel, I. F. 1989, ApJL, 340, L13
Mirabel, I. F. 1990, ApJL, 352, L37

Morganti, R., Oosterloo, T. A., Tadhunter, C. N., et al. 2004, A&A, 424, 119
Murphy, M. T., Curran, S. J., & Webb, J. K. 2003, MNRAS, 342, 830
Murphy, M. T., Webb, J. K., Flambaum, V. V., et al. 2001, MNRAS, 327, 1244
Murphy, M. T., Webb, J. K., & Flambaum, V. V. 2003, MNRAS, 345, 609
Murphy, M. T., Webb, J. K., & Flambaum, V. V. 2008, MNRAS, 384, 1053
Myers, S. T., Jackson, N. J., Browne, I. W. A., et al. 2003, MNRAS, 341, 1
O'Dea, C. P. 1998, PASP, 110, 493
O'Dea, C. P., & Baum, S. A. 1997, AJ, 113, 148
Owsianik, I., & Conway, J. E. 1998, A&A, 337, 69
Patnaik, A. R., Browne, I. W. A., Wilkinson, P. N., & Wrobel, J. M. 1992, MNRAS, 254, 655
Peck, A. B., & Taylor, G. B. 2000, ApJ, 534, 90
Perlman, E. S., Carilli, C. L., Stocke, J. T., & Conway, J. 1996, AJ, 111, 1839
Perlman, E. S., Stocke, J. T., Carilli, C. L., et al. 2002, AJ, 124, 2401
Perlman, E. S., Stocke, J. T., Conway, J., & Reynolds, C. 2001, AJ, 122, 536
Pihlström, Y. M., Conway, J. E., & Vermeulen, R. C. 2003, A&A, 404, 871
Polatidis, A., Wilkinson, P. N., Xu, W., et al. 1999, NewAR, 43, 657
Readhead, A. C. S., Taylor, G. B., Xu, W., et al. 1996, ApJ, 460, 612
Roettgering, H. J. A., Lacy, M., Miley, G. K., Chambers, K. C., & Saunders, R. 1994, A&AS, 108, 79
Sarazin, C. L., Burns, J. O., Roettiger, K., & McNamara, B. R. 1995, ApJ, 447, 559
Stanghellini, C., Dallacasa, D., O'Dea, C. P., et al. 2001, A&A, 377, 377
Stanghellini, C., O'Dea, C. P., Baum, S. A., et al. 1997, A&A, 325, 943
Stocke, J. T., Wurtz, R., Wang, Q., Elston, R., & Jannuzi, B. T. 1992, ApJL, 400, L17
Strateva, I., Ivezić, Ž, Knapp, G. R., et al. 2001, AJ, 122, 1861
Tremblay, S. E. 2011, PhD thesis, The Univ. New Mexico
Urry, C. M., & Padovani, P. 1995, PASP, 107, 803
Vermeulen, R. C., Pihlström, Y. M., Tschager, W., et al. 2003, A&A, 404, 861
Webb, J. K., Flambaum, V. V., Churchill, C. W., Drinkwater, M. J., & Barrow, J. D. 1999, PhRvL, 82, 884
Webb, J. K., King, J. A., Murphy, M. T., et al. 2011, PhRvL, 107, 191101
Wiklind, T., & Combes, F. 1994, A&A, 286, L9
Wiklind, T., & Combes, F. 1995, A&A, 299, 382
Wiklind, T., & Combes, F. 1996a, A&A, 315, 86
Wiklind, T., & Combes, F. 1996b, Natur, 379, 139
Willott, C. J., Rawlings, S., Jarvis, M. J., & Blundell, K. M. 2003, MNRAS, 339, 173
Wright, A., & Otrupcek, R. 1990, Parkes (PKS) Catalog
Xiang, L., Stanghellini, C., Dallacasa, D., & Haiyan, Z. 2002, A&A, 385, 768
Yan, T. 2013, PhD dissertation, Univ. Colorado
Yan, T., Stocke, J. T., Darling, J., & Hearty, F. 2012, AJ, 144, 124 (Paper I)
York, B. L., Kanekar, N., Ellison, S. A., & Pettini, M. 2007, MNRAS, 328, L53